Polariton Condensates in a Semiconductor Microcavity Influenced by All-Optical Methods

Dissertation

presented to the Faculty of Physics of the
TU Dortmund University, Germany,
in partial fulfillment of the requirements
for the degree of

Doktor rer. nat.

by
Franziska Wishahi geb. Veit

technische universität
dortmund

Dortmund, July 2013

Accepted by the Faculty of Physics of the TU Dortmund University, Germany.

Day of the oral examination: 30th August 2013

Examination board:
Prof. Dr. Manfred Bayer
Prof. Dr. Thomas Weis
Prof. Dr. Bernhard Spaan
Dr. Alex Greilich

Contents

Chapter 1

Motivation

Seamless, instant communication with people all around the world has become an integral part of everyday life. It is hard to picture today's society without fast data exchange, in private and business matters. This revolution in telecommunication is to a large extent related to the massive utilization of optical fibers as a tool for conveying information over large distances. The first publications on optical fibers in 1954 [1, 2] and the development for telecommunication by Kao et al. in 1961 [3] were the starting point of a fast progressing domain. The interface between optical data transmission and electronic circuits are the so-called optoelectronic devices. Optical transmitters consist typically of light-emitting diodes (LEDs) [4] or semiconductor lasers [5]. Up to now, it was possible to demonstrate a data-sending rate of 101.7 Tbit/s (370x273 Gbit/s) through 165 km of fiber [6]. Besides further research in the field of optical fibers, such as photonic-band-gap fibers [7], it could also be desirable to switch from electronic to optical data processing by creating photonic circuits. Even though this way of processing will most probably also involve some electronics, it could help to reduce the heat load and to increase the net speed in computing systems [8]. The first step towards optical processing is the realization of an optical transistor as a fundamental component of each processing system. With an optical transistor, the creation of optical logic gates would be possible. Several approaches are subject of the current scientific research on optical transistors such as quantum dots in nanocavities [9], semiconductor nanocrystals [10] and ring resonators [11]. To realize optical logic for mainstream applications several criteria such as logic-level restoration, cascadability, fan-out or input/output isolation [12] have to be fulfilled. Therefore, all-optical computers remain a future major challenge.

Since computing is a nonlinear process, where multiple signals have to interact, electronic as well as optical processing depends on the Coulomb interaction of electrons. For light this can be implemented by using materials with a nonlinear refractive index. Given that the nonlinear coefficients of these materials are generally small, optical gates require high power to function. This is contrary to the goal of reducing the heat load with optical processing. Realizing polaritonic instead of photonic circuits, this high power requirement could be loosened.

Exciton-polaritons are the result of strong-coupling between excitons and photons in semiconductor microcavities [13, 14]. The photonic nature of the polariton provides a high speed of exchanging information and the excitonic character opens the field to nonlinear switching processes due to Coulomb interactions. As a results of their bosonic nature in the low density limit, polaritons obey Bose statistics and are able to undergo Bose-Einstein condensation (BEC). With this phase transition at a critical temperature or density, a collective and coherent state of matter is created where individual entities cannot be distinguished anymore. First experimental evidence of atomic BEC at a few nanokelvin was presented in 1995 by the group of Cornell and Wieman [15] and Ketterle [16]. Though, the required low critical temperature that is related to the high atomic masses makes atomic BEC impractical for large scale applications. In contrast, polaritons, due to their photonic nature, have a comparably small effective mass. In 2006 Kasprzak et al. experimentally demonstrated Bose-Einstein condensation of exciton polaritons in a semiconductor microcavity at 19 K [17]. A few years later, the first polariton laser in a GaN-based microcavity at room-temperature was presented [18, 19]. The condensate properties and the nature of polaritons make polariton condensates perfect candidates for logic circuits. Several experimental demonstrations of controlling and manipulating polaritonic systems all optically [20], with further cavity confinement [21, 22] or by adding metallic layers on top of the cavity [23], took place in the last years. Recently, first proposals for a polariton spin switch [24], polariton transistor [25, 26] and polariton resonant tunneling diodes [27] were presented.

The main topic of this thesis is the optical control and manipulation of a polariton condensate in a planar GaAs-based microcavity. Optical methods have the advantage of introducing a fast change of experimental conditions without the necessity to reprocess the sample. The strong repulsive interactions of polaritons under nonresonant excitation lead to a blueshift of the condensate. It is proportional to the excitation density at a given spatial position. Hence, the spatial shape of the excitation spot defines the polariton potential under nonresonant excitation. In the first part of this thesis the excitation spot is differently shaped using a spatial light modulator. By imprinting a wire-shaped spot on the sample, the polariton condensate is spatially trapped to this shape and the dynamics of a 2D confined polariton condensate can be studied. Furthermore, it is possible to create also nontrivial potential landscapes such as a staircase, which allows a direct tailoring of the externally accessible momentum-space properties. Results of far-field spectroscopy visualize this control of the polariton flow via change of the excitation density. Additionally, the spatial dynamics under this pumping conditions and for several excitation densities are demonstrated and analyzed. Second, a steady-state polariton condensate, created with a resonant continuous-wave laser, is perturbed by a nonresonant short laser pulse. The influence of the external disturbance on the polariton flow is examined with results of time-resolved momentum-space measurements. Both approaches to manipulate and control polariton condensates all-optically, demonstrated in this thesis, could represent a further step towards

the realization of polariton logic circuits.

The thesis is structured as follows. Chapter 2 provides a theoretical background for the thesis: it starts with a description of exciton polaritons and microcavities and ends with a report on Bose-Einstein condensation especially in 2D polariton systems. Chapter 3 contains an introduction to the investigated sample, the method of momentum- and real-space imaging and the experimental setup. In Chap. 4 the results of wire-shaped, nonresonant excitation are analyzed followed by Chap. 5 with a demonstration of the optical control of the polariton flow on a polariton staircase. Chapter 6 includes an analysis of the temporal and spatial behavior of a polariton condensate under a perturbation with short, nonresonant laser pulses. Finally, a summary of the main results and an outlook conclude the thesis in Chap. 7 .

Chapter 2

Theoretical Background

This thesis thematically embraces the formation of a polariton condensate in a planar semiconductor microcavity system and optical methods which are appropriate to influence such a condensate. For a detailed analysis of the corresponding experimental results, theoretical background information is provided within this chapter, which is organized in two main parts. In the first part, the theory of microcavity polaritons is presented. Firstly the exciton in a direct band-gap semiconductor is described. It is followed by the theory of photons confined in a semiconductor microcavity leading to the discussion of cavity polaritons and their properties. The second part of this chapter covers the theory of Bose-Einstein condensation: starting with an ideal Bose gas and ending with a presentation of polariton Bose-Einstein condensates under nonresonant excitation.

2.1 Microcavity Polaritons

Under optical excitation the fundamental electronic excitations above the ground state of a semiconductor with a direct band-gap are excitons. With regard to momentum conservation it is possible that the created exciton couples strongly to a photon mode and a new quasiparticle is formed, called exciton-polariton. Due to momentum conservation in the light-matter-coupling two normal-modes with an energy splitting are formed, the upper and lower polariton, first described by Agranovich (1957)[28] and Hopfield (1958)[29]. With the possibility of creating semiconductor nanostructures, the dimensionality of the exciton does no longer match that of the photon (3D). Instead of normal-mode splitting an irreversible radiative decay was found as a consequence of the coupling between an exciton mode and a continuum of photon modes [30]. With the development of semiconductor microcavities it was possible to confine simultaneously the photon as well as the exciton. In 1992, Weisbuch presented for the first time strong coupling in a 2D system [13].

The present section gives an overview on the concepts of microcavity polaritons.

If not indicated otherwise, the discussion below follows the work of Klingshirn [31], Kavokin [32], Savona [14] and Deng [33].

2.1.1 Excitons

A semiconductor is characterized by a completely occupied valance band and an empty conduction band. The extreme values of the valance- and conduction band of an idealized direct band-gap semiconductor are at the center of the Brillouin zone. To create free carriers this band-gap has to be transcended energetically. This is possible through absorption of a photon with an energy equal or greater than the gap. The electron excited into the conduction band leaves a positively charged hole in the valance band. Because of attractive Coulomb interaction between the electron and hole a quasiparticle is formed - the exciton. If the radius of this bound complex is larger than several unit cells it is called Mott-Wannier exciton. With a radius in the order of the lattice constant it is called Frenkel exciton. Frenkel excitons are common in molecular- or insulator crystals. For an inorganic semiconductor the description of the Mott-Wannier excitons is more relevant [31].

The stability of an exciton is mostly determined by collisions with phonons. The phonon energy at temperature T is defined by $k_\mathrm{B}T$, where k_B is the Boltzmann constant. Since Frenkel excitons have a small radius their binding energy is of the order of 100 meV to 1 eV. So the exciton stability is given at room temperature. Since the binding energy of Mott-Wannier excitons is relatively low due to their large radius (in the order of about 1 meV) and $k_\mathrm{B}T$ is about 25 meV at room temperature, it is clear why in bulk semiconductors they are only observed at cryogenic temperatures [34]. In the following only Mott-Wannier excitons will be considered since they are the relevant excitons in semiconductors investigated within this thesis.

Within the effective mass approximation, the electron and hole energies read

$$E_\mathrm{e} = E_\mathrm{g} + \frac{\hbar^2 \boldsymbol{k}^2}{2m_\mathrm{e}^*} \qquad \text{and} \qquad E_\mathrm{h} = \frac{\hbar^2 \boldsymbol{k}^2}{2m_\mathrm{h}^*}, \tag{2.1}$$

where m_e^* and m_h^* are the effective electron and hole masses and E_g is the band-gap energy. In consideration of the attractive Coulomb interaction, the Hamiltonian of the exciton is given by

$$H = E_\mathrm{g} + \frac{\hbar^2 \nabla_\mathrm{e}^2}{2m_\mathrm{e}^*} + \frac{\hbar^2 \nabla_\mathrm{h}^2}{2m_\mathrm{h}^*} - \frac{e^2}{\epsilon_r \epsilon_0 |\boldsymbol{r}_\mathrm{e} - \boldsymbol{r}_\mathrm{h}|}. \tag{2.2}$$

ϵ_r and ϵ_0 are the relative permittivity of the material and the vacuum permittivity, respectively and e is the elementary electric charge. With a separation ansatz into center of mass ($\boldsymbol{R}$) and relative ($\boldsymbol{r}$) coordinates, the exciton problem can be treated in analogy to the hydrogen-atom problem. By use of $\boldsymbol{R} = (m_\mathrm{e}^* \boldsymbol{r}_\mathrm{e} - m_\mathrm{h}^* \boldsymbol{r}_\mathrm{h})/(m_\mathrm{e}^* + m_\mathrm{h}^*)$

and $\boldsymbol{r} = \boldsymbol{r}_\mathrm{e} + \boldsymbol{r}_\mathrm{h}$ the Schrödinger equation in relative coordinates is decoupled from the equation based on center of mass coordinates:

$$\left(\frac{\hbar^2 \nabla_R^2}{2M}\right) \Psi(\boldsymbol{R}) = E_R \Psi(\boldsymbol{R}), \tag{2.3}$$

$$\left(\frac{\hbar^2 \nabla_r^2}{2\mu} - \frac{e^2}{4\pi\epsilon_r\epsilon_0|\boldsymbol{r}|}\right) \Phi(\boldsymbol{r}) = E_r \Phi(\boldsymbol{r}), \tag{2.4}$$

with the reduced $\mu = (m_\mathrm{e}^* + m_\mathrm{h}^*)/(m_\mathrm{e}^* m_\mathrm{h}^*)$ and total mass $M = m_\mathrm{e}^* + m_\mathrm{h}^*$. Solving the differential equation for the energy spectrum of a free exciton, the exciton dispersion is written as:

$$E_\mathrm{X}(\boldsymbol{K}) = E_\mathrm{g} - \frac{E_\mathrm{b}}{n^2} + \frac{\hbar^2 \boldsymbol{K}^2}{2M} \tag{2.5}$$

$E_\mathrm{b} = e^2/(2\epsilon_0 a_0)$ is the binding energy, $a_0 = \hbar^2\epsilon_0/(e^2\mu)$ the Bohr radius and n the quantum number of the free exciton. In contrast to the hydrogen-atom, excitons have a considerably shorter lifetime. In direct band-gap semiconductors the lifetime is of the order of nanoseconds, while in indirect band-gap materials the exciton decays after a few microseconds until some milliseconds. A deeper discussion of excitons, for example their interaction behavior or the possibility of exciton condensation, can be found e.g. in the work of Hanamura et al. [35].

Excitons in Low-Dimensional Semiconductors

By reducing the spatial extent of the semiconductor material to the order of the thermal de Broglie wavelength

$$\lambda_\mathrm{dB}^\mathrm{e,h} = \frac{2\pi\hbar}{\sqrt{3 m_\mathrm{e,h}^* k_\mathrm{B} T}}, \tag{2.6}$$

properties of the electron in the conduction band (CB) and hole in the valance band (VB) become influenced. Particularly, the density of states and energies of the carriers become quantized. In the following, the density of states for the electron in the CB shall be focused on. The density of states $D(E)$ represents the number of available eigenstates for the electrons at a certain energy E within an infinitesimal interval dE. In Tab. 2-1 the density of states is presented for systems with different dimensionality – from a 3D to a 0D system. With decreasing dimensionality a further quantization of the energy levels occurs, as schematically visualized in Fig. 2-1.

Dimension	Density of states
3D	$D(E) = \frac{1}{2\pi^2}\left(\frac{2m_e^*}{\hbar^2}\right)^{3/2}\sqrt{E - E_{CB}}$
2D	$D(E) = \frac{m_e^*}{\pi\hbar^2}\sum_i \Theta(E - E_{CB} - \Delta E_i)$
1D	$D(E) = \frac{\sqrt{2m_e^*}}{\pi\hbar}\sum_i \frac{n_i\Theta(E-E_{CB}-\Delta E_i)}{\sqrt{E-E_{CB}-\Delta E_i}}$
0D	$D(E) = 2\sum_i \delta(E - E_{CB} - \Delta E_i)$

Table 2-1: Electron density of states for semiconductors of different dimensionality. $\Theta(E)$ is the Heaviside unit step-function and ΔE_i is the difference between the minimum and the i-th energy level of the CB. n_i denotes the degeneracy of the respective energy level. With decreasing dimensionality a further quantization of the energy levels occurs, as schematically visualized in Fig. 2-1.

When the motional degree of freedom is reduced in a three dimensional bulk semiconductor along one direction, one obtains a thin film semiconductor. It is also known as quantum well (QW). A quantum wire (QWR) is an example for an one-dimensional semiconductor. In a quantum dot (QD) the carrier mobility is confined in all directions. Since 2D-semiconductors are used as active medium in the microcavities studied in this work, the focus is placed on the effects on excitons in QWs.

The electronic confinement in one dimension leads to a splitting into light- and heavy-hole excitons; within a QW the potential symmetry is reduced, hence, the valance-band states are split. This is one of the most striking changes resulting from the reduction of dimensionality. Another effect is that the increase in the overlap of the wave functions of electron and hole and the growing Coulomb attraction between these two carriers lead to a larger exciton oscillator strength. This corresponds to a decrease in the exciton Bohr radius and larger binding energy of the exciton in the QW compared to the exciton in a bulk semiconductor. The change in the binding energy strongly depends on the width l_z of the QW along the growth axis z and on the semiconductor material. In the case of the ground-state $1S$ exciton and infinitely high barriers, where $l_z = 0$, the binding energies in terms of the bulk values E_b^{3D} are given by [36]:

$$E_b^{2D}(1S) = \frac{E_b^{3D}}{(n - \frac{1}{2})^2}. \tag{2.7}$$

For realistic QWs with a finite barrier height there is a local maximum of the binding energy depending on the material and the QW width [37]. In the case of a $1S$ exciton E_b is still two to three times higher than in bulk materials.

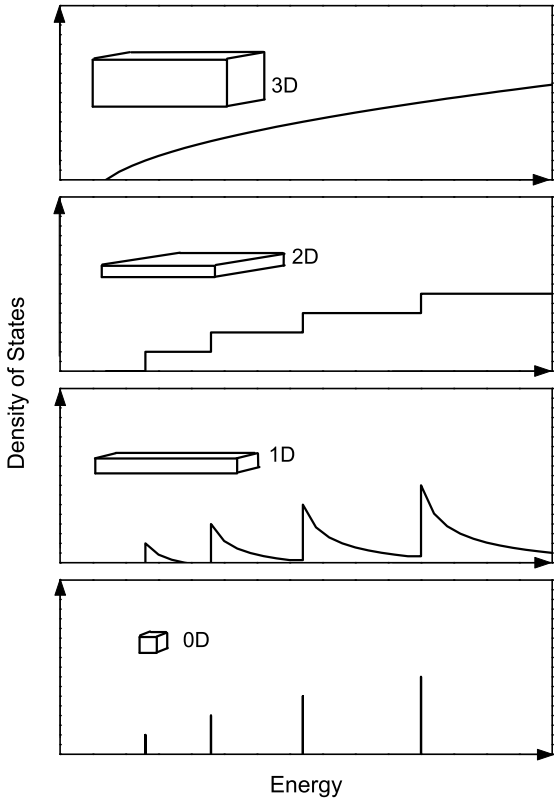

Figure 2-1: Schematic diagram of the electronic density of states for different spatial dimensionalities. With decreasing dimensionality of the material there is a discretization of the energy levels.

2.1.2 Photons in a Planar Microcavity

To influence the density of states of the light field an optical resonator can be used. Two planar mirrors in a distance L_{Cav} can build a resonator to confine the light. Due to multiple reflection and interference there is a build-up of standing waves for certain resonance frequencies. Hence, in contrast to the linear dispersion relation of a free photon, the resonator mirrors lead to a discretization of the wave vector:

$$k_z = \frac{N\pi}{L_{\mathrm{Cav}}} \tag{2.8}$$

with the number $N \in \mathbb{N}$ of the particular resonant Fabry-Perot mode and the cavity length L_{Cav}. The in-plane wave vector $k_{||} = \sqrt{k_x^2 + k_y^2}$ stays unaffected. Hence, the dispersion relation for photons in a planar resonator is

$$E_{\mathrm{Cav}}(k_{||}) = \frac{\hbar c}{n_{\mathrm{Cav}}} \sqrt{\left(\frac{\pi^2 N^2}{L_{\mathrm{Cav}}^2} + k_{||}^2\right)} \tag{2.9}$$

with n_{Cav} as the refraction index inside the cavity. For small momentum, the dispersion has a parabolic shape and can be described by an effective photon mass $m^*_{\mathrm{Cav}} = hn_{\mathrm{Cav}}/(cL_{\mathrm{Cav}})$ [38]. With increasing momentum the dispersion curve joins the linear relation $E(k_{||}) = \hbar c k_{||}/n_{\mathrm{Cav}}$. The relation between the emission angle Θ from the cavity and the photon in-plane wave vector $k_{||}$ is given by $k_{||} = k \sin\Theta$ and offers the possibility of experimentally investigating the energy dispersion relation by performing angle resolved spectroscopy.

The longitudinal mode separation $\delta\lambda$, which is the spectral distance of two resonant frequencies in a resonator, is given by [39]

$$\delta\lambda = \frac{\lambda^2}{2n_{\mathrm{Cav}}L_{\mathrm{Cav}}}. \tag{2.10}$$

Thus, macroscopic Fabry-Perot resonators ($L_{\mathrm{Cav}} \gg \lambda$) have a large number of modes next to each other, while for microcavities ($L_{\mathrm{Cav}} \approx \lambda$) the mode separation is large enough to allow single-mode emission.

An ideal cavity possesses precise values for the confined resonant modes and has no losses. To describe the discrepancy between the ideal and real case a quality factor Q is used. The quality factor is given by the ratio of the resonance wavelength λ_{Cav} and its linewidth $\Delta\lambda_{\mathrm{Cav}}$ and is proportional to the cavity lifetime τ_{Cav}:

$$Q = \frac{\lambda_{\mathrm{Cav}}}{\Delta\lambda_{\mathrm{Cav}}} = 2\pi\frac{c\,\tau_{\mathrm{Cav}}}{\lambda_{\mathrm{Cav}}}. \tag{2.11}$$

Typical Q-factor values for different kinds of microcavities can be found in the publication of Vahala et al. [40].

If the linewidth is small the lifetime of the photon inside the cavity increases. For high Q-factors the number of round trips of the wave in the resonator and, therefore, the photonic confinement increase. In order to realize microcavities with a high Q-factor, distributed Bragg reflectors (DBR) are used as mirrors, see details in chapter 3.1. DBRs consist of many layers of alternating films with low (L) and high (H) refractive indices. The optical path $d(\lambda)$ in each film is determined by the quarter of the cavity center wavelength $d(\lambda) = \lambda_{\mathrm{Cav}}/(4n_{\mathrm{L/H}})$. This ensures the build-up of a broad-band high reflectivity region - it is called stop band. In this region the reflectivity is given by [41]

$$R = \frac{1 - \frac{n_{\mathrm{sub}}}{n_0}\left(\frac{n_{\mathrm{L}}}{n_{\mathrm{H}}}\right)^{2m_{\mathrm{DBR}}}}{1 + \frac{n_{\mathrm{sub}}}{n_0}\left(\frac{n_{\mathrm{L}}}{n_{\mathrm{H}}}\right)^{2m_{\mathrm{DBR}}}} \tag{2.12}$$

where n_{sub} and n_0 are the refractive indices of the substrate beyond the DBRs and of the closing layer on top of the microcavity, respectively. m_{DBR} is the number of pairs of mirror layers. To have the electric field antinode of the standing wave at the center of the cavity, the size of the cavity is commonly chosen as a multiple of

$\lambda_{\mathrm{Cav}}/2$.

Since the photon field penetrates into the DBR structure, the cavity length L_{Cav} from a standard Fabry-Perot cavity has to be replaced by an effective cavity length L_{eff} [14]:

$$L_{\mathrm{eff}} = L_{\mathrm{Cav}} + L_{\mathrm{DBR}} \tag{2.13}$$

with

$$L_{\mathrm{DBR}} = \frac{\lambda_{\mathrm{Cav}}}{2\, n_{\mathrm{Cav}}} \frac{n_{\mathrm{L}}\, n_{\mathrm{H}}}{n_{\mathrm{H}} - n_{\mathrm{L}}}. \tag{2.14}$$

Moreover, if there is an imperfection during the growth of the DBR structure, differences in the cavity resonance frequency ω_{Cav} and center frequency ω_{DBR} of the stop-band appear. Thus, the real microcavity resonance frequency is

$$\omega_{\mathrm{MC}} = \frac{L_{\mathrm{Cav}}\, \omega_{\mathrm{Cav}} + L_{\mathrm{DBR}}\, \omega_{\mathrm{DBR}}}{L_{\mathrm{eff}}}. \tag{2.15}$$

2.1.3 Polaritons - Strong Coupling in Microcavities

How can one achieve that an exciton and a photon mutually interact to form a polariton? By placing a QW into a microcavity system the excitons of the QW and the photon of the cavity can interact. In order to increase the oscillator strength of the exciton and, therefore, also its coupling to the light field, the QWs are placed at the antinodes of the microcavity. The interaction can be described in a simplified model as an ensemble of coupled harmonic oscillators.

The Hamiltonian of the system near resonance ($E_{\mathrm{Cav}} \approx E_{\mathrm{X}}$) takes the following form in the rotating wave approximation :

$$\hat{H}_{\mathrm{Pol}} = \hat{H}_{\mathrm{Cav}} + \hat{H}_{\mathrm{X}} + \hat{H}_{\mathrm{int}} \tag{2.16}$$

$$= \sum_{\boldsymbol{k}} E_{\mathrm{Cav}}(\boldsymbol{k})\, \hat{a}^{\dagger}_{\boldsymbol{k}}\, \hat{a}_{\boldsymbol{k}} + \sum_{\boldsymbol{k}} E_{\mathrm{X}}(\boldsymbol{k})\, \hat{b}^{\dagger}_{\boldsymbol{k}}\, \hat{b}_{\boldsymbol{k}} + \sum_{\boldsymbol{k}} \hbar g(\boldsymbol{k})(\hat{a}^{\dagger}_{\boldsymbol{k}}\, \hat{b}_{\boldsymbol{k}} + \hat{b}_{\boldsymbol{k}}\, \hat{a}^{\dagger}_{\boldsymbol{k}}). \tag{2.17}$$

Here $\hat{a}^{\dagger}$ and $\hat{a}$ correspond to the photon creation and annihilation operators and $\hat{b}^{\dagger}$ and $\hat{b}$ to those of the exciton, respectively. To simplify the notation $\boldsymbol{k}$ stands in this section for $\boldsymbol{k}_{||}$. $\hbar g(k)$ accounts for the exciton-photon dipole interaction given through the exciton optical transition-matrix element M. Here, it is assumed that M is nonzero only for modes with the same in-plane wave vector.

By the following transformation

$$\hat{p}_{\boldsymbol{k}} = \mathcal{X}_{\boldsymbol{k}}\, \hat{b}_{\boldsymbol{k}} + \mathcal{C}_{\boldsymbol{k}}\, \hat{a}_{\boldsymbol{k}}, \tag{2.18}$$

$$\hat{q}_{\boldsymbol{k}} = \mathcal{X}_{\boldsymbol{k}}\, \hat{a}_{\boldsymbol{k}} - \mathcal{C}_{\boldsymbol{k}}\, \hat{b}_{\boldsymbol{k}}, \tag{2.19}$$

the Hamiltonian (2.17) can be diagonalized to

$$\hat{H}_{\mathrm{Pol}} = \sum_{\boldsymbol{k}} E_{\mathrm{LP}}(\boldsymbol{k}) \hat{p}^{\dagger}_{\boldsymbol{k}} \hat{p}_{\boldsymbol{k}} + \sum_{\boldsymbol{k}} E_{\mathrm{UP}}(\boldsymbol{k}) \hat{q}^{\dagger}_{\boldsymbol{k}} \hat{q}_{\boldsymbol{k}}. \tag{2.20}$$

These two new eigenmodes of the system are called exciton-polaritons. $\hat{p}^{(\dagger)}_{\boldsymbol{k}}$ is the (creation) annihilation operator of the lower polariton (LP) and $\hat{q}^{(\dagger)}_{\boldsymbol{k}}$ the one of the upper polariton (UP). The operators fulfill the commutation relation $[\hat{p}_{\boldsymbol{k}}, \hat{p}^{\dagger}_{\boldsymbol{k}}] = 1$ and $[\hat{q}_{\boldsymbol{k}}, \hat{q}^{\dagger}_{\boldsymbol{k}}] = 1$ and, therefore, they have bosonic character. In that context, an important parameter, the detuning $\Delta_{\boldsymbol{k}}$, has to be defined. It is the energy difference between the dispersion relation of the photon $E_{\mathrm{Cav}}(\boldsymbol{k})$ and the exciton $E_{\mathrm{X}}(\boldsymbol{k})$:

$$\Delta_{\boldsymbol{k}} = E_{\mathrm{Cav}}(\boldsymbol{k}) - E_{\mathrm{X}}(\boldsymbol{k}). \tag{2.21}$$

The dispersion relation for the new quasi-particles depends on the detuning and on the coupling strength $\hbar g(\boldsymbol{k})$:

$$E_{\mathrm{LP/UP}}(\boldsymbol{k}) = \frac{1}{2} \left\{ E_{\mathrm{X}}(\boldsymbol{k}) + E_{\mathrm{Cav}}(\boldsymbol{k}) \pm \sqrt{4\hbar^2 g(\boldsymbol{k})^2 + \Delta^2_{\boldsymbol{k}}} \right\}. \tag{2.22}$$

In Fig. 2-2 (a)-(c) the polariton dispersions are plotted and compared to the bare cavity and exciton modes for three different detunings.

At resonance of the uncoupled modes ($E_{\mathrm{X}} = E_{\mathrm{Cav}}$), there is a minimal splitting between the eigenmodes. This results in $E_{\mathrm{UP}} - E_{\mathrm{LP}} = 2\hbar g(\boldsymbol{k})$, which is called normal mode- or Rabi-splitting [*]. The coefficients $\mathcal{C}_{\boldsymbol{k}}$ and $\mathcal{X}_{\boldsymbol{k}}$, known from the equations (2.18) and (2.19), are called Hopfield coefficients. For different detunings the percentage of the photonic and excitonic character of the LP and UP changes, as can be seen in Fig. 2-2 (d)-(f). The quadratic form of the Hopfield coefficients describe these percentages:

[*] Originally the term "Rabi splitting" comes from atomic physics, where at atomic resonance a splitting in energy occurs. In semiconductor microcavities, the term is frequently used and is an indicator for the system to be in the strong coupling regime. It can be identified by an anticrossing of exciton and photon resonance in the reflection spectra. In general, values of the Rabi splitting range from a few meV in GaAs microcavities with one QW to several hundreds of meV in organic systems with Frenkel excitons.

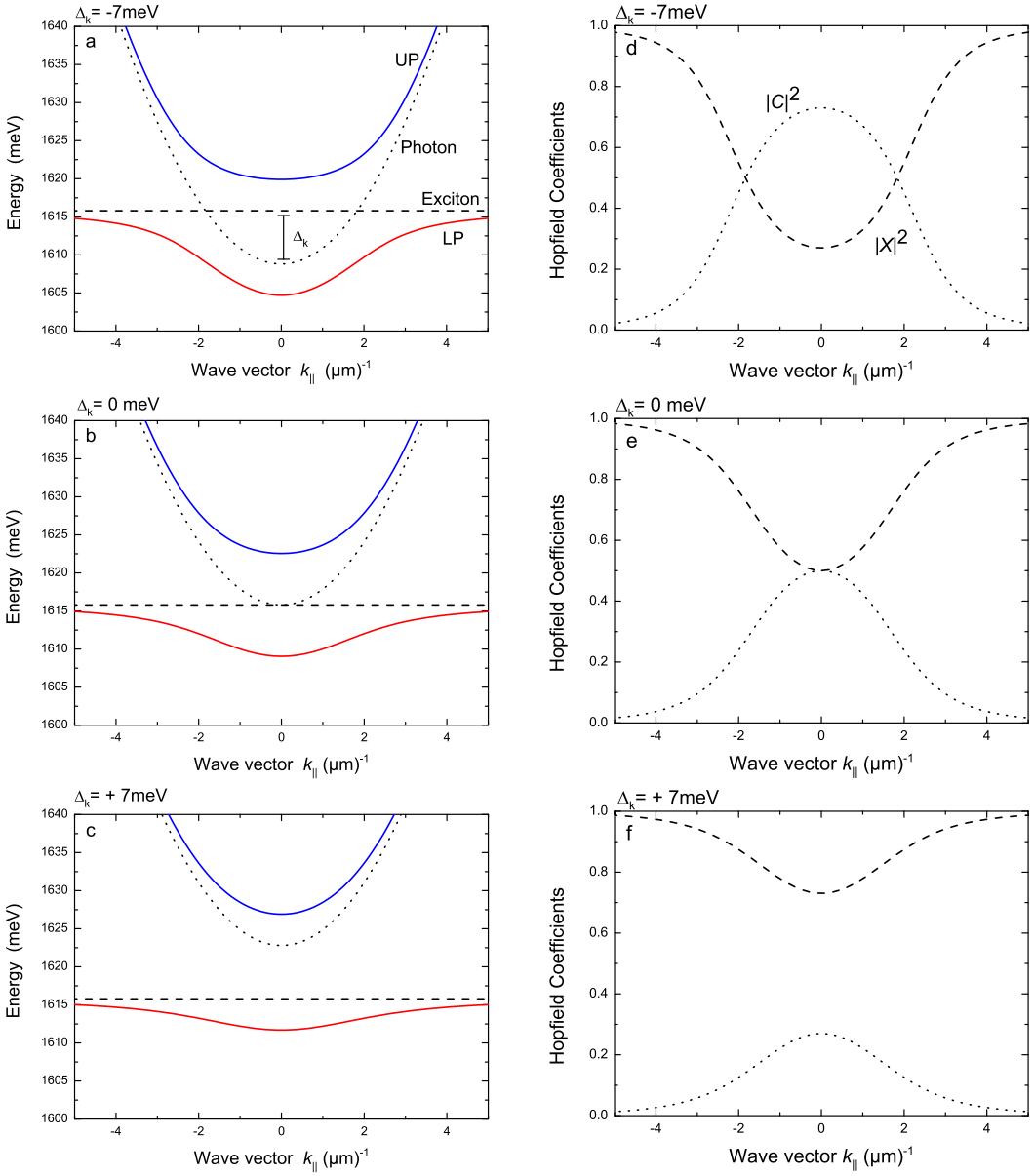

Figure 2-2: Polariton dispersions and squared Hopfield coefficients for negative detuning $\Delta_{\boldsymbol{k}} = -7$ meV [(a) and (d)], zero detuning $\Delta_{\boldsymbol{k}} = 0$ meV [(b) and (e)] and positive detuning $\Delta_{\boldsymbol{k}} = +7$ meV [(c) and (f)]. (a)–(c) The dotted line corresponds to the pure cavity mode while the dashed line represents the pure exciton mode. The red line is the lower polariton branch and the blue line indicates the upper polariton branch. (d)–(f) $|\mathcal{X}|^2$ (dashed) represents the excitonic content for the LP and the photonic fraction for the UP. The photonic fraction for the LP is given by $|\mathcal{C}|^2$ (dotted) while it stands for the excitonic content in the case of the UP. The figure is adapted from reference [42].

$$|\mathcal{X}_{\boldsymbol{k}}|^2 = \frac{1}{2}\left(1 + \frac{\Delta_{\boldsymbol{k}}}{\sqrt{\Delta_{\boldsymbol{k}} + 4\hbar^2 g(\boldsymbol{k})^2}}\right), \tag{2.23}$$

$$|\mathcal{C}_{\boldsymbol{k}}|^2 = \frac{1}{2}\left(1 - \frac{\Delta_{\boldsymbol{k}}}{\sqrt{\Delta_{\boldsymbol{k}} + 4\hbar^2 g(\boldsymbol{k})^2}}\right). \tag{2.24}$$

In the case of the LP, the photonic content is given by $|\mathcal{C}_{\boldsymbol{k}}|^2$ and the excitonic part by $|\mathcal{X}_{\boldsymbol{k}}|^2$. The photonic part decreases for increasing detuning, while the excitonic content raises. This behavior is exactly the opposite for the UP, where $|\mathcal{X}_{\boldsymbol{k}}|^2$ stands for the photonic fraction and $|\mathcal{C}_{\boldsymbol{k}}|^2$ for the excitonic one. In every case, $|\mathcal{C}_{\boldsymbol{k}}|^2 + |\mathcal{X}_{\boldsymbol{k}}|^2 = 1$ has to be fulfilled.

By changing the detuning the polaritons become more exciton- or photon-like. This influence can be expressed by the effective masses of the lower and upper polariton for $\mathbf{k} = 0$, as they are controlled by the detuning:

$$\frac{1}{m_{\mathrm{LP}}} = \frac{|\mathcal{X}_0|^2}{m_{\mathrm{X}}} + \frac{|\mathcal{C}_0|^2}{m_{\mathrm{Cav}}}, \tag{2.25}$$

$$\frac{1}{m_{\mathrm{UP}}} = \frac{|\mathcal{C}_0|^2}{m_{\mathrm{X}}} + \frac{|\mathcal{X}_0|^2}{m_{\mathrm{Cav}}}. \tag{2.26}$$

As the photon dispersion is bent more strongly at $\boldsymbol{k} = 0$ than that of the exciton and thus the effective photon mass is smaller than the exciton one, the mass of the lower polariton is approximately given by:

$$m_{\mathrm{LP}} = \frac{m_{\mathrm{Cav}}}{|\mathcal{C}_0|^2}. \tag{2.27}$$

Another important aspect has to be taken into account: since the photon in the cavity has a finite lifetime due to imperfect mirrors and the exciton can also decay nonradiatively, the dispersion relations of the polariton are modified to

$$E_{\mathrm{LP/UP}}(\boldsymbol{k}) = \frac{1}{2}\left(E_{\mathrm{X}} + E_{\mathrm{Cav}} + i(\gamma_{\mathrm{Cav}} + \gamma_{\mathrm{X}}) \pm \sqrt{4\hbar^2 g(\boldsymbol{k})^2 + (\Delta_{\boldsymbol{k}} + i(\gamma_{\mathrm{Cav}} - \gamma_{\mathrm{X}}))^2}\right), \tag{2.28}$$

where γ_{Cav} is the decay rate of the photon due to the finite reflectivity of the cavity mirrors and γ_{X} is the decay rate of the exciton due to interactions. For zero detuning $\Delta_{\boldsymbol{k}} = 0$ the equation is reduced to

$$E_{\mathrm{LP/UP}}(\boldsymbol{k}) = E_{\mathrm{Cav}} + \frac{i(\gamma_{\mathrm{Cav}} + \gamma_{\mathrm{X}})}{2} \pm \frac{1}{2}\sqrt{4\hbar^2\Omega^2 - i(\gamma_{\mathrm{Cav}} - \gamma_{\mathrm{X}})^2}. \tag{2.29}$$

Here $2\hbar\Omega = 2\hbar g(0)$ corresponds to the Rabi splitting at zero detuning. The splitting itself depends on the oscillator strength f_{osc}, the number N_{QW} of embedded QWs and the cavity length L_{eff} [43]:

$$\hbar\Omega \sim \sqrt{\frac{f_{\mathrm{osc}} N_{\mathrm{QW}}}{L_{\mathrm{eff}}}}. \tag{2.30}$$

The Eq. (2.29) provides solutions for two special cases: in the case of $\hbar\Omega > |\gamma_{\mathrm{X}} - \gamma_{\mathrm{Cav}}|/2$, the losses due to scattering and transmission are smaller than the oscillator strength and the strong coupling regime is reached. Otherwise if $\hbar\Omega < |\gamma_{\mathrm{X}} - \gamma_{\mathrm{Cav}}|/2$, the energy splitting disappears because the losses are too high. This is the so-called weak coupling regime with the bare cavity and exciton modes corrected by their altered lifetimes.

To determine the lifetime of the polaritons, the lifetime of the photon in the cavity $\tau_{\mathrm{Cav}} = \hbar/\gamma_{\mathrm{Cav}}$ and the lifetime of the exciton in the QW $\tau_{\mathrm{X}} = \hbar/\gamma_{\mathrm{X}}$ can be used. In analogy to Eq. (2.25) one obtains for the lower polariton branch:

$$\frac{1}{\tau_{\mathrm{LP},\boldsymbol{k}}} = \frac{|\mathcal{X}|^2}{\tau_{\mathrm{X}}} + \frac{|\mathcal{C}|^2}{\tau_{\mathrm{Cav}}}. \tag{2.31}$$

Since the lifetime of the photon in a planar microcavity ($\tau_{\mathrm{Cav}} \approx 1 - 10$ ps) is much shorter than the lifetime of the exciton ($\tau_{\mathrm{X}} \approx 1$ ns), the polariton lifetime is almost completely determined by $\tau_{\mathrm{LP},\boldsymbol{k}} \approx \tau_{\mathrm{Cav}}/|\mathcal{C}|^2$.

2.1.4 Scattering Mechanisms in Microcavities

The polariton energy dispersion relation can be gathered from angle-resolved micro-photoluminescence measurements. Hereby, the semiconductor sample is optically excited either resonantly near the bottleneck region in the trap of the lower polariton branch or nonresonantly at higher energies.

In the case of nonresonant excitation (Fig. 2-3) a large number of free electron-hole pairs is generated - called electron-hole plasma. These free pairs lose their coherence due to strong carrier-carrier interaction. Their initial carrier temperature lies in the order of several thousands of Kelvin and, therefore, they are also called hot carriers [45]. To create excitons in the quantum well these hot carriers have to thermalize by emitting optical phonons through interaction with the lattice. This phonon relaxation process occurs on a subpicosecond timescale. It is followed by a slower scattering with acoustic phonons leading to a formation of a thermal exciton reservoir with a fixed temperature at high momentum. The total process of reaching the lattice temperature takes about hundreds of picoseconds.

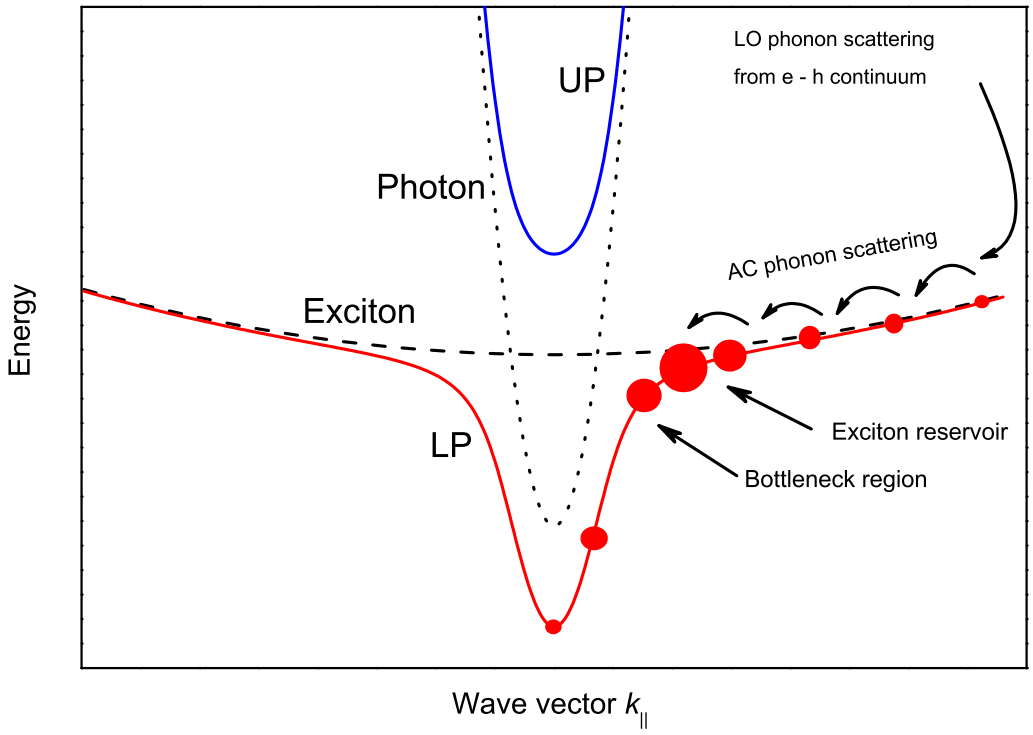

Figure 2-3: Schematic diagram of the relaxation processes in a QW microcavity under nonresonant excitation. The red and blue curves represent the LP and UP dispersions, respectively. The dashed line stands for the uncoupled exciton dispersion while the dotted line corresponds the the uncoupled cavity photon mode. Under nonresonant excitation hot electron-hole pairs are created at high energies and relax towards the QW exciton dispersion via LO phonon emission. The created excitons relax under acoustic (AC) phonon emission and populate the exciton reservoir. The bottleneck effect leads to a less effective AC phonon scattering into the lower polariton branch illustrated by the size of the circles which indicate the state of occupancy. The figure is adapted from reference [44].

The Bragg mirrors of the cavity reflect the light only within a finite angular cone, so that the excitons couple strongly to the light field as soon as their in-plane wave vector matches the one corresponding to the angular cone. Since the formed polaritons at high momentum are exciton-like, the thermalization via acoustic phonons stays efficient until the region of the anti-crossing point is reached. Due to their light mass in the region of the polariton dispersion minimum, the relaxation with acoustic phonons is slower than the decay time of the polaritons. This leads to a less populated ground state compared to the edge of the polariton trap at the anti-crossing point. This phenomenon of a suppressed relaxation towards the ground state is called bottleneck effect. Tassone et al. [46] first introduced the effect for microcavity polaritons and a few years later Tartakovskii et al. [47] and Müller et al. [48] observed it experimentally. The slow relaxation for small values of the momentum is the reason why a thermal equilibrium can not be achieved in this region. By use of high excitation power it is possible to suppress the bottleneck effect by an increase in polariton-polariton and polariton-free-carrier interaction.

When a considerable number of excitons is collected in the excitonic reservoir at high momentum, the coupling between photon and exciton is weakened. Thus, the number of QWs in the microcavity must be large enough to reach excitation powers which enable a suppression of the bottleneck effect without leaving the strong coupling regime. The occurring polariton-polariton interaction at high excitation powers leads to their separation in momentum space: one of the polaritons is scattered into the parabolic-shaped dispersion valley, while the other one scatters into the excitonic-like dispersion part of the lower polariton branch and correspondingly obtains a higher energy level. Another scattering mechanism to overcome the bottleneck effect is based on polariton-free-carrier interactions. Here, polaritons scatter with hot carriers (e.g. electrons) created by the optical excitation [49]. Because of the small effective mass of the interacting electron which arranges an energy dissipation via wave vector exchange, it is possible to extend the polariton lifetime at moderate densities. This in turn is helpful for overcoming the bottleneck effect. Since polaritons are bosons the bosonic final state stimulation plays a significant role which leads to a macroscopic occupation of the ground state and therefore to a build-up of a coherent Bose-Einstein condensate. The basic concept of Bose-Einstein condensation and its occurring characteristics, the equilibrium conditions for polariton BEC will be discussed in detail in the next sections.

For resonant excitation, polaritons are injected directly at the polariton trap, as shown in Fig. 2-4. Hereby, a population of the exciton reservoir and the mechanism to bypass the bottleneck are not necessary anymore. Via polariton-polariton scattering a ground-state population is finally achieved. This parametric process leads to stimulation of the $(k_{||} = 0)$-state and a build-up of macroscopic coherence. The macroscopic population of the ground state is accompanied by a nonlinearity in the emitted intensity.

To describe the polariton relaxation mentioned above, the so-called semi-classical Boltzmann rate equations for bosons and fermions can be used, provided that only weak interactions play a role. In the strong coupling regime the interactions between polaritons are weak and, therefore, the Boltzmann equations are valid. The corresponding rate equations for the time-dependent number of bosons and fermions at $\boldsymbol{k}$ are given by [32]:

$$\frac{dn_{\boldsymbol{k}}}{dt} = P_{\boldsymbol{k}} - \Gamma_{\boldsymbol{k}} n_{\boldsymbol{k}} - n_{\boldsymbol{k}} \sum_{\boldsymbol{k}'} W_{\boldsymbol{k}\to\boldsymbol{k}'}(1 + n_{\boldsymbol{k}'}) + (1 + n_{\boldsymbol{k}}) \sum_{\boldsymbol{k}'} W_{\boldsymbol{k}'\to\boldsymbol{k}} n_{\boldsymbol{k}'} \qquad \text{(Bosons)}, \tag{2.32}$$

$$\frac{dn_{\boldsymbol{k}}}{dt} = P_{\boldsymbol{k}} - \Gamma_{\boldsymbol{k}} n_{\boldsymbol{k}} - n_{\boldsymbol{k}} \sum_{\boldsymbol{k}'} W_{\boldsymbol{k}\to\boldsymbol{k}'}(1 - n_{\boldsymbol{k}'}) + (1 - n_{\boldsymbol{k}}) \sum_{\boldsymbol{k}'} W_{\boldsymbol{k}'\to\boldsymbol{k}} n_{\boldsymbol{k}'} \qquad \text{(Fermions)}, \tag{2.33}$$

where $P_{\boldsymbol{k}}$ is the pumping generation term, $\Gamma_{\boldsymbol{k}}$ is the particle decay rate, and $W_{\boldsymbol{k}\to\boldsymbol{k}'}$

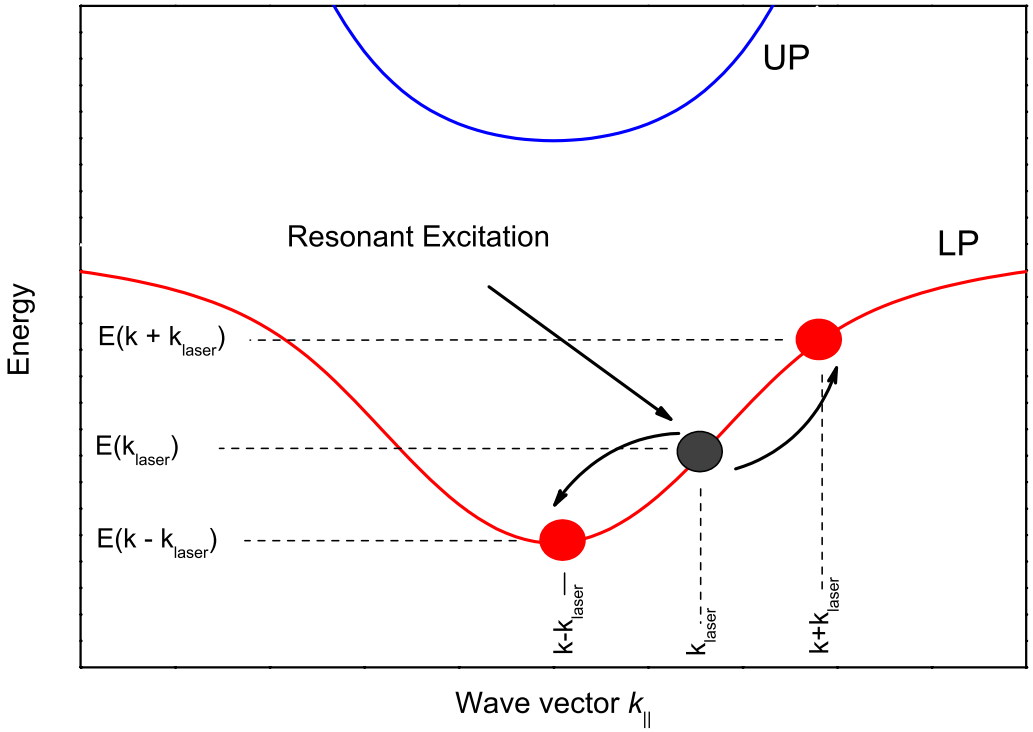

Figure 2-4: Schematic diagram of the relaxation processes in a QW microcavity under resonant excitation. The red and blue curves represent the LP and UP dispersion, respectively. Due to momentum- and energy conservation, one polariton gets scattered to $(\boldsymbol{k}_{||} - \boldsymbol{k}_{||,\mathrm{laser}})$ and the other one to $(\boldsymbol{k}_{||} + \boldsymbol{k}_{||,\mathrm{laser}})$.

is the total scattering rate between the $\boldsymbol{k}$- and $\boldsymbol{k}'$-state. The total scattering rate consists of the scattering rates of the different relaxation mechanisms for the polariton

$$W_{\boldsymbol{k}\to\boldsymbol{k}'} = W^{\mathrm{Phonon}}_{\boldsymbol{k}\to\boldsymbol{k}'} + W^{\mathrm{Polariton}}_{\boldsymbol{k}\to\boldsymbol{k}'} + W^{\mathrm{Electron}}_{\boldsymbol{k}\to\boldsymbol{k}'}, \tag{2.34}$$

and can be calculated with Fermi's Golden rule, see details in Ref. [50].

2.1.5 Breakdown of Strong Coupling Regime

With increasing excitation density the oscillator strength f_{osc} gets renormalized due to the presence of an electron-hole plasma. This means that with increasing excitation power the concentration of electron-hole pairs increases and starts to screen the Coulomb attraction, so that an exciton state is no longer stable. The critical density at which the exciton becomes unstable is called Mott-density, the corresponding transition is named as Mott-transition [51].

The change in the oscillator strength leads to a reduction in the vacuum Rabi splitting and the system passes from the strong into the weak coupling regime [52]. Due to the smaller Rabi splitting the coupling is weaker than the photon decay rate in the cavity and nonradiative recombination rate of excitons. Hence, the

anti-crossing behavior is replaced by the crossing of the bare cavity and exciton modes.

The light-matter interaction in a weakly coupled system can be described by Fermi's Golden rule, since the coupled and uncoupled eigenstates are similar. It gives the probability of the transition from an initial $|i\rangle$ to a continuum of final $|f\rangle$ states, whose coupling is described by a Hamiltonian H':

$$\frac{1}{\tau} = \frac{2\pi}{\hbar}|\langle f|H'|i\rangle|^2\rho_{\mathrm{f}}, \tag{2.35}$$

with ρ_{f} as the density of final states.

For QWs embedded in a microcavity acting as optical emitter, it is given by the electric dipole $\boldsymbol{d}$ and light field $\mathbf{E}(\boldsymbol{r},t)$ at the position $\boldsymbol{r}$ and time t. The emission energy of the emitter is designated by $\hbar\omega_{\mathrm{emit}}$. The spontaneous emission rate is defined as

$$\gamma_{\mathrm{sp}} = \frac{1}{\tau} = \frac{2\pi}{\hbar}|\boldsymbol{d}\cdot\boldsymbol{E}(\boldsymbol{r},t)|^2\rho_{\mathrm{Cav}}(\omega_{\mathrm{emit}}), \tag{2.36}$$

with the density of states ρ_{Cav} of the light field being in resonance with the emitter. In terms of the fundamental mode frequency ω_{Cav} and quality factor $Q = \omega_{\mathrm{Cav}}/\Delta\omega_{\mathrm{Cav}}$, the photon density of states in the cavity reads

$$\rho_{\mathrm{Cav}}(\omega) = \frac{2}{\pi}\frac{\Delta\omega_{\mathrm{Cav}}}{4(\omega-\omega_{\mathrm{Cav}})^2+\Delta\omega_{\mathrm{Cav}}^2}. \tag{2.37}$$

The spontaneous emission rate into the cavity differs from the one into the vacuum, since the resonator influences the photon density of states. When the emitter is out of resonance with the cavity mode, the spontaneous emission rate into the cavity is reduced compared to the one into vacuum. At resonance between the emitter and the cavity mode the spontaneous emission rate is enhanced with respect to the one in vacuum. This effect of enhancement in a cavity is known as the Purcell effect and is described by the Purcell factor F_{P} [53]:

$$F_{\mathrm{P}} = \frac{3Q(\lambda_{\mathrm{Cav}}/n)^3}{4\pi^2 V_{\mathrm{eff}}}. \tag{2.38}$$

Here, λ_{Cav} is the cavity wavelength, n the refractive index, and V_{eff} the effective mode volume of the cavity, which is defined by L_{eff}. As one can clearly see from Eq. (2.38), the enhancement solely depends on parameters of the cavity. For planar microcavities the Purcell factor is generally of the order of unity [54] while it can

reach values of about 30 for micropillars[†] [55].

Note, the system of a microcavity in the weak coupling regime will start to lase if, due to high excitation densities, electronic population inversion is reached. The conditions for stimulated emission in semiconductors is discussed in the work of Bernard and Duraffourg [56]. In the case of stimulated emission a photon in the cavity forces the active medium to release another photon with the same polarization and which is in phase with the original photon. On account of energy conservation, an excited electron falls back into the valence band. The onset of coherent light emission due to photon lasing becomes visible by a nonlinear increase in the input-output curve, where the PL intensity is plotted against the excitation power.

2.2 Bose-Einstein Condensate

Thermodynamics can force bosons to undergo a phase transition and build up a macroscopic population of their ground state. Reaching a critical density n_c or temperature T_c, a Bose-Einstein condensate (BEC) is formed. It is characterized by e.g. a macroscopic coherence and the macroscopic occupation of the lowest state by bosons. Polaritons can be treated as bosons in the low-density limit and, therefore, they are perfect candidates for showing Bose-Einstein condensation. A condensate in a microcavity system represents a coherent-light-emitter with the advantage of having a lower threshold carrier density compared to photon lasing using the same structure. Furthermore, due to their half-matter nature polariton condensate systems are perfect candidates for cavity quantum electrodynamics.

This section gives an overview of the concept of Bose-Einstein condensation in general and case of confined polaritons in a 2D system. As a basic reference for the discussion in this chapter, the publications from Deng [33], Kavokin [32] and Wouters [57] were taken, unless specified otherwise.

2.2.1 Ideal Bose Gas

Consider a gas with N free, identical and noninteracting bosons in thermal equilibrium at a temperature T in a volume V. The distribution of these bosons is then as follows:

$$f_b(\boldsymbol{k}, \mu, T) = \frac{1}{e^{\frac{E(\boldsymbol{k})-\mu}{k_B T}} - 1}. \tag{2.39}$$

[†]Micropillars are further dimensional reduced cavities created by plasma etching of a planar microcavity.

$E(\boldsymbol{k}) = \hbar^2\boldsymbol{k}^2/2m$ is the energy-momentum dispersion of the free particles and μ the chemical potential, where $-\mu$ is the energy needed to add a further boson to the system. The total number of bosons is given by

$$N = \sum_{\mathbf{k}} f_{\mathrm{b}}(\mathbf{k}, \mu, T). \tag{2.40}$$

The number of bosons in the lowest state with energy E_0 is determined by

$$N_0 = \frac{1}{e^{\frac{E_0-\mu}{k_{\mathrm{B}}T}} - 1}. \tag{2.41}$$

It is possible to separate the ground state from all excited states:

$$N = N_0 + \sum_{\boldsymbol{k}, k\neq 0} N_k \tag{2.42}$$

$$= N_0 + \sum_{\boldsymbol{k}, k\neq 0} f_{\mathrm{b}}(T, \mu, \boldsymbol{k}). \tag{2.43}$$

In the case of bosons in a 3D system with size L and in the thermodynamical limit $L^3 \to \infty$, the total number of bosons occupying the excited states takes the following form:

$$N_k = 4\pi \left(\frac{L}{2\pi}\right)^3 \int_0^\infty dk \frac{1}{\boldsymbol{k}^2} f_{\mathrm{b}}(\boldsymbol{k}, T, \mu), \tag{2.44}$$

$$N_E = 4\pi \left(\frac{L}{2\pi}\right)^3 \frac{1}{2} \left(\frac{2m}{\hbar^2}\right)^{\frac{3}{2}} \int_0^\infty dE \sqrt{E} f_b(E, T, \mu). \tag{2.45}$$

Considering now the density of the excited states, Eq. (2.45) turns into

$$n_E = \frac{1}{4\pi^2} \left(\frac{2m}{\hbar^2}\right)^{\frac{3}{2}} \int_0^\infty dE\, \sqrt{E} \frac{1}{e^{\frac{E-\mu}{k_{\mathrm{B}}T}} - 1}. \tag{2.46}$$

The integral reaches a maximum value when the chemical potential μ is equal to E_0. If this critical density n_{c} is achieved, each further added particle has to occupy the ground state in order to fulfill the Bose-Einstein distribution. So, there is a macroscopic occupation of the ground state. This macroscopic occupation caused by saturation of the excited states is the phase transition known as Bose-Einstein condensation.

The critical temperature T_{c} of Bose-Einstein condensation can be phenomenologically described by the distance between the free identical bosons. Each boson has a certain expansion - the thermal de Broglie wavelength $\lambda_{dB} = \sqrt{(2\pi\hbar^2)/(mk_BT)}$ [59]. It characterizes the thermal broadening of the particle wave function.

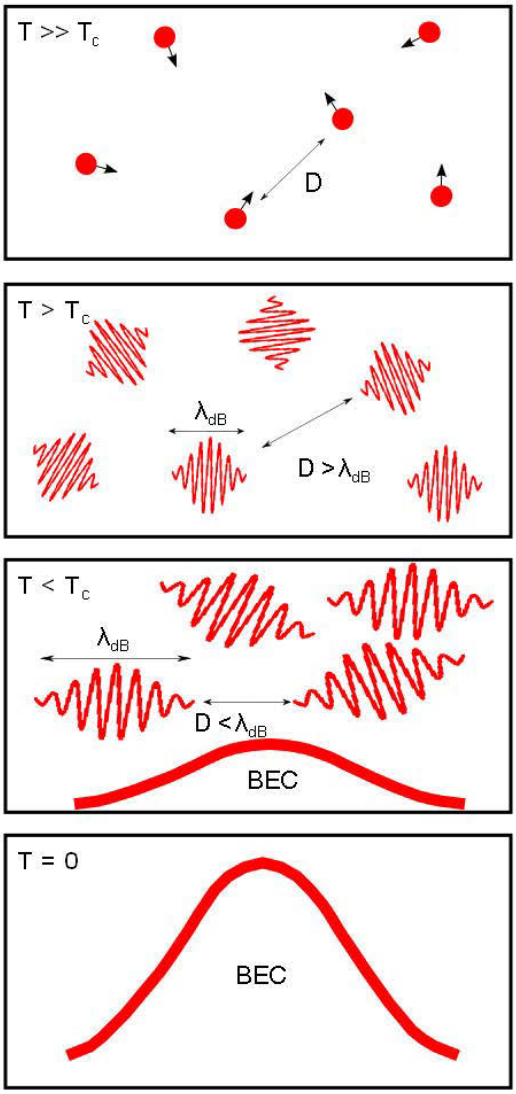

Figure 2-5: A phenomenological approach of Bose-Einstein condensation for an ideal Bose gas at different temperatures. For high temperatures $T \gg T_c$ (top panel) the particles can be described as point particles with an inter-particle distance D. For lower temperatures $T > T_c$ (2nd panel) the particles can no longer be treated as point particles but as wave packets. Their thermal de Broglie wavelength is still smaller than the particle distance. This is changed for temperatures below the critical temperature $T < T_c$ (3rd panel from top). Here, the averaged particle distance is in the order of the λ_{dB} and the different wave packets can overlap. A collective ground-state wave function is formed - the Bose-Einstein condensate. At absolute zero temperature all particles join this ground-state wave function (bottom panel). The figure is adapted from reference [58].

In the case of an inter-particle distance D in the order of the de Broglie wavelength, the particles interfere with each other and a macroscopic occupation of the ground state occurs. For $n_c \propto \lambda_{dB}(T_c)^{-d}$ with d as the system dimension, the

critical temperature is proportional to

$$k_{\mathrm{b}} T_{\mathrm{c}} \propto 3.31 \frac{\hbar^2 n^{2/d}}{m}, \tag{2.47}$$

and, therefore, it varies inversely with the particle mass m.

Beside the macroscopic occupation of the ground state, a further indicator for the occurrence of BEC is the off-diagonal-long-range-order (ODLRO) or long-range-phase-coherence in the condensed state. When a system shows ODLRO, its single-particle density matrix

$$\rho(\boldsymbol{r}, \boldsymbol{r}') \equiv \mathrm{Tr}\{\hat{\rho}\hat{\Psi}^\dagger(\boldsymbol{r})\hat{\Psi}(\boldsymbol{r}')\} \equiv \langle \hat{\Psi}^\dagger(\boldsymbol{r})\hat{\Psi}(\boldsymbol{r}')\rangle \tag{2.48}$$

has an eigenvalue which is proportional to the absolute number of particles in the system. Here, the density operator is $\hat{\rho}$, and $\hat{\Psi}^\dagger$ and $\hat{\Psi}$ are the creation and annihilation field operators, respectively. In principle the matrix in Eq. (2.48) expresses the probability amplitude that a system will stay in the same state, even if a particle is removed at position $\boldsymbol{r}$ and added at $\boldsymbol{r}'$. For the normal states the density matrix has a nonvanishing value, when the distance $|\boldsymbol{r} - \boldsymbol{r}'|$ is in the order of the de Broglie wavelength. It tends to zero for distances well above the de Broglie wavelength of the bosons. This stands in contrast to the behavior in the condensed state, where the single-particle density matrix has a nonzero value, even in the case of $|\boldsymbol{r} - \boldsymbol{r}'| \to \infty$. When a particle is inserted at $\boldsymbol{r}$ into the condensate and a particle at $\boldsymbol{r}'$ is removed, a quantum coherent amplitude and phase still exist.

A further attribute of BEC is the spontaneous gauge-symmetry breaking causing a phase transition. To describe this symmetry breaking the field operator $\hat{\Psi}(\boldsymbol{r})$ is separated into the ground state and uncondensed excited states:

$$\hat{\Psi}(\boldsymbol{r}) = \phi_0(\boldsymbol{r})\hat{a}_0 + \sum_{i \neq 0} \phi_i(\boldsymbol{r})\hat{a}_i^\dagger \tag{2.49}$$

with the single particle wave function ϕ and the creation (annihilation) operator $\hat{a}^\dagger$ ($\hat{a}$), respectively. Making use of the Bogoliubov approximation [60] with

$$\hat{a}_0 = \sqrt{N_0} \quad \text{and} \quad N_0 = \langle \hat{a}_0^\dagger \hat{a}_0 \rangle, \tag{2.50}$$

and in the case of a macroscopic occupation of the ground state ($N_0 \gg 1$), the field operator can be defined as follows:

$$\hat{\Psi}(\boldsymbol{r}) = \Psi_0(\boldsymbol{r}) + \delta\hat{\Psi}(\boldsymbol{r}). \tag{2.51}$$

$\Psi_0 = \sqrt{N_0}\phi_0$ is the wave function of the condensate and order parameter of the phase transition. The order parameter has to fulfill the requirement to be zero above the phase transition and nonzero below. For the wave function of the condensate the relation

$$\Psi_0 = |\Psi_0(\boldsymbol{r})|e^{iS(\boldsymbol{r})} \tag{2.52}$$

is essential, with $|\Psi_0(\boldsymbol{r})|^2 = n_0$ and $S(\boldsymbol{r})$ as the phase connected to the coherence and superfluidity phenomenon of the condensate. The absolute phase of the condensate is irrelevant and an arbitrary phase factor $e^{i\alpha}$ can be added without changing physical characteristics. Assuming a certain phase $S(\boldsymbol{r})$ at the phase transition of the BEC in absence of a preferred phase value is a spontaneous breaking of the gauge symmetry. To describe the spontaneous symmetry breaking the condensate is characterized as a coherent state (or being rather close to one) and the order parameter is chosen in a way that it matches the expectation value of the field operator $\langle\hat{\Psi}(\boldsymbol{r})\rangle$. Above the phase transition the ground state is occupied by statistically independent number eigenstates. This changes below the transition, where the ground state can be described as a coherent state with a well-defined phase, it is given by [61]

$$\hat{a}|\alpha\rangle = \alpha|\alpha\rangle. \tag{2.53}$$

Here, $|\alpha|^2 = N_0$ is the average particle number in the condensed state. The coherent state can be expressed by the particle-number eigenstate:

$$|\alpha\rangle = e^{\frac{-|\alpha|^2}{2}} \sum_n \frac{\alpha^n}{\sqrt{n!}}|n\rangle. \tag{2.54}$$

For a condensate in a coherent state, the time dependence of the order parameter can be assumed to

$$\Psi_0(\boldsymbol{r},t) \equiv \langle\alpha|\phi_0\hat{a}_0|\alpha\rangle = \langle\hat{\Psi}(\boldsymbol{r})\rangle e^{-i(E_N - E_{N-1})t/\hbar}. \tag{2.55}$$

If $N_0 \gg 1$, the energy term in Eq. (2.55) corresponds to the chemical potential:

$$E_N - E_{N-1} \simeq \frac{\partial E_N}{\partial N} = \mu. \tag{2.56}$$

Since the expectation value of the field operator $\langle\hat{\Psi}(\boldsymbol{r})\rangle$ equals the order parameter, for the time-dependent wave function of the condensate follows:

$$\Psi_0(\boldsymbol{r},t) = \Psi_0(\boldsymbol{r})e^{-i\mu t/\hbar}. \tag{2.57}$$

In summary, BEC is observed when a macroscopic number of particles occupy

the ground state and a single-particle wave function is able to describe this condensate. At the phase transition, there is a build-up of coherence over a macroscopic distance.

2.2.2 Weakly Interacting Bose Gas

The ideal Bose gas is a description of the condensation phenomenon in theory, but it is not an explanation for a real experimental system, since there will always be at least weakly repulsive interactions among the bosons. In 1947, Bogoliubov presented a mean-field description for a weakly interacting Bose gas on macroscopic scale.

The field operator is used to express the Hamiltonian of two weakly interacting bosons in the following form:

$$\hat{H} = \int \left(\frac{\hbar^2}{2m} \nabla \hat{\Psi}^\dagger \nabla \hat{\Psi} \right) dr + \frac{1}{2} \int \hat{\Psi}^\dagger \hat{\Psi}^{\dagger\prime} V(\boldsymbol{r}' - \boldsymbol{r}) \hat{\Psi} \hat{\Psi}' dr\, dr', \tag{2.58}$$

where $V(\boldsymbol{r}' - \boldsymbol{r})$ is the interaction potential of both bosons; it is considered as weak and short-ranged. Using the description

$$\hat{\Psi}(\boldsymbol{r}) = \frac{1}{\sqrt{L^3}} \sum_{\boldsymbol{k}} \hat{a}_{\boldsymbol{k}} e^{i\boldsymbol{k}\,\boldsymbol{r}} \tag{2.59}$$

to express the field operator, Eq. (2.58) can be written as

$$\hat{H} = \sum_{\boldsymbol{k}} \frac{\hbar^2 \boldsymbol{k}^2}{2m} \hat{a}^\dagger_{\boldsymbol{k}} \hat{a}_{\boldsymbol{k}} + \frac{1}{2L^3} \sum_{\boldsymbol{k},\boldsymbol{k}',\boldsymbol{q}} V_{\boldsymbol{q}} \hat{a}^\dagger_{\boldsymbol{k}+\boldsymbol{q}} \hat{a}^\dagger_{\boldsymbol{k}'-\boldsymbol{q}} \hat{a}_{\boldsymbol{k}} \hat{a}_{\boldsymbol{k}'} \tag{2.60}$$

with the Fourier-transformed potential $V_{\boldsymbol{q}} = \int V(\boldsymbol{r}) e^{-(iqr)/\hbar} dr$. Since the common two-body potential has a short-range term r_0, which is resulting in a difficulty to solve the Schrödinger equation on a microscopic scale for a cold and dilute system, an effective potential $V_{\text{eff}}(\boldsymbol{r})$ is assumed for small momentum where q is much smaller than $\hbar/r_0$. The macroscopic properties of the condensate are fully determined for the momentum $q = 0$. Hence, the potential can be written as

$$V_0 = \int V_{\text{eff}}(\boldsymbol{r}) dr \tag{2.61}$$

and for the Hamiltonian:

$$\hat{H} = \sum_{\boldsymbol{k}} \frac{\hbar^2 \boldsymbol{k}^2}{2m} \hat{a}^\dagger_{\boldsymbol{k}} \hat{a}_{\boldsymbol{k}} + \frac{V_0}{2L^3} \sum_{\boldsymbol{k},\boldsymbol{k}',\boldsymbol{q}} \hat{a}^\dagger_{\boldsymbol{k}+\boldsymbol{q}} \hat{a}^\dagger_{\boldsymbol{k}'-\boldsymbol{q}} \hat{a}_{\boldsymbol{k}} \hat{a}_{\boldsymbol{k}'}. \tag{2.62}$$

With the Bogoliubov approximation, already mentioned in Eq. (2.50) and the Bogoliubov ansatz (2.51), the ground-state energy in the lowest mean-field ap-

proximation can be evaluated to

$$E_{0,0} = \frac{g}{2L^3} N_0^2 \simeq \frac{g}{2L^3} N^2. \tag{2.63}$$

$N_0 = N$ is valid, since in a cold and diluted system the occupation of the excited states is negligible. g is the potential expressed by the Born approximation to

$$g = V_0 = \frac{4\pi\hbar^2 a}{m} \tag{2.64}$$

where a is the s-wave scattering length. The chemical potential of the system is therefore given by

$$\mu = \frac{\partial E_0}{\partial N} = gn \tag{2.65}$$

with the density of the gas $n = N/V$. Using the Hamiltonian from Eq. (2.62) and the Heisenberg equation of motion

$$i\hbar \frac{\partial}{\partial t} \hat{\Psi}(\boldsymbol{r}, t) = \left[\hat{\Psi}(\boldsymbol{r}, t), \hat{H} \right], \tag{2.66}$$

the time development of the macroscopic and also classical wave function of the condensate is given by the Gross-Pitaevskii equation:

$$i\hbar \frac{\partial}{\partial t} \Psi_0(\boldsymbol{r}, t) = \left(-\frac{\hbar^2 \nabla^2}{2m} + g|\Psi_0(\boldsymbol{r}, t)|^2 \right) \Psi_0(\boldsymbol{r}, t). \tag{2.67}$$

To be able to describe also the excitation spectrum a higher order of the mean-field approximation has to be considered. Therefore, the normalization relation is used

$$\hat{a}_0^\dagger \hat{a}_0 + \sum_{\boldsymbol{k} \neq 0} \hat{a}_{\boldsymbol{k}}^\dagger \hat{a}_{\boldsymbol{k}} = |\alpha|^2 + \sum_{\boldsymbol{k} \neq 0} \hat{a}_{\boldsymbol{k}}^\dagger \hat{a}_{\boldsymbol{k}} = N. \tag{2.68}$$

This leads to the following expression of the higher-order mean-field Hamiltonian [62]:

$$\hat{H} = \frac{g}{2L^3} N^2 + \sum_{\boldsymbol{k} \neq 0} \frac{\hbar^2 \boldsymbol{k}^2}{2m} \hat{a}_{\boldsymbol{k}}^\dagger \hat{a}_{\boldsymbol{k}} + \frac{1}{2} gn \sum_{\boldsymbol{k} \neq 0} \left(2\hat{a}_{\boldsymbol{k}}^\dagger \hat{a}_{\boldsymbol{k}} + \hat{a}_{\boldsymbol{k}}^\dagger \hat{a}_{-\boldsymbol{k}}^\dagger + \hat{a}_{\boldsymbol{k}} \hat{a}_{-\boldsymbol{k}} + \frac{mgn}{\hbar^2 \boldsymbol{k}^2} \right) \tag{2.69}$$

The third term in the Hamiltonian corresponds to the self-energy of the excited states caused by interaction. At momentum $\boldsymbol{k}$ there is the creation of the excited states, while simultaneously at $-\boldsymbol{k}$ the annihilation of the excited states takes place. Making use of the linear Bogoliubov transformation, the Hamiltonian can

be diagonalized with

$$\hat{a}_{\boldsymbol{k}} = u_{\boldsymbol{k}}\hat{b}_{\boldsymbol{k}} + v^*_{-\boldsymbol{k}}\hat{b}^\dagger_{-\boldsymbol{k}}, \tag{2.70}$$

$$\hat{a}^\dagger_{\boldsymbol{k}} = u^*_{\boldsymbol{k}}\hat{b}^\dagger_{\boldsymbol{k}} - v_{-\boldsymbol{k}}\hat{b}_{-\boldsymbol{k}}. \tag{2.71}$$

With $u_{\boldsymbol{k}} = u_{-\boldsymbol{k}}$, $v_{\boldsymbol{k}} = v_{-\boldsymbol{k}}$ and $|u_{\boldsymbol{k}}|^2 - |v_{-\boldsymbol{k}}|^2 = 1$ the new operators fulfill the bose commutation relations, as the operators before. To achieve a vanishing of the nondiagonal terms in Eq. (2.69) the coefficients have to satisfy

$$\frac{gn}{2}\left(|u_{\boldsymbol{k}}|^2 + |v_{-\boldsymbol{k}}|^2\right) + \left(\frac{\hbar^2\boldsymbol{k}^2}{2m} + gn\right)u_{\boldsymbol{k}}v_{-\boldsymbol{k}} = 0, \tag{2.72}$$

which leads to coefficients that are determined by

$$u_{\boldsymbol{k}}, v_{-\boldsymbol{k}} = \pm\sqrt{\left(\frac{\frac{\hbar^2\boldsymbol{k}^2}{2m} + gn}{2E_{\mathrm{Bog}}(\boldsymbol{k})} \pm \frac{1}{2}\right)}. \tag{2.73}$$

$E_{\mathrm{Bog}}(\boldsymbol{k})$ is known as the Bogoliubov dispersion law of the excitation spectrum and is defined as

$$E_{\mathrm{Bog}}(\boldsymbol{k}) = \sqrt{\frac{gn}{m}\hbar^2\boldsymbol{k}^2 + \left(\frac{\hbar^2\boldsymbol{k}^2}{2m}\right)^2}. \tag{2.74}$$

Using now the Bogoliubov transformation and the determination of the coefficients the Hamiltonian turns out to be

$$\hat{H} = E_{0,1} + \sum_{\boldsymbol{k}\neq 0} E_{\mathrm{Bog}}(\boldsymbol{k})\hat{b}^\dagger_{\boldsymbol{k}}\hat{b}_{\boldsymbol{k}}. \tag{2.75}$$

With $E_{0,1}$ as the ground-state energy in a higher-order mean-field approximation, one obtains

$$E_{0,1} = E_{0,0} + \frac{1}{2}\sum_{\boldsymbol{k}\neq 0}\left[E_{\mathrm{Bog}}(\boldsymbol{k}) - gn - \frac{\hbar^2\boldsymbol{k}^2}{2m} + \frac{mg^2n^2}{\hbar^2\boldsymbol{k}^2}\right]. \tag{2.76}$$

For low momentum

$$k \lesssim \frac{1}{\xi} = \frac{\sqrt{2mgn}}{\hbar}, \tag{2.77}$$

the Bogoliubov dispersion law has a phonon-like behavior

$$E_{\mathrm{Bog}}(\boldsymbol{k}) = \sqrt{\frac{gn}{m}}\hbar\boldsymbol{k} = c_s\hbar\boldsymbol{k} \tag{2.78}$$

with the sound velocity c_s. ξ is called the healing length and plays an important role in superfluidity. It also characterizes the transition from the phonon-like

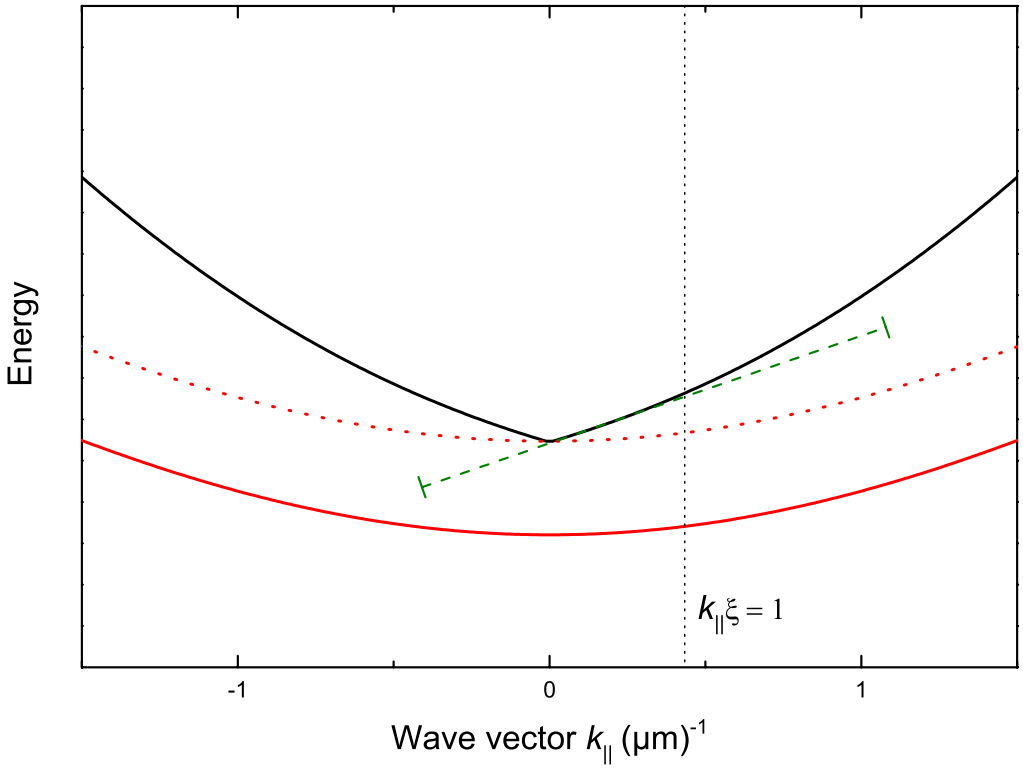

Figure 2-6: Exemplary polariton dispersion representing the lower polariton branch (red line), the blue shifted lower polariton branch (red dotted line) and the Bogoliubov dispersion (black line) with a linear guide to the eye (green dashed line). The transition from the linear behavior for small momentum towards a parabolic one at high momentum is marked with a black dotted line. Here, $\boldsymbol{k}_{||}\xi$ has a value of 1.

behavior to a free-particle one for higher momenta:

$$E_{\mathrm{Bog}}(\boldsymbol{k}) = \frac{\hbar^2 \boldsymbol{k}^2}{2m} + gn. \tag{2.79}$$

2.2.3 Superfluidity

Superfluidity is deeply connected to BEC, but both do not require each other; they also exist on their own. A superfluid can flow through small capillaries without any energy dissipation. One of the main and mostly referred criteria for superfluidity follows the suggestions of Landau; he drew a connection between superfluidity and BEC for the first time.

A large body with mass M is considered to flow with velocity $\boldsymbol{v}_{\mathrm{i}}$ into a liquid. As soon as the flow is able to induce excitations in the liquid, dissipation will occur. If the motion is below a so-called Landau critical velocity, the excitation of any particle is not possible and, therefore, the motion is without any energy dissipation. This critical velocity can be established by letting the mass M scatter

with a particle of the liquid. This scattering leads to a change of the velocity from $\boldsymbol{v}_\mathrm{i}$ to $\boldsymbol{v}_\mathrm{f}$. If the energy and momentum of the scattered particle are given by $\epsilon(p)$ and $\boldsymbol{p}$, respectively, conservation law implies the following:

$$\frac{1}{2}M\boldsymbol{v}_\mathrm{i}^2 = \frac{1}{2}M\boldsymbol{v}_\mathrm{f}^2 + \epsilon(p), \tag{2.80}$$

$$M\boldsymbol{v}_\mathrm{i} = M\boldsymbol{v}_\mathrm{f} + \boldsymbol{p}. \tag{2.81}$$

Equation (2.81) is solved for $\boldsymbol{v}_\mathrm{f}$ and inserted into Eq. (2.80), which leads to:

$$\epsilon(p) - \boldsymbol{p}\,\boldsymbol{v}_\mathrm{i} + \frac{p^2}{2M} = 0. \tag{2.82}$$

The last term in the equation above will be negligible, if the mass M is large. Hence, the critical Landau velocity is given by:

$$\boldsymbol{v}_\mathrm{L} = \left[\frac{\epsilon(p)}{p}\right]_\mathrm{min}. \tag{2.83}$$

For a weakly interacting Bose gas as discussed in the previous section, the critical Landau velocity equals the sound velocity of the Bogoliubov dispersion for small momentum. Thus, a weakly interacting Bose gas at zero temperature is a superfluid. When the interactions are strong, the Landau criterion is still fulfilled with a critical velocity smaller than the sound velocity. In general, it is obvious that the critical velocity decreases as the interaction decreases and vanishes completely for an ideal gas without interaction and a free particle dispersion $\epsilon(p) = p^2/(2m)$. The criterion can also be deduced from a liquid moving in a small tube or capillary.

In addition to the Landau criterion, phase coherence and long range order are necessary for a superfluid, since all particles of a superfluid coherently participate within a superfluidity flow. Therefore, another connection between superfluidity and BEC, besides the critical Landau and sound velocity of the Bogoliubov excitation spectrum, is the coupling between the velocity of the superfluid $\boldsymbol{v}_s$ and the phase $\boldsymbol{S}$ of the BEC order-parameter Ψ_0. To derive this connection the Gross-Pitaevskii equation (2.67) has to be multiplied with $\Psi_0^*(\boldsymbol{r},t)$ and subtracted with the complex conjugate so that a continuity equation is obtained:

$$\frac{d}{dt}n(\boldsymbol{r},t) + \mathrm{div}\left[\boldsymbol{j}(\boldsymbol{r},t)\right] = 0, \tag{2.84}$$

where $\boldsymbol{j}(\boldsymbol{r},t)$ is the particle-current density and is given as

$$\boldsymbol{j}(\boldsymbol{r},t) = -\frac{i\hbar}{2m}\left(\Psi_0^*\nabla\Psi_0 - \Psi_0\nabla\Psi_0^*\right). \tag{2.85}$$

With the expression in Eq. (2.52) one obtains

$$\Psi_0(\boldsymbol{r},t) = \sqrt{n(\boldsymbol{r},t)}e^{iS(\boldsymbol{r},t)} \tag{2.86}$$

and the particle-current density can be rewritten as

$$\boldsymbol{j}(\boldsymbol{r},t) = n(\boldsymbol{r},t)\frac{\hbar}{m}\nabla S(\boldsymbol{r},t). \tag{2.87}$$

Hence, for the connection between BEC and superfluidity follows that the superfluidity velocity $\boldsymbol{v}_s$ is given as the product of the local particle density and the gradient of the phase S of the order parameter:

$$\boldsymbol{v}_s(\boldsymbol{r},t) = \frac{\hbar}{m}\nabla S(\boldsymbol{r},t). \tag{2.88}$$

Accordingly, for a nonzero field operator $\Psi(\boldsymbol{r},t)$ and a well-defined phase $S(\boldsymbol{r},t)$ it follows that

$$\nabla \times \boldsymbol{v}_s(\boldsymbol{r},t) = 0. \tag{2.89}$$

Thus, the integral of the superfluidity velocity $\boldsymbol{v}_s$ is zero, but for the appearance of singularities with the consequence that $\Psi(\boldsymbol{r},t)$ vanishes. The change in the phase $\triangle S(\boldsymbol{r},t)$ has to be an integer multiple of 2π

$$\triangle S(\boldsymbol{r},t) = \oint \nabla S(\boldsymbol{r},t)dl = 2\pi l \qquad l = ...-2,-1,0,1,2... \tag{2.90}$$

due to the fact that the phase itself is defined modulo 2π. This leads to a quantized circulation

$$\Gamma = \oint \boldsymbol{v}_s dl = l\frac{h}{m} \tag{2.91}$$

called Onsager-Feynman quantization condition and results in the occurrence of quantized vortices.

2.2.4 BEC in a 2D System

If in the thermodynamic limit the dimension of a system is reduced to 2D, the critical density (2.46) defined for the BEC phase-transition in a 3D system will diverge for $\mu \to 0$. This is due to the fact that the critical density depends on the density of states of a 2D system which has a nonzero value for E_0. As a consequence, no phase transition towards a BEC in the thermodynamic limit can occur. Only at $T = 0$ BEC exists. Since there is no macroscopic ground-state population, the appearance of long-range-order is not possible due to phase fluctuations. But these phase fluctuations do not destroy any superfluidity and, therefore, a new phase transition has been declared by Kosterlitz and Thouless. Above a critical temperature T_{KT} the density of the superfluid n_{s} is zero and there is only local condensation. These local condensates are completely decoupled from each other because free thermally excited vortices prevent the flow of the local condensates until the critical temperature is reached. At this point, the free

vortices become unstable and form pairs and clusters with a total binding number equal to zero. This allows the flow of the local condensates where phase coherence exists. Hence, there is a sudden jump in the superfluid density n_s to a nonzero value and a global superfluid is formed. The critical temperature is given by [63]

$$k_\mathrm{B}T_\mathrm{KT} = \frac{\pi\hbar^2 n_\mathrm{s}}{2m}. \tag{2.92}$$

To describe this transition in dependence of the thermal de Broglie wavelength at temperature T_KT the following relationship is used [64]:

$$n_\mathrm{s}\lambda^2_{\mathrm{dB}_\mathrm{KT}} = 4 \tag{2.93}$$

The formed superfluid can be described by the Bogoliubov theory for weakly interacting bosons, even though its wave function has a finite extension in reciprocal space and true long-range-order can only be achieved when no vortices exist, such as for $T = 0$.

Nevertheless, it is also possible to achieve a BEC transition at finite temperatures in a 2D system by confining the Bose gas in a spatially varying potential $U \sim r^\eta$. This leads to a density of states $\rho(E) \sim E^{2\eta}$ with the consequence that Eq. (2.46) converges for $\eta > 0$. Hence, it is possible to define a critical temperature for the phase transition again [65]:

$$k_\mathrm{B}T_\mathrm{c} \sim \left(\frac{n}{m}\right)^{\eta/(2+\eta)}. \tag{2.94}$$

Therefore, it is only necessary to have discrete energy levels E_i $(i = 1, 2, ..)$ and a finite total particle number arising from the finite size L^2 to achieve a critical density definition for a 2D system:

$$\mu = E_1, \tag{2.95}$$

$$n_\mathrm{c} = \frac{1}{L^2}\sum_{i\geq 2}\frac{1}{e^{E_i/(k_\mathrm{B}T)} - 1}. \tag{2.96}$$

By use of the expression of the thermal de Broglie wavelength, for the 2D critical density follows:

$$n_\mathrm{c} = \frac{2}{\lambda^2_\mathrm{dB}}\ln\left(\frac{L}{\lambda_\mathrm{dB}}\right). \tag{2.97}$$

To conclude, in the thermodynamic limit BEC is absent in a two-dimensional system, whereas in a finite system BEC phase-transition occurs. Superfluidity in a 2D system can be achieved below the Kosterlitz and Thouless transition temperature. In the last few years several condensation signatures were verified for polaritons in microcavity systems. In 2006, Kasprzak et al. presented results showing macroscopic occupation of the ground state and a nonlinear threshold behavior

[17]. Spatial coherence and ODLRO for polariton condensates were illustrated in the publication of Deng et al. in 2007 [66]. Demonstrations of Bogoliubov excitations [67], quantized vortices [68], half vortices [69] and spontaneous polarization [70] followed. Furthermore it was possible to show superfluid behavior [71, 72]. The expected coherence build-up was confirmed by results of correlation measurements [73].

2.2.5 BEC under Nonresonant Excitation

In the case of a planar microcavity with embedded QWs the possibility of nonresonant excitation has to be considered as well. Under this configuration the BEC strongly depends on the geometry of the pump spot, since the influence of the exciton reservoir cannot be neglected anymore. The derivations in this section follow the publication of Wouters et al. [57].

To explain the occurring phenomena under nonresonant pumping a mean-field approach can be used. The generalized nonequilibrium Gross-Pitaevskii equation (GPE) describes the dynamics of the macroscopic condensate with the wave function $\Psi(\boldsymbol{r})$.

$$i\hbar\frac{\partial\Psi(\boldsymbol{r})}{\partial t} = \left\{E_0 - \frac{\hbar^2}{2m}\nabla^2_{\boldsymbol{r}} + \frac{i\hbar}{2}[R[n_{\mathrm{R}}(\boldsymbol{r})] - \gamma_{\mathrm{con}}] + V_{\mathrm{ext}}(\boldsymbol{r}) + \hbar g|\Psi(\boldsymbol{r})|^2 + V_{\mathrm{R}}(\boldsymbol{r})\right\}\Psi(\boldsymbol{r}). \tag{2.98}$$

E_0 represents the ground-state energy of the LP and m is its effective mass. V_{ext} stands for an external potential such as disorder in the excitonic and photonic structure [74]. g describes the repulsive Coulomb-interaction strength between two condensate polaritons and γ_{con} is the linear polaritonic cavity-loss rate. $R[n_{\mathrm{R}}(\boldsymbol{r})]$ represents the condensate gain rate and can be described by a monotonically growing function of the local density $n_{\mathrm{R}}(\boldsymbol{r})$ of the noncondensed reservoir polaritons. Caused by the reservoir a mean-field repulsive potential $V_{\mathrm{R}}(\boldsymbol{r})$ occurs and can be approximated by

$$V_{\mathrm{R}}(\boldsymbol{r}) \simeq \hbar g_{\mathrm{R}} n_{\mathrm{R}}(\boldsymbol{r}) + \hbar\mathcal{G}P(\boldsymbol{r}). \tag{2.99}$$

Here, $P(\boldsymbol{r})$ is the pumping rate and g_{R} and $\mathcal{G}$ are interaction strengths induced by condensate polariton scattering with reservoir polaritons and free carriers. When the GPE is now coupled to a rate equation of the reservoir population, it follows:

$$\dot{n}_{\mathrm{R}}(\boldsymbol{r}) = P(\boldsymbol{r}) - \gamma_{\mathrm{R}} n_{\mathrm{R}}(\boldsymbol{r}) - R[n_{\mathrm{R}}(\boldsymbol{r})]|\Psi(\boldsymbol{r})|^2. \tag{2.100}$$

Therefore, polaritons reach the reservoir with a rate $P(\boldsymbol{r})$ and relax with an effective rate $\gamma_{\mathrm{R}} \gg \gamma_{\mathrm{con}}$. This large effective decay rate is due to the thermalization of bottleneck polaritons with a bath of hot carriers created by the pump beam. Final state-stimulated scattering into the condensate mode causes a depletion of the reservoir density which is proportional to $R[n_R(\boldsymbol{r})]|\Psi(\boldsymbol{r})|^2$.

In the following, the spatially homogeneous case of the pump spot geometry $P(\boldsymbol{r}) = P$ will be considered so that in absence of an external potential analytically stationary solutions are found for Eqs. (2.98) and (2.100). One obtains for the condensate density $|\Psi(\boldsymbol{r})|^2 = 0$ below the condensation threshold, thus, the reservoir density grows linearly with the excitation intensity $n_\mathrm{R}(\boldsymbol{r}) = P/\gamma_\mathrm{R}$. When the threshold pump intensity P^th is reached, the stimulated scattering equals the losses $R[n_{\mathrm{R,th}}(\boldsymbol{r})] = \gamma_\mathrm{con}$, while the solution with $|\Psi(\boldsymbol{r})|^2 = 0$ becomes unstable. With further increasing excitation power and therefore well-above the threshold, the reservoir density becomes homogeneous $n_\mathrm{R}(\boldsymbol{r}) = n_\mathrm{R}$. The condensate wave function has now the form $\Psi(\boldsymbol{r}) = e^{i(\boldsymbol{k}_\mathrm{con}\boldsymbol{r}-\omega_\mathrm{con}t)}\Psi_0$, and it leads to a condensate-density dependence of $|\Psi_0|^2 = (P - P^\mathrm{th})/\gamma_\mathrm{con}$. $\boldsymbol{k}_\mathrm{con}$ is the condensate wave vector and, even though it is still undetermined, stable solutions exist. Corresponding to each value of $\boldsymbol{k}_\mathrm{con}$, the given oscillation frequency ω_con reads

$$\omega_\mathrm{con} - \omega_0 = \frac{\hbar^2\boldsymbol{k}_\mathrm{con}^2}{2m} + g|\Psi_0|^2 + g_\mathrm{R}n_\mathrm{R} + \mathcal{G}P. \tag{2.101}$$

In the case of a heterogeneous pump profile $P(\boldsymbol{r})$ one has to define a local density $\rho(\boldsymbol{r})$ and a local phase $\phi(\boldsymbol{r})$ instead of a global definition. Thus, stationary solutions have the following form:

$$\Psi(\boldsymbol{r},t) = \Psi_0(\boldsymbol{r})e^{i\omega_\mathrm{con}t} = \sqrt{\rho(\boldsymbol{r})}e^{i[\phi(\boldsymbol{r})-\omega_\mathrm{con}t]}, \tag{2.102}$$

$$n_\mathrm{R}(\boldsymbol{r},t) = n_\mathrm{R}(\boldsymbol{r}). \tag{2.103}$$

While the condensate oscillation frequency stays the same throughout the spot, its local wave vector varies and is determined as the spatial gradient of the phase:

$$\boldsymbol{k}_\mathrm{con} = \nabla_{\boldsymbol{r}}\phi(\boldsymbol{r}). \tag{2.104}$$

By use of Eqs. (2.102) and (2.103), the generalized GPE and the rate equation lead to:

$$\hbar\omega_\mathrm{con} = \hbar\omega_0 + \frac{\hbar^2\boldsymbol{k}_\mathrm{con}^2}{2m} + V_\mathrm{ext} + \frac{\hbar^2}{2m}\frac{\nabla_{\boldsymbol{r}}^2\sqrt{\rho}}{\sqrt{\rho}} + \hbar g\rho + \hbar g_\mathrm{R}n_\mathrm{R} + \hbar\mathcal{G}P, \tag{2.105}$$

$$0 = [R[n_\mathrm{R}] - \gamma_\mathrm{con}]\rho - \frac{\hbar}{m}\nabla_{\boldsymbol{r}}\rho\boldsymbol{k}_\mathrm{con}, \tag{2.106}$$

$$P = \gamma_\mathrm{R}n_\mathrm{R} + R[n_\mathrm{R}]\rho. \tag{2.107}$$

Under the condition that the variation of the pump profile is sufficiently plain, a local density approximation (LDA) can be used. As a consequence, the quantum-pressure term in Eq. (2.105) and the term of the current divergence in (2.106) are negligible. Hence, under the LDA the condensate is treated as homogeneous system with a local value of the intensity of the pump spot $P(\boldsymbol{r})$. Therefore, below threshold $P(\boldsymbol{r}) < P^\mathrm{th}$ the condensate-density profile vanishes $\rho(\boldsymbol{r}) = 0$ for all points $\boldsymbol{r}$. Since the condensate oscillation frequency ω_con is constant, this variation has to be balanced by a variation in the wave vector in space $\boldsymbol{k}_\mathrm{con} = \boldsymbol{k}_\mathrm{con}(\boldsymbol{r})$.

It is possible for a symmetric pump profile to elaborate an analytic solution if there is no external potential such as disorder. Under this circumstance the stationary solutions are cylindrically symmetric and the condensate wave vector vanishes at the center of the spot $\boldsymbol{k}_{\mathrm{con}}(r=0)=0$. Accordingly, it leads to

$$\omega_{\mathrm{con}}-\omega_0 = g\rho(r=0)+g_{\mathrm{R}}n_{\mathrm{R}}(r=0)+\mathcal{G}P(r=0). \tag{2.108}$$

In case of an experimental conventional Gaussian pump spot the intensity decreases along the radial direction and the condensate wave vector points in this direction and increases with r. At the point where $P(r)$ reaches the threshold value P^{th}, the wave vector value is at its maximum. If so, the repulsive interactions lead to an anti-trapping potential V_{at} giving rise to a ballistical acceleration of polaritons away from the center of the spot:

$$V_{\mathrm{at}}(r) = \hbar g\rho(r)+\hbar g_{\mathrm{R}}n_{\mathrm{R}}(r)+\hbar\mathcal{G}P(r). \tag{2.109}$$

Having a closer look at the different sizes of a Gaussian excitation spot, one notices a quite huge influence of the size onto the dynamics of the condensate. In the following, a spot with a waist of about $\sigma_{\mathrm{p}}=20\ \mu$m is compared to one with $\sigma_{\mathrm{p}}\approx 2\ \mu$m. For the calculations shown in Fig. 2-7 a parabolic polariton dispersion was assumed.

Large Gaussian Pump spot

In the case of a large Gaussian pump spot a significant broadening of the polariton distribution in real-space due to the anti-trapping potential is noticeable, as shown in panel (c) of Fig. 2-7. Panel (d) shows that as soon as the spatial polariton density vanishes, the local condensate wave vector saturates. In consequence of the steep behavior of the local condensate wave vector next to the center of the pumping spot, there is a quite wide polariton distribution in momentum-space which is centered around $k_{||}=0$. The highest wave vector value k_{c0} which can be reached is the one where the free polariton dispersion equals the condensate frequency $\omega_{\mathrm{con}}(k_{\mathrm{c0}})=\omega_{\mathrm{LP}}$. All in all, these results are able to explain the occurring flat condensate behavior shown in panel (a). Due to the Gaussian shaped pump spot the polariton density in real- and momentum-space is higher at the center of the spot than at the side. This leads to a higher blueshift at the center and with a constant condensate frequency and a parabolic free polariton dispersion it results in a flat condensate mode.

Small Gaussian Pump Spot

There is a change in the behavior as soon as the excitation spot gets smaller than the ballistic propagation distance of the polaritons. In this case the polaritons are able to travel away from the pump spot before decaying. As a result of this

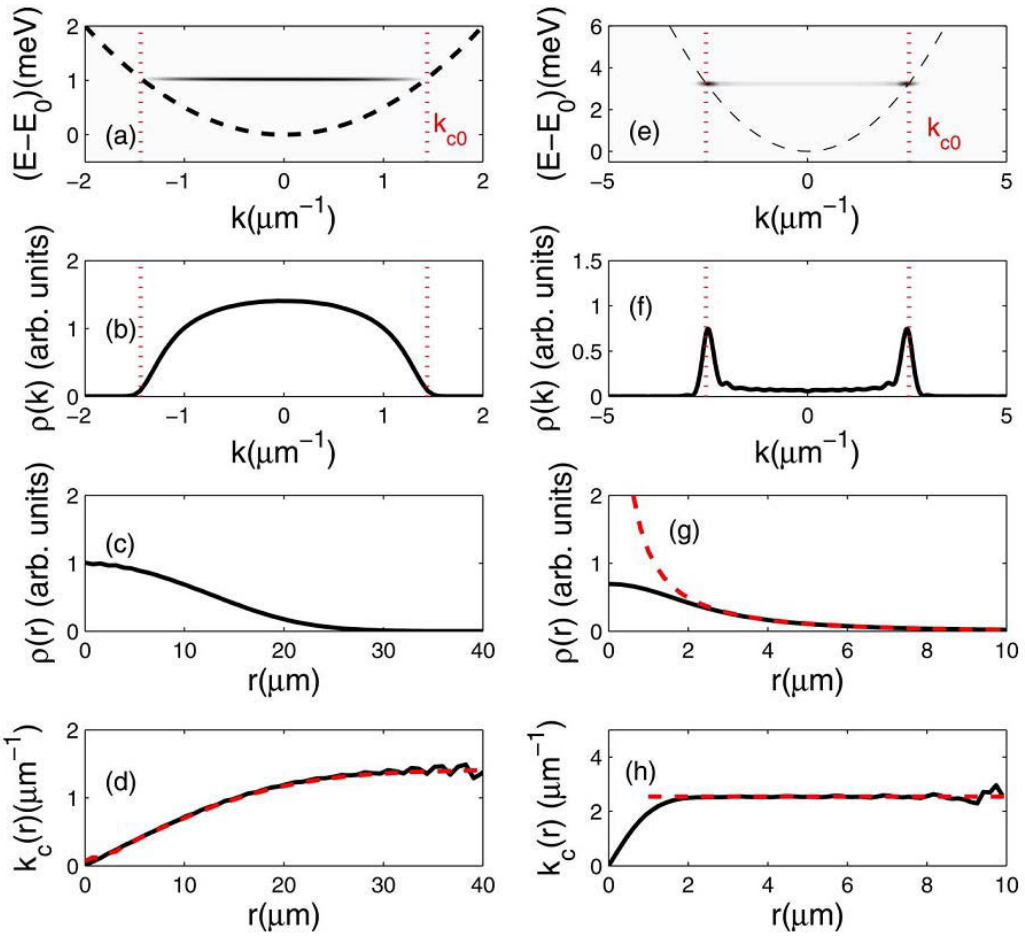

Figure 2-7: Numerical results of generalized GPE simulations for a small and large pumping spot performed by Wouters et al. in 2008 [57]. On the left side, (a)-(d), results for a spot with $\sigma_p = 20$ μm are shown, and on the right side, (e)-(h), results for a pump spot with $\sigma_p = 2$ μm are presented. The panels on top (a) and (e) give the polariton condensate dispersion under nonresonant excitation. The dashed black line represents the free polariton dispersion with the corresponding wave vector k_{c0} at ω_{con} indicated by the red dotted line, also seen in (b) and (f). The panels below (b) and (f) show the polariton distribution in momentum space and panels (c) and (g) the one in real space. The red dashed line in (g) is the analytical approximation to the density tail, since LDA cannot be performed for a small excitation spot but for regions far outside the pump spot. The lowest panels (d) and (h) present the local condensate wave vector $k_{con}(\boldsymbol{r})$. The dashed red lines here are LDA predictions of the local condensate wave vector. As can be seen for the large spot, the accordance with the numerical results is quite good. The figure is taken from reference [57].

geometry, the local density approximation can no longer be performed, but, under the assumption of no polariton interactions an analytical solution for the condensate wave function far from the pump spot is possible. As can be seen in the plots on the right side of Fig. 2-7, there is also a broadening visible in real-space (g) and a steep behavior of the condensate wave vector around the center of the pump spot (h). Beyond the pump spot the condensate wave vector saturates immediately, which is different to the behavior for a large excitation spot, where k_{con}

saturates with the disappearance of the polariton density. In momentum-space (f), the small spot leads to a ballistic expanding of the polaritons towards k_{c0}. Thus, the emission has a ring shape with a radius k_{c0}. Experimentally, this behavior was already observed by Richard et al. in 2005 [75]. Inside of the ring a weak emission intensity is noticeable, whereas beyond the ring almost no emission is present. In the dispersion diagram (e) the ring shape gets visible through two emission peaks occurring where ω_{LP} equals $\omega_{con}(k_{c0})$.

Chapter 3

Experimental Methods

This chapter contains basic explanations of the utilized experimental methods to perform exciton-polariton condensation measurements at low temperatures. In the first section of this chapter the investigated sample is described. This is followed by a section which presents the method of momentum- and spatially-resolved spectroscopy. The third section describes a basic micro-photoluminescence (μPL) setup to study the energy- and time-depending properties of the polariton condensate. For the results presented in Chap. 5 and 6 the basic μPL setup is extended in different ways. These changes are discussed in detail in the last two sections of this chapter.

3.1 Sample

For all results presented in this thesis the same sample was used, which will be described in the following paragraph.

The sample is a planar microcavity consisting of III-V semiconductor material and was grown by molecular-beam epitaxy (MBE) in the group of Prof. Alfred Forchel at the Julius-Maximilians-Universität in Würzburg. The Bragg mirrors enclose a $\lambda/2$-resonator with 20 layer pairs underneath and 16 on top of the cavity. The pairs are an alternating bedding of AlAs and $Ga_{0.8}Al_{0.2}As$ layers. With this mirror configuration a quality factor of about 1800 can be achieved. The resonator itself has 12 quantum wells (QWs) embedded with AlAs barriers as separators. To increase the coupling between the excitons of the QWs and the photons of the cavity, the QWs are embedded at the three central antinodes of the cavity with four wells at each maximum. The cavity itself is slightly wedged. This makes it possible to change the detuning between the pure photon and exciton mode by simply varying the position of excitation on the sample. The microcavity structure itself is grown in a GaAs substrate. A schematic drawing of the whole sample pattern is shown in Fig. 3-1.

With the high number of QWs the strong coupling regime can be stabilized.

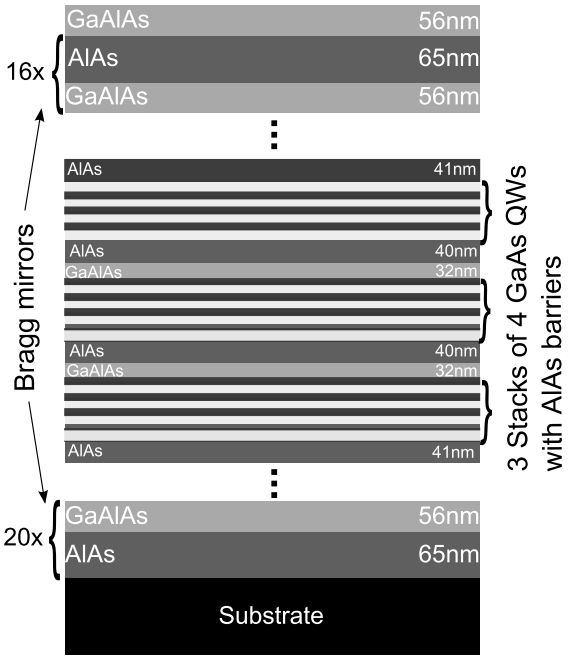

Figure 3-1: Schematic drawing of the planar microcavity examined in the measurements performed for this thesis. It consists of AlAs/GaAlAs Bragg mirrors which enclose a $\lambda/2$ cavity with alternating layers on top and underneath the cavity. 3 stacks of 4 QWs are embedded at the three central antinodes of the cavity. The sample was grown on a GaAs substrate using molecular-beam epitaxy.

The polariton wave function is delocalized over the whole microcavity and for a certain polariton density the exciton density decreases with increasing number of QWs. Therefore, one can reach a higher polariton density before an occurrence of a transition into the weak coupling regime caused by exciton bleaching. Additionally, the normal mode splitting (NMS) increases from about 4 meV for one QW in a planar GaAs microcavity to about 14 meV for 12 QWs (see Fig. 3-2) due to the fact that the coupling strength $g(k)$ is proportional to the square root of the number N of QWs [76].

3.2 Momentum- and Real-Space Imaging

The µPL spectroscopy offers the possibility to study the dispersion and time-dependence of the cavity emission. The following section starts with an explanation of the relation between the in-plane wave vector $k_{||}$ and the emission angle Θ. Afterwards the method of Fourier- and real-space imaging is described.

As already mentioned in section 2.1.2, the emission angle Θ from the cavity is directly related to the in-plane wave vector $k_{||}$ of the photons inside of the

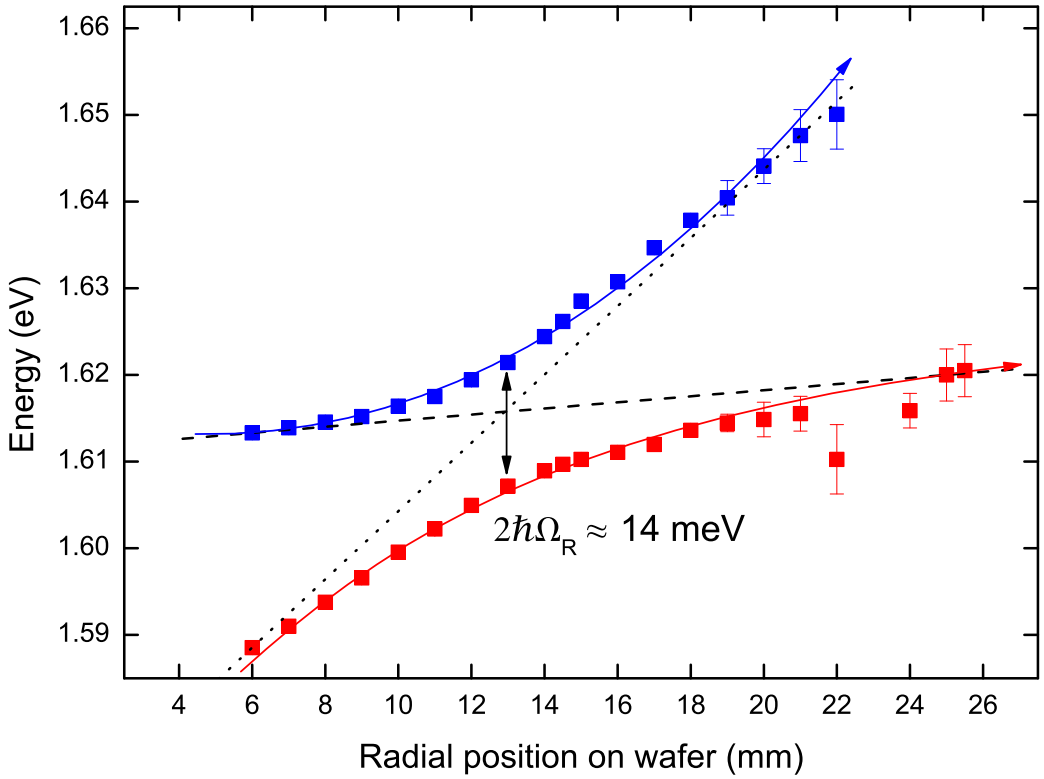

Figure 3-2: Energy of the lower (red squares) and upper (blue squares) polariton as well as for the uncoupled cavity (dotted line) and exciton (dashed line) mode in dependence of the radial position on the sample wafer. The arrow illustrates the normal mode splitting of $2\hbar g(0) = 2\hbar\Omega_R \approx 14$ meV. The data set results from reflectivity measurements performed by the group of Prof. Alfred Forchel at the Julius-Maximilians-Universität in Würzburg.

microcavity. When a photon is leaving the resonator, it leads to the decay of the polariton. And due to in-plane translation invariance in the cavity, the in-plane component of the polariton is equivalent to that of the emitted photon. Given that the energy has to be conserved when the photon leaves the microcavity, the energy of the photon equals that of the polariton. Therefore, it is possible to extract the full information by performing angle-resolved μPL measurements of the emitted photons following the relation:

$$k_{||} = k \sin\Theta = \frac{2\pi}{\lambda} \sin\Theta = \frac{E_{\mathrm{ph}}}{\hbar c} \sin\Theta. \tag{3.1}$$

The emission from the microcavity is collected by a microscope objective whose focal plane corresponds to a virtual plane - the Fourier plane. Each position on this plane represents a certain emission angle Θ_i and due to Eq. 3.1 also a certain in-plane wave vector $k_{||}$. Fig. 3-3 illustrates the concept of the Fourier plane schematically for two different angles.

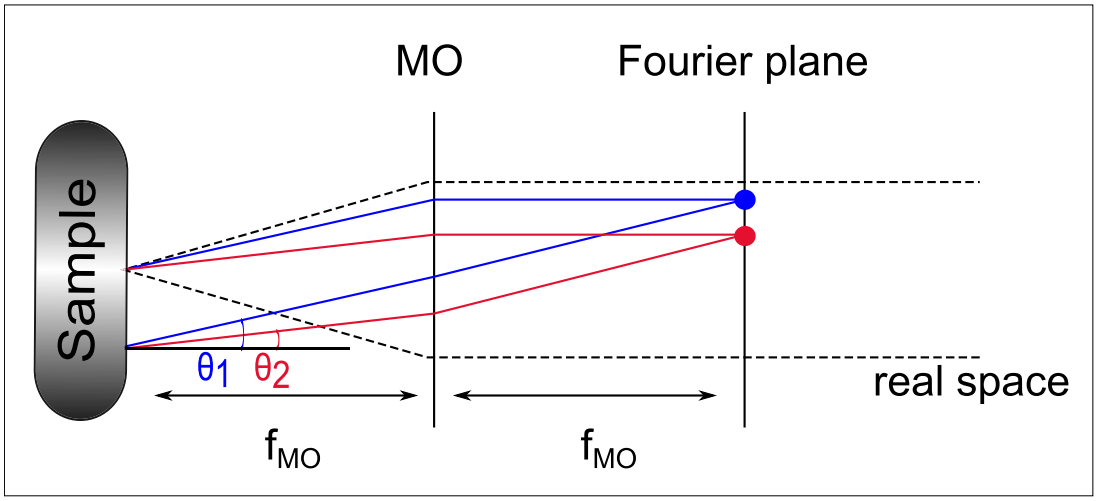

Figure 3-3: Illustration of the functionality of angle-resolved measurements. The light which leaves the sample under the same angle Θ will be collected at one point in the Fourier plane. To collect the light a microscope objective (MO) with the focal length f_{MO} is used. Imaging this Fourier plane onto the entrance slit of a spectrometer allows for dispersion measurements.

Performing spectrally-resolved measurements to investigate the dispersion of the emission the Fourier plane has to be imaged onto the entrance slit of a monochromator. This is realized by two lenses. For time-resolved measurements in momentum-space the Fourier plane is imaged with two lenses onto the entrance slit of a streak camera. If the distribution in real-space instead of momentum-space is of concern, the emission collected by the MO will be imaged onto the entrance slit of a monochromator or the streak camera by means of only one lens.

3.3 Basic Optical Setup

In this section the basic optical setup for the performed measurements is described. At first, the laser systems used for excitation and their characteristics are explained. Afterwards, the sample excitation technique is specified and in the last part of this section the detection methods are illustrated. Fig. 3-4 presents the scheme of the complete basic setup.

For optical excitation of the sample two different laser systems are available. On the one hand, a pulsed Ti:Sapphire laser (Coherent Mira 900) and, on the other hand, a continuous-wave (CW) Ti:Sapphire laser (Spectra Physics 3900). The pulsed Ti:Sapphire laser (Mira) emits pulses with a duration of either 1.5 ps or 100 fs at a repetition rate of 75.39 MHz and is pumped by a Nd:YVO_4 CW laser with 10 W. While the pump laser (Verdi V10) has a precise wavelength of 532 nm, the Mira can be tuned in a range of 700 to 980 nm. For time-resolved measurements with the streak camera a trigger signal is needed and, therefore, a small fraction of the laser emission is detected by a fast photo diode. The CW

Ti:Sapphire laser is also pumped by a Nd:YVO_4 CW laser (Sprout G10) which has an output power of 10 W at a wavelength of 532 nm. The CW laser has two sets of optics which allow an operation in a range of $700 - 850$ nm and $850 - 1000$ nm.

For compensation of the beam divergence for either the pulsed or CW laser, two lenses (L1 and L2) are used as a telescope. This optical arrangement has the advantage that the beam diameter can also be adapted depending on the requirement of the experiments. Two variable neutral density filters (NDF) are used to control the excitation power. To minimize the spatial displacement of the emission beam caused by varying one of the filters they are oriented in the opposite direction to each other and as close as possible to the sample in the cryostat. To polarize the excitation beam, a Glan-Taylor prism (GTP) is used and with $\lambda/2$ and $\lambda/4$ waveplates it is possible to switch between linear-, circular- and elliptical-polarized excitation. Finally, there are two possibilities of focusing the excitation beam onto the sample. On the one hand, a lens (L3) is used when the excitation takes place under an angle of 45° from normal incidence. On the other hand, for excitation from normal incidence the combination of a beam splitter and a microscope objective (MO) is used. With a $f = 60$ mm-lens, the spot size is in the order of $20 - 30$ µm, and in the case of excitation with the MO it is in the range of a few micrometers. The sample is mounted on a cold finger inside of a helium-flow cryostat (Cryovac Konti-Cryostat Micro). By controlling the flow of the helium through the cryostat and in addition with external heating it is possible to accomplish measurements at temperatures between 6 and 300 K. To vary the excitation spot on the sample, the cryostat is mounted on three micrometer-screw operated translation stages. This makes it possible to perform measurements at different detunings of the photon and exciton mode.

The PL of the sample is either collected by a microscope objective with a numerical aperture of 0.26 and a magnification factor of 10 or by an objective with a numerical aperture of 0.42 and a magnification by a factor of 50.

Spectrally Resolved Measurements

The lenses (L4 and L5) are used to image the Fourier plane onto the slit of a monochromator for spectrally-resolved measurements. The monochromator (Acton SP-2500i) has a focal length of 500 mm and offers a triple grating turret. The gratings with 300 and 1200 grooves per millimeter are blazed at 1000 nm and the third grating, which has 600 grooves per millimeter, is blazed at 500 nm. The blaze wavelength is the wavelength at which the grating reaches its maximum efficiency. After passing the spectrometer the PL is detected by a charged-coupled-device (CCD) camera which is mounted on the monochromator exit port. The CCD camera is a camera cooled by liquid nitrogen to minimize the influence of noise and dark counts on the signal. The CCD itself has 1340x400 pixels with a pixel size of 20 µm. Under these experimental conditions with an entrance slit width of 20 µm a spectral resolution of about 0.09 nm has been reached.

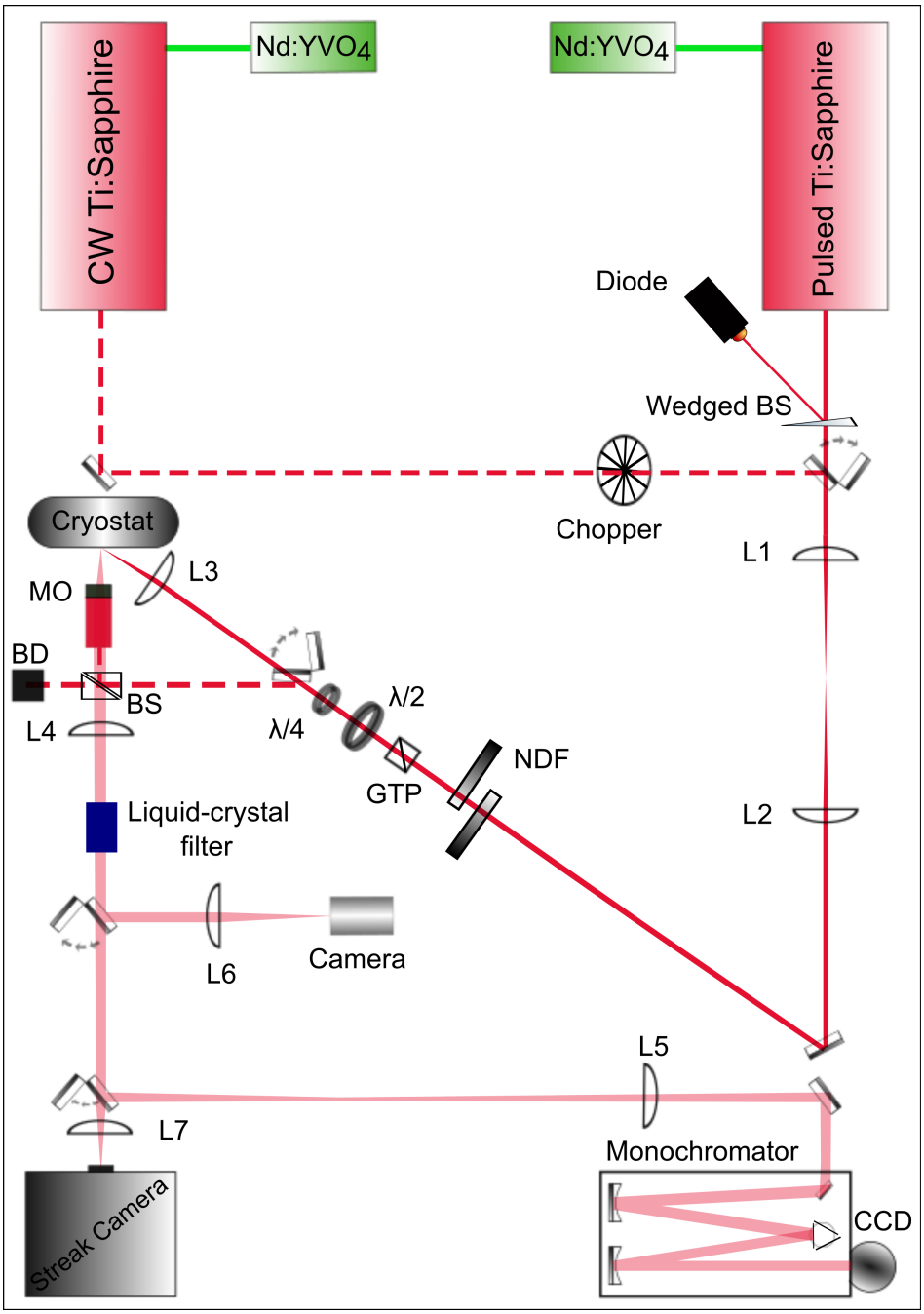

Figure 3-4: Scheme of the basic experimental μPL setup. As optical excitation source a CW or a pulsed Ti:Sapphire laser is used. Two lenses (L1 and L2) form a telescope to be able to get a certain beam diameter and to correct divergence of the original laser beam. Two neutral density filter (NDF) are placed into the excitation beam to control the excitation power. Furthermore, a Glan-Taylor prism (GTP), a $\lambda/2$ and $\lambda/4$ waveplate are placed into the beam. The beam itself can be focused under an angle onto the sample using a lens (L3) or from normal incidence by making use of a beam splitter (BS) and a microscope objective (MO). The same MO is used to collect the sample emission. The system of a flip mirror, lens (L6) and camera enables an intermediate image of the sample and spot on the sample. To image the Fourier plane onto the monochromator slit, lenses L4 and L5 are utilized. For real-space measurements only lens L5 is needed. A flip mirror in front of the streak camera enables to switch between time- and spectrally-resolved measurements. In front of the streak camera a short focal length lens (L7) focuses the signal onto the entrance slit.

Time Resolved Measurements

Time-resolved measurements are performed by using a streak camera. In this case, the emission is going through a liquid-crystal interference filter (VariSpec NIRR) to select a single-spectral emission mode. The filter has a spectral full-width-at-half-maximum (FWHM) of about 0.75 nm. The filter can be tuned via remote-control over a range of $650 - 1100$ nm. The signal is focused with a short-focal-lens (L7) onto the entrance slit of the streak camera. Inside of the streak camera the signal is subsequently guided to a photocathode. The incoming photons are then converted into photoelectrons scaling with the intensity. In the following, the free electrons get accelerated and pass two vertical sweep units, which are provided with a temporally oscillating electric field. The electrons therefore get deflected in a certain angle, which is proportional to their arrival time. Since the deflection voltage is synchronized with the repetition rate of the pulsed laser for each incoming pulse a new deflection loop is started. The electrons then pass a micro-channel-plate, where they are multiplied and hit a phosphor screen. The brightness of the phosphorescence is proportional to the intensity of the signal. A CCD camera is used to detect the signal where the horizontal position corresponds to the position in space and the vertical position to the arrival time.

3.4 Setup for Measurements with a Spatial-Light-Modulator

In order to perform measurements with differently shaped excitation spots and to change the shape easily, the basic μPL setup is extended by a spatial-light-modulator (SLM). A scheme of the extended setup is shown in Fig. 3-5.

A phase-only SLM (Holoeye Pluto VIS) with a display consisting of 1920x1080 pixels and a pixel pitch of 8 μm is used. The reflective liquid-crystal micro display can provide a phase shift above 2π in the whole visible range and can be addressed like an external monitor. For the purpose of creating an excitation beam with a certain spatial shape a diffractive optical element (DOE) as a 256-graylevel image has to be created so that the phase of the incoming laser beam is influenced when hitting the SLM. Therefore, the Fourier transform of the initial shape is calculated and optimized with an iterative Fourier-Transform Algorithm [77]. By means of this method a diffraction efficiency of slightly above 80% is achieved. To separate the diffracted beam from the undiffracted reflection a DOE phase pattern of a lens is superimposed onto the created DOE of the beam shape. Thus, the undiffracted reflections are blocked by an iris-diaphragm to avoid their leaving from the optical table. The desired beam shape instead is imaged in the focal plane of the virtual lens, since focusing is equivalent to performing a Fourier transform. To image the picture in the focal plane onto the sample a lens and a 50x MO with a numerical aperture of 0.42 are used. The emission of the sample is collected by the same MO. The further way of detection is the same as described in Sec. 3.3.

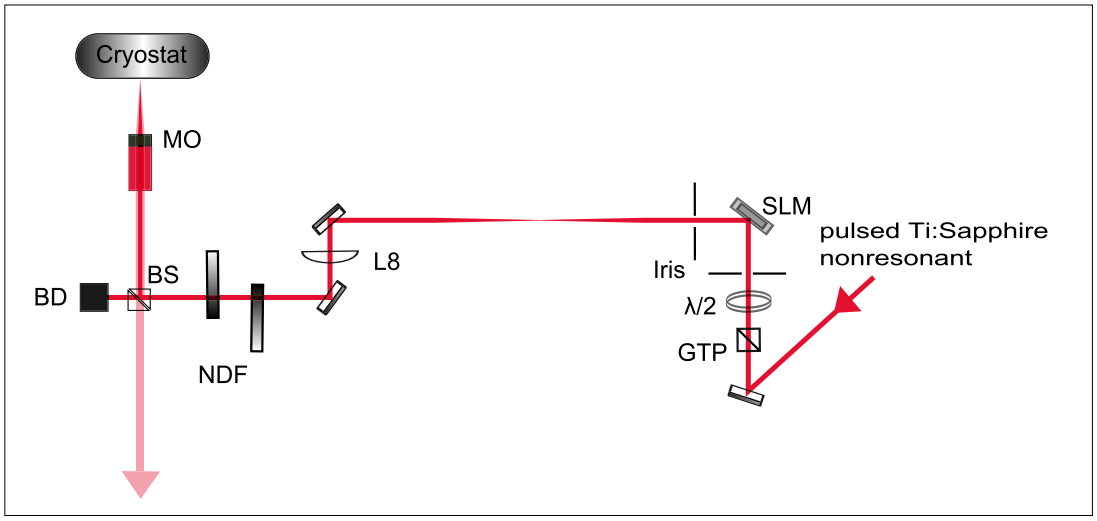

Figure 3-5: In addition to the basic μPL setup (Fig. 3-4) a spatial-light-modulator (SLM) is used in the excitation part of the setup. Since the beam hitting the SLM must have a certain polarization a Glan-Taylor prism (GTP) and a $\lambda/2$ waveplate are placed in front of the SLM. An iris-diaphragm is used to block the undiffracted reflections. The SLM can be controlled via extented monitor mode from the computer and its software is able to compute a diffractive optical element (DOE) of the desired spot shape to influence the phase of the laser beam. A DOE phase pattern of a lens is added to the beam shape pattern to separate the diffracted beam from the undiffracted reflections. This leads to an imaging of the desired beam shape in distance of the focal length of the virtual lens and makes it necessary to use a another lens (L8) and a microscope objective to finally image it onto the sample.

For the results presented in Chap. 4, measurements are performed with the SLM creating a wire-like excitation spot. On the surface of the sample, the projected wire has a length of 15 μm and a width of 2 μm. In Fig. 3-6 an image of the wire itself, of the created wire DOE phase pattern and an image of the wire DOE with an additional phase pattern of a lens is shown.

Also, a quasi-one-dimensional wire-staircase potential created by the SLM is studied. The staircase consists of 16 steps, and projected, onto the sample, each plateau of a step has a length of about 1 μm and a width of 2 μm. The right panels in Fig. 3-6 present the staircase pattern in real space, its DOE phase pattern and the combination of the staircase DOE with a lens phase pattern.

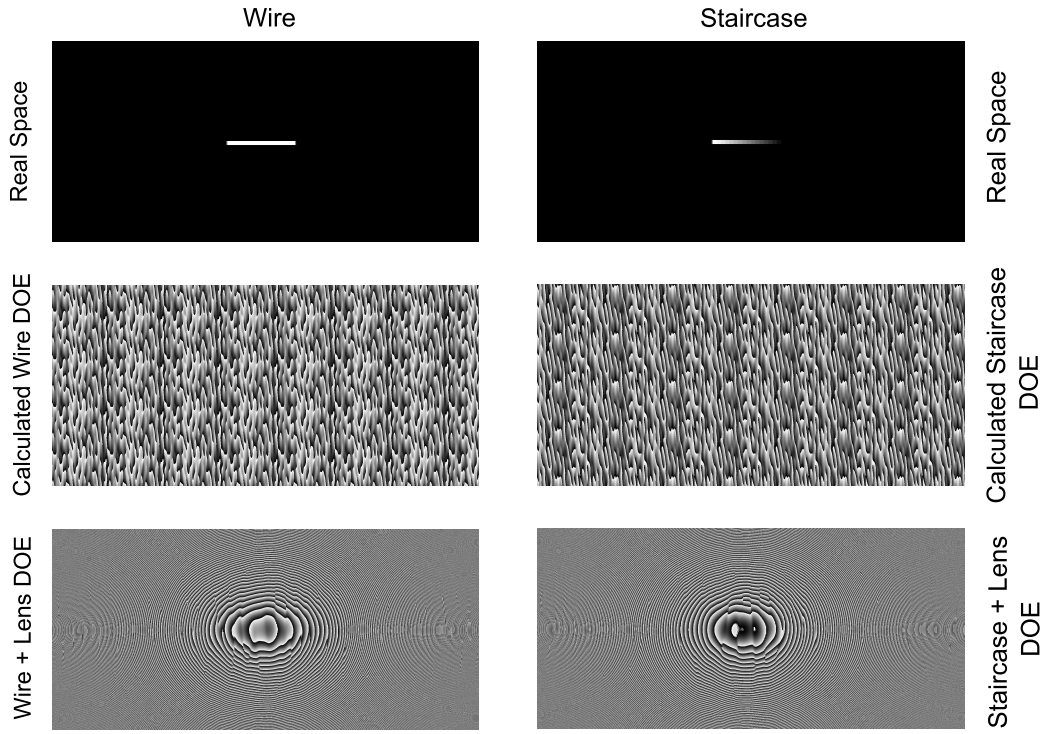

Figure 3-6: Top panels: The modeled-shape of the excitation spot, wire (left) and staircase (right). Middle panels: The optimized Fourier transform of the designated spot shape for both cases. Lower panel: The optimized Fourier transform, as shown in middle panels, additionally with the DOE of a lens.

3.5 Setup for Two-Laser Excitation Measurements

The results presented in Chap. 6 are obtained with the basic μPL setup extended by an additional excitation beam, as can be seen in Fig. 3-7. The sample is excited resonantly with a CW Ti:Sapphire laser under an angle of 45° from normal incidence. The excitation power is chosen in such a way that the regime of polariton lasing is achieved. A second nonresonant pulsed Ti:Sapphire laser is additionally focused onto the sample from the other side of the cryostat using a lens (L3b) with a focal length of $f = 150$ mm. The short nonresonant laser pulses (width ≈ 2 ps) are supposed to perturb the polariton condensate created by CW excitation. In the case of the resonant excitation, the spot diameter is approximately 20 μm, while the nonresonant probe laser has a spot diameter of about 10 μm and is located at the center of the resonant pump spot. A chopper is used to avoid damaging of the sample by simultaneously blocking both laser beams, which assures also that the sample is excited simultaneously by both beams. The PL of the sample is

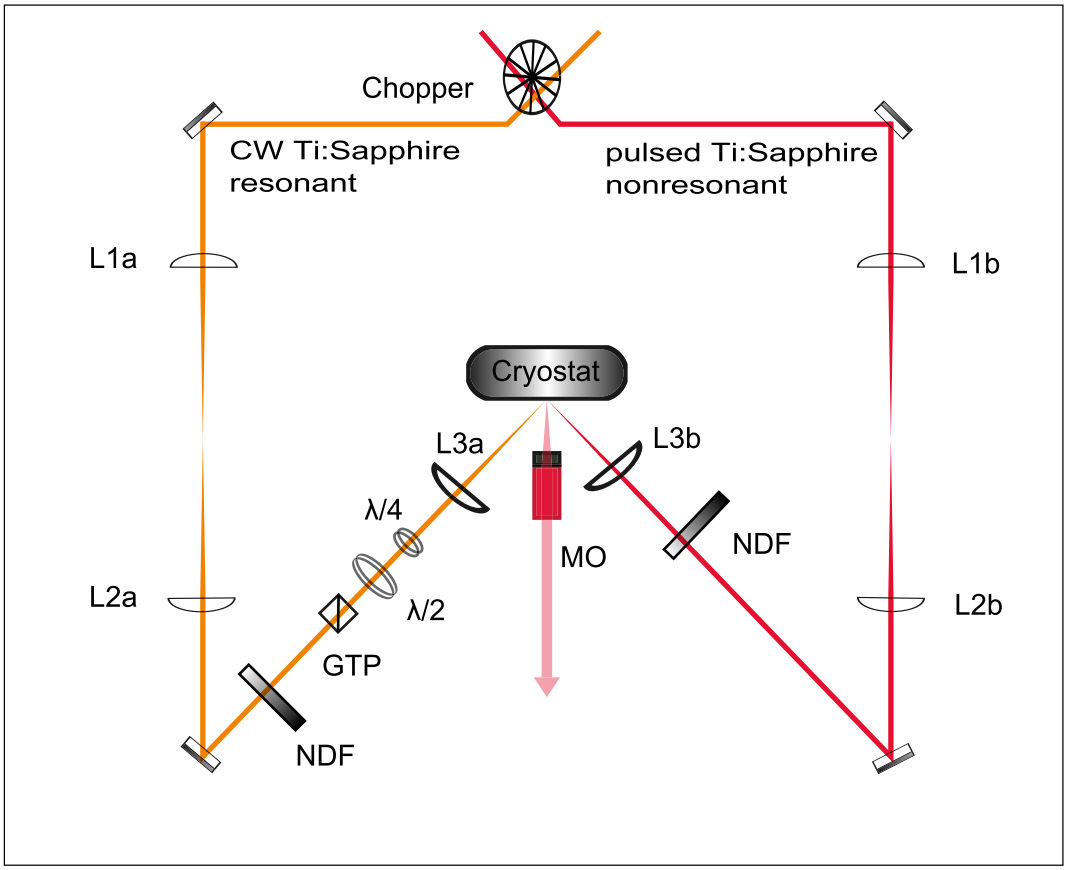

Figure 3-7: The basic μPL setup (Figure 3-4) is extended by an additional excitation beam. Left: Standard μPL-setup using the CW Ti:Sapphire (Spectra 3900) laser as a resonant excitation source to reach the regime of polariton condensation. Right: Additional nonresonant excitation with the pulsed Ti:Sapphire (Mira 900) laser to influence the polariton condensate through short laser pulses. The emission of the sample is collected by a 10x MO with a numerical aperture of 0.26.

collected by a 10x MO with an aperture of 0.26. Afterwards, it is detected by a streak camera in a way already described in section 3.3. The time-resolved results of these two-beam measurements are presented in Chap. 6.

Chapter 4

Relaxation Dynamics of Optically Imprinted Polariton Wires

The realization of polariton condensates in microcavity systems is a huge step towards optical circuits and all-optical switching. Due to their macroscopic wave function, condensed polaritons show collective phenomena and can be influenced by controlling their phase and velocity in an all-optical way [78]. Reports on multistability [79] or nonlocal spin switches [24] are pointing towards the realization of optical circuits.

Recently, it has become possible to achieve polariton condensation and to demonstrate its optical manipulation also in quantum wire microcavity systems [22]. In that context, phenomena such as bistability [80] are theoretically demonstrated and neuron-like switching [81] or polariton transistors [82] are already proposed. Thus, quantum wire microcavity systems are of considerable interest for all-optical circuits.

Compared to quantum wells, quantum wires are additionally confined in a lateral direction and are therefore one-dimensional systems. Due to the additional spatial confinement of the cavity, a splitting of the polariton mode into a fan of subbranches takes place [83]. Quantum wires of a certain width and length can be created from planar microcavities by lithography. The technique of quantum wire etching has the disadvantage of defining the confinement potential with the processing of the sample. This is not the case when a spatial-light-modulator (SLM) is used to optically imprint a certain potential and to localize the polaritons due to the effect of gain-trapping [84]. The polaritons are gain-trapped to the imprinted spot shape due to their short lifetime, which prevents them from moving far away before they decay. Therefore, this method offers the possibility to systematically study different confinement potentials.

This chapter presents an analysis of the relaxation dynamics in an optically created wire shaped potential for polaritons and is structured as follows. Firstly, the results of time-resolved measurements in real-space are presented including the study of spatially resolved intensity profiles at specific times in the decay

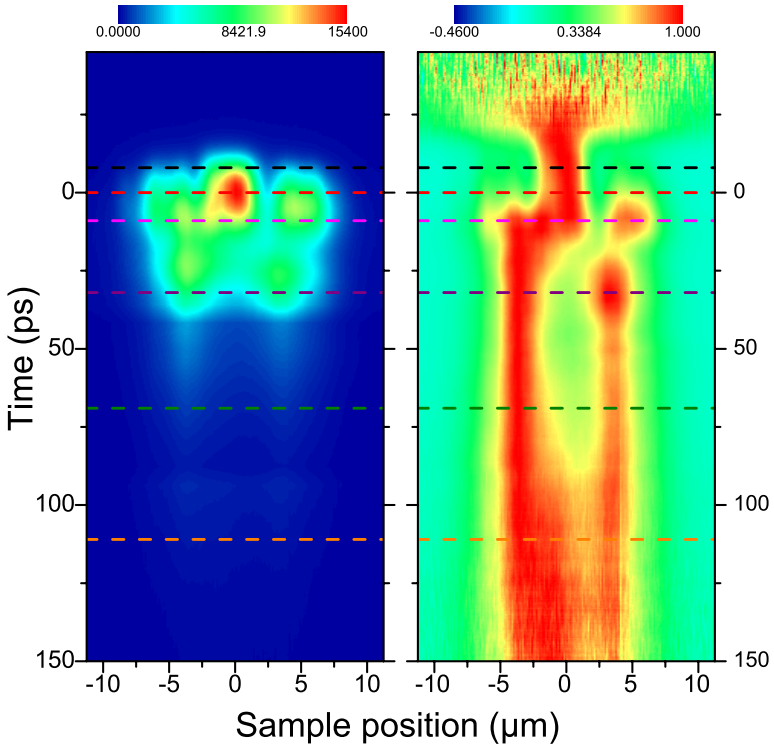

Figure 4-1: Spectrally integrated polariton decay dynamics confined in an optically created wire potential. (Left) Time dependence of the absolute emitted intensity spatially resolved. (Right) The emission intensity from the left panel normalized to the highest emission intensity at each respective time. The dashed lines represent the times which are of interest for further examinations. At early times the intense emission peak comes from the center of the wire. Two additional peaks occur at both sides of the wire after a few picoseconds. Later on, after about 30 ps these three peaks disappear and at the spatial position of the former intensity minima at both sides two new peaks arise. This shape of the pattern remains rather stable throughout the time.

dynamics. Secondly, spectrally resolved emission profiles at different times in the decay evolution are demonstrated.

4.1 Temporal and Spectral Dynamics of Optically Imprinted Quantum Wires

Time-resolved measurements in real-space provide information about the temporal and spatial dynamics of 1D confined polaritons. For this purpose, the microcavity sample (cf. Sec. 3.1) is excited nonresonantly with a beam shaped like a quantum wire by making use of a SLM. A detailed description of the optical setup can be found in Sec. 3.4. Figure 4-1 shows the emission of spectrally integrated polariton decay dynamics. The origin of the time axis (zero point) is defined by occurrence of the highest emitted intensity. The emission pattern consists of an

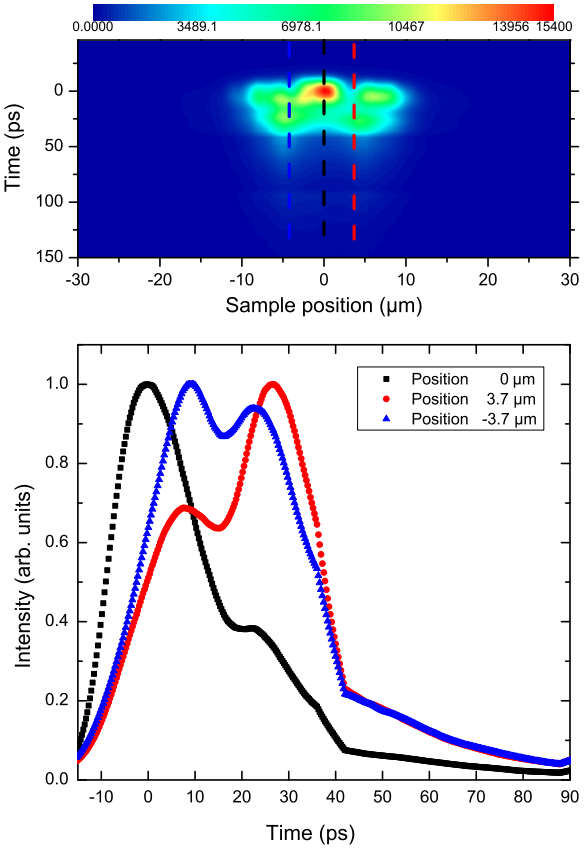

Figure 4-2: Intensity profiles for three different sample positions with time dependence. The positions are marked in the time-resolved emission pattern with dashed lines in the corresponding color. At the wire center the emission occurs with the impact of the pulse. Two side peaks appear after about 10 ps, followed by a short decrease and an increase at around 30 ps. The intensity profiles are normalized to the highest intensity value.

intense peak coming from the center of the wire defining the zero point on the spatial x-axis. The spatial width of the emission at that time is about $4-5$ µm. A few picoseconds later, two additional peaks occur at each side of the central peak with clear intensity minima between them. This three-peak behavior vanishes at around 25 ps and two peaks arise at ± 4 µm, slightly shifted compared to the previously mentioned side peaks. At later times, a smooth decrease of intensity takes place, while the spatial position of the emission stays unchanged. This stability in spatial position is also confirmed by the emission pattern with the absolute emitted intensity normalized to the highest intensity at each respective time, see right panel of Fig. 4-1. Moreover, at later times a spatial broadening of both emission peaks is observed.

Figure 4-2 shows the intensity profiles in dependence of time for three different sample positions to emphasize the results of the emission pattern shown in Fig. 4-1. The intensity profiles are normalized to the highest intensity of the respective position. The figure visualizes the earlier appearance of emission at the wire center compared to two positions at each side of the wire. After about 10 ps the side

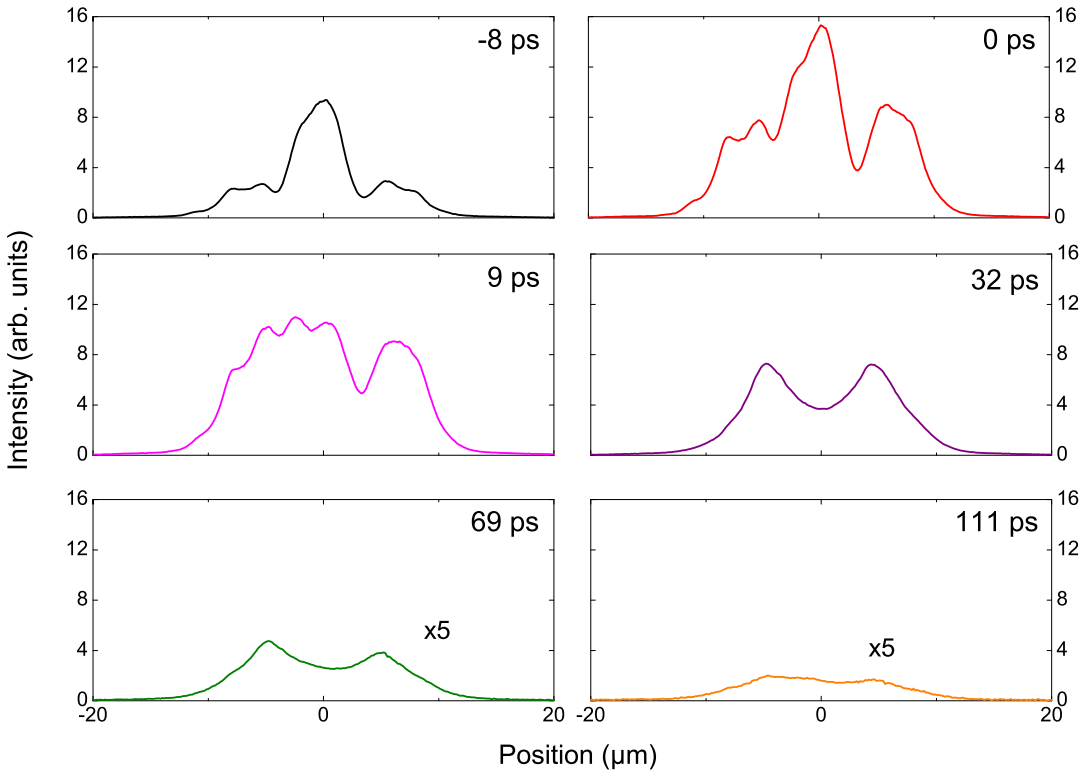

Figure 4-3: Spatially resolved intensity profiles at selected times throughout the emission pulse, as shown in Fig. 4-1. For a better visibility the profiles at 69 ps and 111 ps are multiplied by the factor five. The transition from the intense emission profile at the wire center with two side emission peaks towards a double peak behavior at later times is clearly demonstrated with the intensity profiles shown.

peaks occur followed by a slight intensity decrease and a further increase after about 30 ps. At this time the emission mainly stems from the side of the wire.

To illustrate the transition from a three-peak towards a double-peak behavior, Fig. 4-3 shows real-space intensity profiles at selected times which are indicated by dashed lines in Fig. 4-1 with the corresponding color. At early times the center emission is dominant and only small side peaks are visible. After about 9 ps all three peaks have about the same height. The center peak emission vanishes after around 32 ps and a clear double-peak behavior arises.

In order to fully characterize the dynamics of polaritons in optically created quantum wires, the spectral dynamics are also of interest. Therefore, spectrally resolved real-space emission profiles at selected times during the emission pulse are presented in Fig. 4-4. To allow for distinguishing between the strong and weak coupling regime, results of previous measurements are used [73]. For the present detuning the lower polariton energy is 1.6071 eV (771.5 nm) and the bare cavity mode has an energy of 1.6148 eV (767.8 nm). Due to nonresonant pumping, Coulomb interactions, caused by polariton-polariton and carrier-polariton interactions, play a significant role and lead to a blueshift in the polariton energy. With increasing blueshift the probability for screening effects increases.

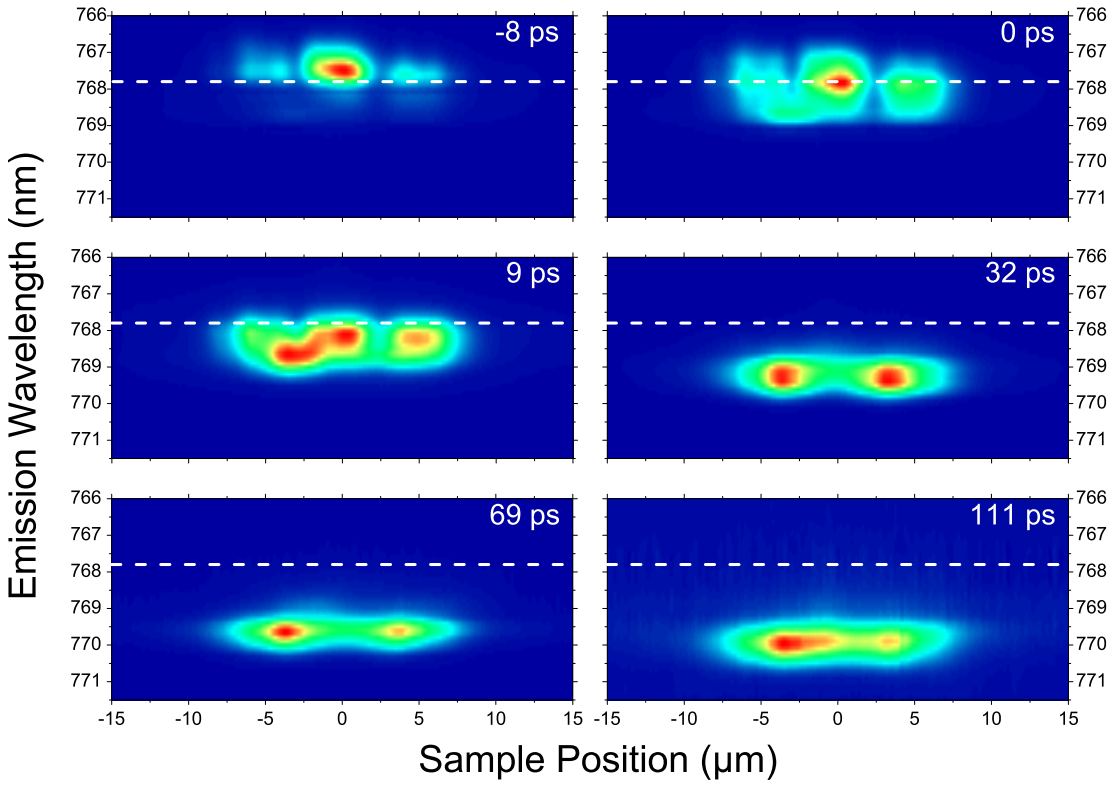

Figure 4-4: Real-space emission profiles spectrally resolved at selected times (compare Fig. 4-1) during the emission pulse. For early times the emission, mainly coming from the center of the wire, arises at wavelengths close to the bare cavity mode. With occurring of the double peak emission at later times a shift towards higher wavelengths is observable. The dashed white lines indicate the wavelength of the bare cavity mode.

These effects results in a breakdown of the strong coupling and a transition into the weak coupling regime with conventional photon lasing. In the case of this sample, the blueshift amounts to about 7.7 meV when the transition from strong to weak coupling takes place. Thus, it is clear that at early times the main emission from the wire center occurs at an energy being close to the bare cavity mode. Hence, the strong coupling is broken and the system is in the weak coupling regime. This is the case for times up to 9 ps, even though at this time a slight shift towards lower energies is visible. The two side peaks arising at that time, as can also be seen in Fig. 4-3, show blueshifts of about 5.9 meV. This is well below the mentioned transition blueshift. The wire center, where the emission of the weak coupling came from at earlier times, shows no strong emission peak anymore. With time passing by, the blueshift decreases continuously which reveals a slow declining of the polariton-polariton interactions caused by a decrease of the ground-state occupancy. This smooth process is typical for a condensed polariton system in the strong coupling regime. After 111 ps the emission is only marginally blueshifted compared to the lower polariton (LP) energy at this detuning.

In addition to the spectral evidence for photon lasing at the wire center at early times, the temporal arising of the emission in delay to the excitation time

is also supporting the interpretation of emission from a weakly coupled system. Photon lasing, just requiring inversion, can be observed subsequently after the excitation pulse, while for polariton lasing the hot carriers have to relax towards the LP branch with further relaxation down to the bottom of the branch before emission can be observed. Thus, the earlier emission peak in Fig. 4-2 corresponds to the emission of a photon laser in the weak coupling regime and the side peaks at later times are consistent with the emission of a polariton laser in the strong coupling regime.

To explain the spatial multi-mode structure, three possible scenarios are thinkable: imperfect projection of the wire onto the sample with the SLM due to diffraction, carrier redistribution and spontaneous pattern formation. The first and simplest possibility is that diffraction causes an inhomogeneous local pump density. This may lead to the situation that at some positions on the sample the threshold to the weak coupling due to screening effects is reached and at others it is not. Although this scenario is possible, it is very unlikely to happen since the density differences would need to be quite huge. Moreover, similar effects have been evidenced also for other excitation densities which contradict this explanation. The second possible explanation, carrier redistribution, is likely to happen since non-condensed carriers may undergo diffusive motion. This leads to a spatial shape of the background carrier density which is varying in time. For semiconductor samples excitons are the carriers to deal with and their typical diffusion constants are of the order of $10 - 20\ \frac{\mathrm{cm}^2}{\mathrm{s}}$ in GaAs based quantum wells [85]. Thus, this process takes place on a much slower timescale than the decay dynamics evidenced here. The explanation due to spontaneous pattern formation under nonresonant excitation seems to be more realistic. The boundary conditions of the optically created quantum wire and the influence of polariton interactions onto the condensate wave function as well as onto the relaxation dynamics could lead to a spatial ordering of the condensate density [86, 87]. For a deeper analysis of this spatial inhomogeneity, the dynamic results presented here have to be compared to results of polariton wire measurements imprinted under CW excitation.

4.2 Conclusion

In this chapter the results of time-resolved measurements with an all-optical created quantum wire were presented. Under nonresonant excitation the decay dynamics of the polariton system were investigated. It was possible to show that at early times the emission is strongly blueshifted and rapidly decaying. Furthermore, the main emission comes from the center of the wire. This behavior indicates a dominating photon lasing emission. This changes after a few tens of picoseconds, where the emission mainly stems from the edges of the wire. Additionally, the blueshift is much smaller and the decay dynamics are slower. Thus, at that time the dominant emission corresponds to polariton lasing.

Further studies, especially under continuous-wave excitation, are necessary for a better understanding of the decay dynamics and the spatial formation in quantum wires. Moreover, measurements with different optically created geometries should be investigated to provide the next steps towards functional optical elements.

Chapter 5

All-optical Control of the Polariton Flow on a Polariton Staircase

Spatially shaping the nonresonant excitation spot for a semiconductor microcavity system offers the possibility to influence the polariton condensate in a controlled, all-optical way. By creating an intensity staircase pattern with a spatial light modulator one can realize a polariton BEC which populates several discrete linear-momentum-stairs in a given direction. As described in Sec. 2.2.5, nonresonant excitation leads to the presence of noncondensed background carriers producing a mean-field repulsive potential corresponding to the excitation spot [57]. Since the sample is excited nonresonantly in this experiment and the potential varies in space due to the staircase pattern, the local condensate wave vector $\boldsymbol{k}_{\mathrm{con}}(\boldsymbol{r})$ (cf. Eq. 2.104) has to vary in space to overcome the energy difference caused by the different intensity levels of the staircase pattern. This modulation of the local condensate wave vector is necessary to fulfill the generalized Gross-Pitaevskii equation in the local density approximation which describes the condensate dynamic.

This chapter is organized as follows. The first Sec. 5.1 presents and discusses the results of far-field measurements under nonresonant and pulsed excitation with a pump spot shaped like a staircase. The comparison of the momentum emission pattern in the condensed regime with the one below the threshold of polariton lasing is part of this section. Furthermore, an analysis of the results at higher excitation power and different detection energies is presented. A comparison to numerical simulations shall emphasize the experimental results. Finally, the build-up of a single condensate state shall be confirmed with time-resolved measurements. The second section of this chapter contains results and discussion of spatially, spectrally and time-resolved measurements under nonresonant, pulsed excitation. First of all, emission patterns with an excitation density far below the threshold to polariton lasing are analyzed. Moreover, a discussion of the dynamics in the polariton lasing regime is presented and compared to numerical results. Afterwards, the dynamics at excitation densities at the crossover between polariton and photon lasing are examined. Finally, the emission patterns with an excitation density far above the threshold of photon lasing are shown and the blueshifts relative to the

LP mode are plotted versus the time for three different excitation densities. The chapter ends with a conclusion of the presented results.

5.1 Control of the Condensate's Momenta

One consequence of a spatially varying excitation density is a spatial variation of the blueshift which the condensed polaritons experience. This dependence of the blueshift on the excitation density is given through the fact that the blueshift arises due to polariton-polariton interactions and interactions of the polaritons with reservoir carriers such as electrons, holes and excitons. A condensate under steady-state conditions and with a Gaussian-shaped pump spot can be described as

$$\hbar(\omega_{\mathrm{con}} - \omega_{\mathrm{LP}}) = \frac{\hbar^2 k_{\mathrm{con}}^2(\boldsymbol{r})}{2m} + \Delta E(\boldsymbol{r}), \tag{5.1}$$

where $\hbar\omega_{\mathrm{con}}$ and $\hbar\omega_{\mathrm{LP}}$ are the energies of the condensate and of the minimum of the LP branch, respectively. $k_{\mathrm{con}}(\boldsymbol{r})$ represents the local condensate wave vector and m is the LP mass. The spatially varying blueshift is given by $\Delta E(\boldsymbol{r})$. Under the presumption of a single condensate state the variation in the blueshift can just be compensated by a change of the local condensate wave vector k_{con} to fulfill Eq. 5.1. Assuming a vanishing k_{con}-vector at the position of the pump intensity maximum the local wave vector is given as

$$|k_{\mathrm{con}}(\boldsymbol{r})| = \sqrt{\frac{2m[\hbar(\omega_{\mathrm{con}} - \omega_{\mathrm{LP}}) - \Delta E(\boldsymbol{r})]}{\hbar^2}}. \tag{5.2}$$

As described in section 3.4 the imprinted staircase spot has 16 steps with a spatially homogeneous pump intensity at each plateau and the intensity at the n-th step is denoted as:

$$I_n = (1 - \frac{n}{16})I_0, \tag{5.3}$$

where I_0 is the pump intensity of the highest plateau. For a pump spot shaped like this, one expects, inserting Eq. 5.3 into Eq. 5.2, a local condensate wave vector with the following behavior:

$$|k_{\mathrm{con}}(\boldsymbol{r})| = \sqrt{\frac{2m[E_0 - (1 - \frac{n}{16})E_0]}{\hbar^2}} = \sqrt{\frac{2mE_0}{16\hbar^2}} \cdot \sqrt{n}. \tag{5.4}$$

E_0 is the blueshift corresponding to the highest step of the staircase potential. So at each position on one plateau the same wave vector is demanded.

In Fig. 5-1 (a) the real-space image of the staircase patterned excitation spot is demonstrated realized by imaging the excitation beam after passing the SLM onto the slit of the monochromator in the energy integrated mode. Due to diffrac-

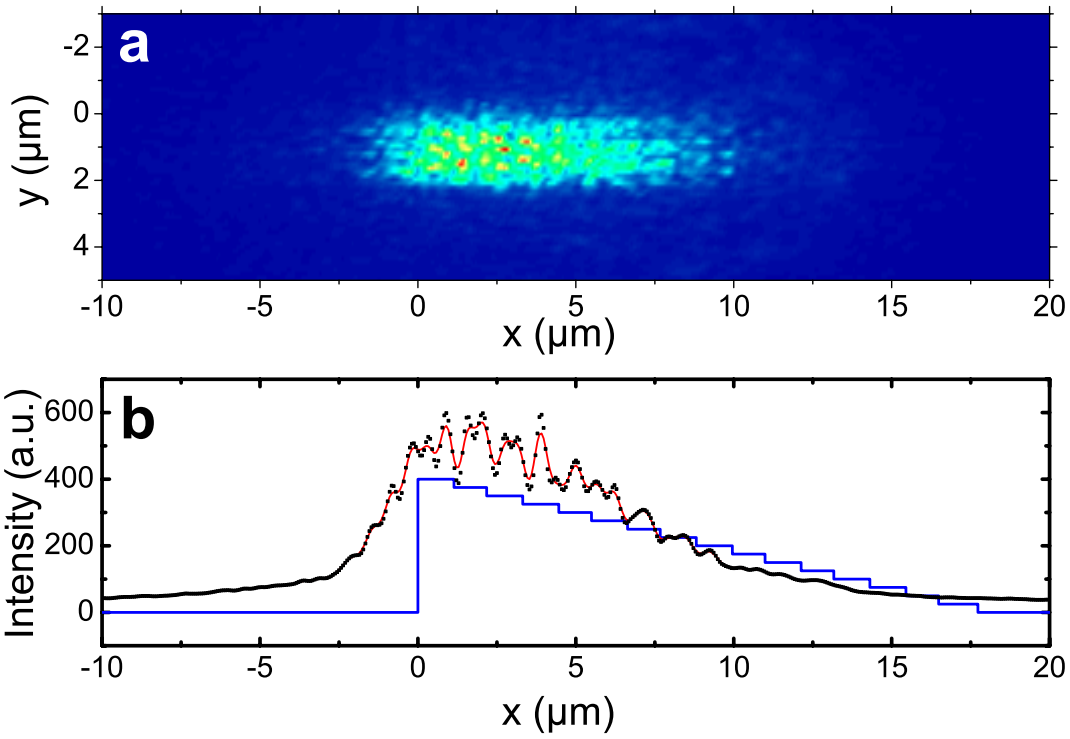

Figure 5-1: (a) A real-space image of the excitation spot shaped like a staircase. (b) The corresponding intensity profile integrated along the y-axis. The red line gives a three-point-smoothed guide to the eye. The blue line represents the target spatial shape of the excitation spot used as the input for the SLM.

tion and imperfect imaging it is hard to recognize the staircase pattern directly. Considering the intensity profile along the staircase gradient direction, which is integrated along the y-axis, the staircase behavior gets more visible, see Fig. 5-1(b). As a comparison the ideal profile is added to the experimental profile. Under the assumption of a single condensate state build-up, the shape of the emission in momentum-space is determined by the local shape of the excitation spot as discussed before. Such a momentum-space emission pattern for two different excitation densities is shown in the upper panels of Fig. 5-2. For excitation densities below the threshold of condensation (upper left panel) a broad distribution without peaks is visible. This changes abruptly with reaching the critical density of condensation where peaks at discrete values of the k_x direction are formed spontaneously. Fig. 5-2 (b) presents an emission pattern of the momentum distribution in the regime of polariton condensation. It has a detection energy centered around 7.3 meV above the LP energy of 1.6060 eV.

As mentioned before, the nonresonant excitation leads to an antitrapping potential corresponding to the pump spot profile. In the case of a staircase profile this results in a behavior of the condensate wave vector as described in Eq. 5.4. To make sure that it is due to the presence of the antitrapping background potential, which causes the quantization of the momentum distribution, the positions of the polariton density maxima are plotted against the index number of the corre-

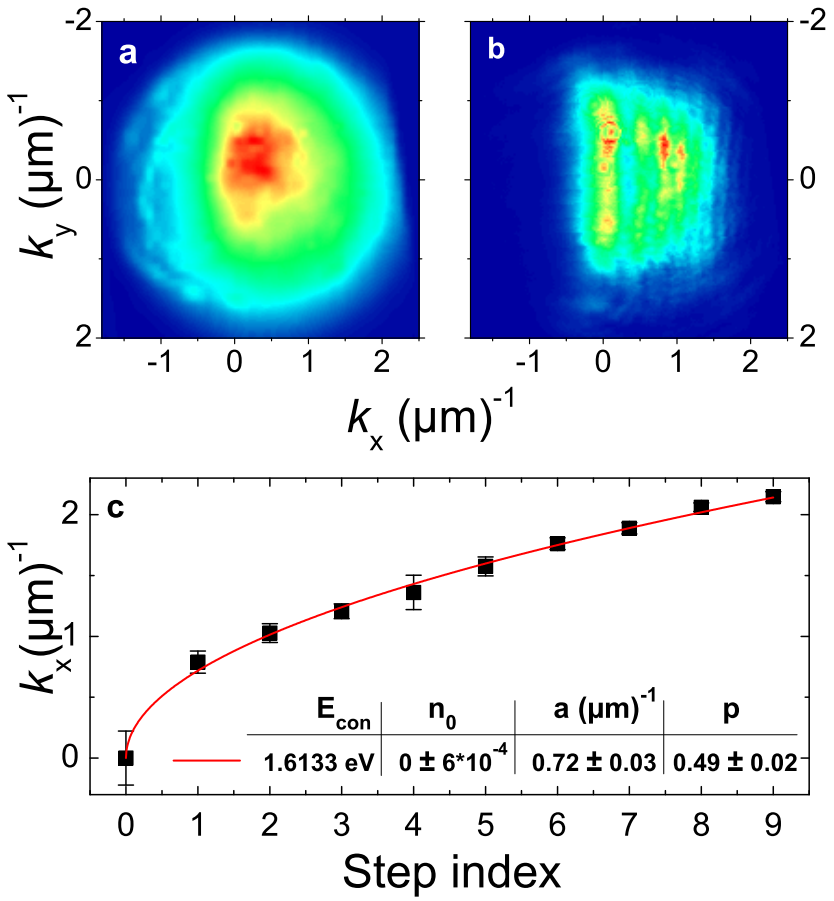

Figure 5-2: (a) The emission pattern of a uncondensed lower polariton branch in momentum-space at a detection energy of 1.6060 eV. At the same excitation density but different detection energy (1.6113 eV), the momentum-space emission pattern in the condensed regime (b) shows discrete momentum states in the k_x direction instead of a broad distribution as seen in panel (a). In panel (c) the center positions of the discrete maxima are plotted against the step index number. The expected square root dependence of the condensate wave vector for a staircase-shaped excitation spot (cf. Eq. 5.4) can be observed. The red solid line gives a power-law fit with fit parameters n_0, a and p. E_{con} corresponds to the central detection energy of the condensate.

sponding maximum. As can be seen in Fig. 5-2 (c), the results show a square root dependence just as expected for a staircase potential with linear step size (cf. Eq. 5.4). The solid line gives a power-law fit to the function

$$k_x(n) = a(n - n_0)^p. \tag{5.5}$$

With the fit parameter a it is possible to directly estimate the blueshift of the condensate to 7.4 meV with a higher precision than just by using the tunable spectral filter, which has a spectral width of 0.75 nm ($\approx$ 1.2 meV).

A closer examination of the intensity distribution along the k_y-axis for three

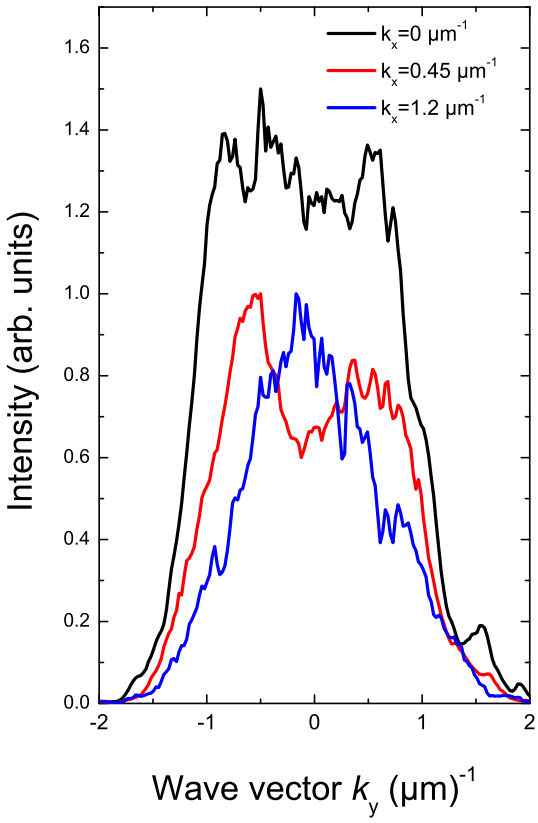

Figure 5-3: Intensity distribution along the k_y-direction for three values of k_x in the condensed regime, panel (b) in Fig. 5-2. The line at $k_x = 0.45$ µm^{-1} shows a double-peaked shape and differs significantly from the other lines.

different k_x-values (see Fig. 5-3) shows a noticeable deviation for $k_x = 0.45$ µm^{-1} compared to the other momentum-space distributions. In this case the distribution has a two-peak instead of a one-peak shape. Even though the behavior is very different, one could assume that step index 1 belongs to $k_x = 0.45$ µm^{-1}. This would lead to a clear mismatch between the fitted curve and the other results, whereas $k_x = 0.7$ µm^{-1} assigned to step index 1 gives nicely matching results. Therefore, at $k_x = 0.45$ µm^{-1} is likely an additional maximum. A possible explanation for this extra peak in the momentum distribution could be an incomplete momentum alignment along the x-axis of step index 1. Conceivable are also diffraction effects at the edge of the highest step of the staircase. Moreover, imperfections due to diffraction could also give rise to the creation of additional small plateaus. And a last alternative reason could be elastic scattering of polaritons from the highest plateau on a symmetric circle around $k = 0$.

To verify the previous results, time-integrated momentum-space polariton emission patterns were also gathered at another sample position and at higher excitation power. The results for detection energies of 1.6102 eV, 1.6123 eV and 1.6144 eV are presented in the upper panels of Fig. 5-4, respectively. In general, the results

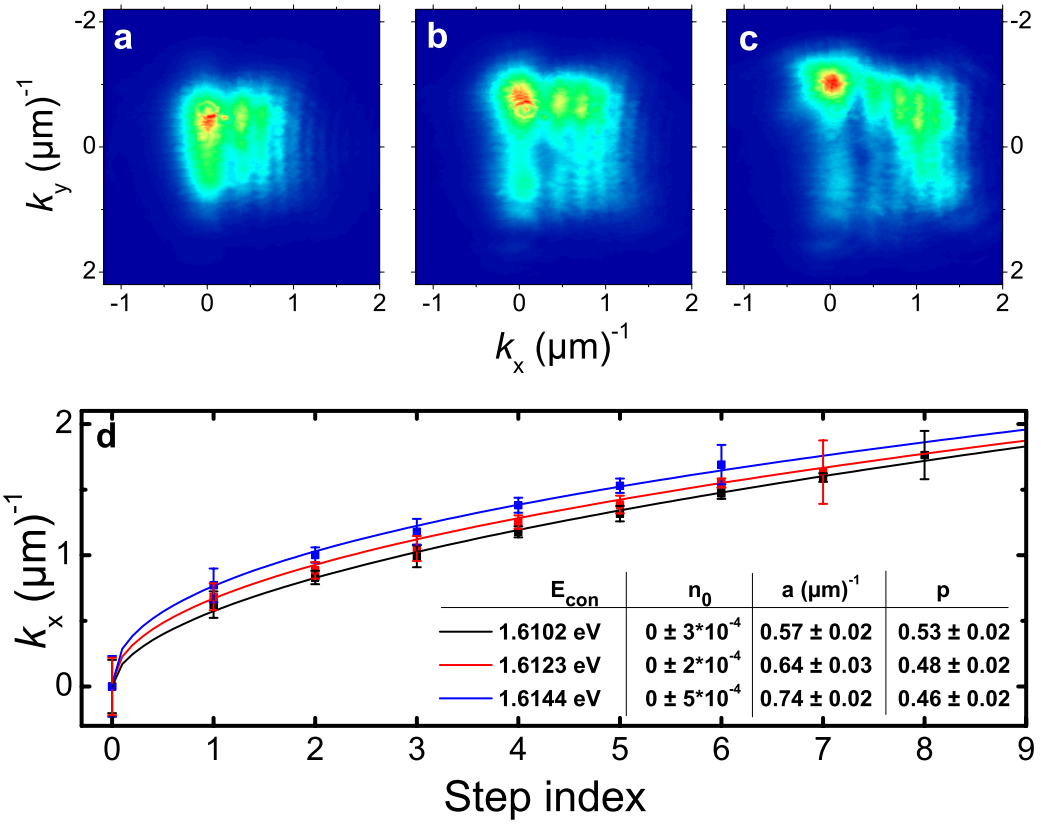

Figure 5-4: The emission patterns of a polariton condensate in momentum-space for a higher excitation density than in Fig. 5-2, but still below the threshold into the weak coupling regime. Panel (a)-(c) have different central detection energies of 1.6102, 1.6123 and 1.6144 eV, respectively. In panel (d) the center positions of the discrete maxima are plotted against the step index number of the staircase. The black curve corresponds to panel (a), the red to panel (b) and the blue to panel (c). The corresponding fit parameters n_0, a and p are given in panel (d). E_{con} is consistent with the central detection energies. The highest detection energy has the greatest k_x-values.

are comparable to the ones shown before, but two differences are recognizable. First of all, the stripe distance increases with increasing detection energy. Second, there is a redistribution of the polariton density from $k_y = 0$ towards larger values of k_y with growing detection energy. Fig. 5-4 (d) shows again the positions of the polariton density maxima in momentum-space plotted against the step index of the staircase. Power-law fits indicate the square root behavior with only small deviations from the ideal case. The recognized increase of the stripe distance can be seen in the shift of the curves to higher k_x-values with increasing detection energy.

In Fig. 5-5 the effect of a stripe distance increase is demonstrated by plotting the intensity profile of the k_x momentum distribution. The shift to higher positions is marked with a dashed green line for step index number 1, 4 and 6. In both plots the first maximum with step index number 0 stays unchanged. To check whether the power-law fits are suitable results or not, the fit values corresponding to the blueshift are compared to the central detection energy of

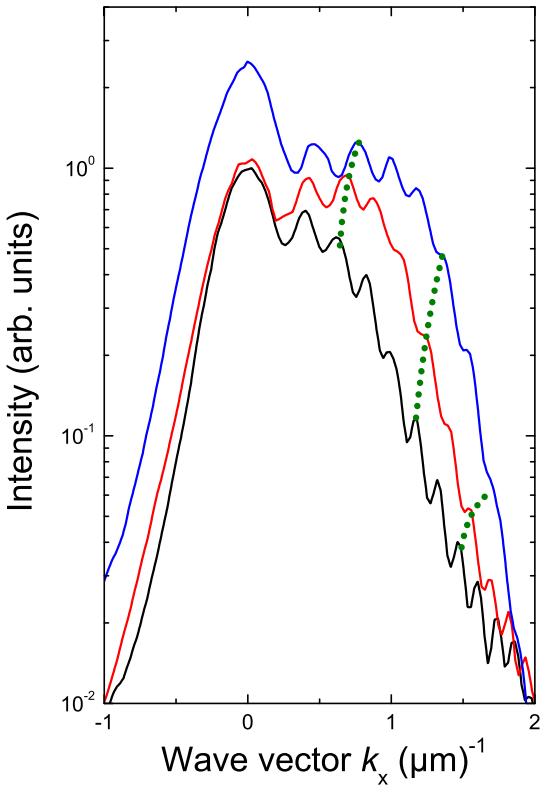

Figure 5-5: Polariton momentum-space distribution integrated along k_y with the black, red and blue curves corresponding to panels (a), (b) and (c) from Fig. 5-4, respectively. The green dotted lines match the maxima of step index 1, 4 and 6 and emphasize the increase of the stripe distance for growing detection energy.

each momentum-space distribution. With blueshifts of 4.7, 5.9 and 7.9 meV from the LP energy of 1.6060 eV one obtains emission energies of 1.6107, 1.6119 and 1.6139 eV,respectively, which is in a good agreement with the central detection energies mentioned before.

An explanation for the increase of the stripe distance is the decrease of the background carrier population starting with the highest population right after the excitation pulse. Since the background carrier number decreases the emission energy shifts to smaller values. Consequently, the momenta of the condensed polaritons at each single step also decrease. In this way, it is possible to influence the momenta of the condensed polaritons by varying the blueshift with a change in the imprinted potential.

While the results shown so far are consistent, it is still noticeable that the blueshifts are quite large and one has to make sure that effects from a transition into the weak coupling regime can be excluded. The transition into the weak coupling regime takes place when the blueshift due to polariton-polariton and polariton-carrier interactions becomes comparable to the energy difference between

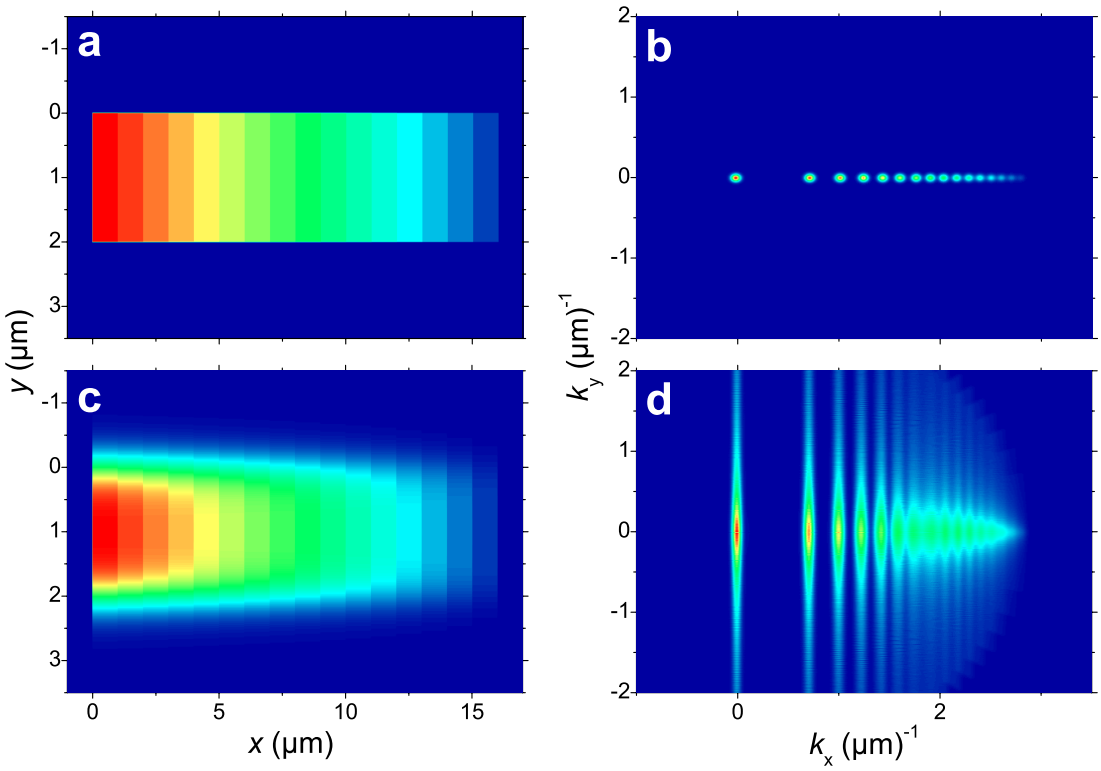

Figure 5-6: The emission patterns of a polariton condensate with an ideal staircase-shaped pumping spot in real- (a) and momentum-space (b). Furthermore, the emission patterns of a polariton condensate created by an imperfect staircase-shaped pumping spot in real- (c) and momentum-space (d). The smoothed edge along the y-axis causes a large broadening in the k_y-direction. In both cases only geometrical broadening is considered.

the LP and the bare cavity mode. For this sample it was already shown in earlier measurements under similar experimental conditions that the transition into the weak coupling is expected to be at a blueshift of about 7.7 meV [73]. While the blueshift observed in Fig. 5-2 is smaller than that, it surmounts the value from Fig. 5-4. Contemplating this case, it is obvious that the emission is not coming from the area around $k_y = 0$ but from higher k_y-values. While Coulomb interactions are the main factor leading to a blueshift for small k-values, also the kinetic energy of the polaritons has to be taken into account for higher momenta. The observable screening of the excitons at the threshold from the strong into the weak coupling is solely due to Coulomb interaction. This could be the reason for the minimal condensate emission at $k = 0$ seen especially in Fig. 5-4 (c), as the strong coupling would be already broken. However, the major part of the emission comes from higher k-values of at least 1 µm^{-1}. At this point the polaritons have gained already a kinetic energy of about 1 meV, which points out that the blueshift caused by Coulomb interactions is about 7 meV and therefore still below the transition to the weak coupling regime.

In fact one would expect from Eq. 5.4 due to quantization discrete momenta

instead of discrete lines in momentum space. So how can this behavior, visible in all measured emission patterns, be explained? The broadening of the polariton distribution in momentum space due to the small spot size in k_y-direction is caused either by position-momentum uncertainty or by imperfections of the shape of the potential due to diffraction. To find out which of these two effects are playing a role in the broadening of emission in momentum-space shown before, polariton distributions from a phenomenological model were calculated for the ideal staircase and for an imperfect potential due to diffraction which is called geometrical broadening from now on.

The theoretical model for the simulations in Fig. 5-6 is based on the Gross-Pitaevskii Equation (GPE) (cf. equation 2.98). In this calculation the dominant contribution to the blueshift of the condensate mode is the effect of the shape of the pump spot. Effects such as polariton-polariton interactions or disorder are neglected or rather contribute only in a way that there is a slight changing in the pump spot shape. Under the assumption of a homogeneous system with a local varying pumping rate it is possible to apply a local density approximation. This leads to a condensate wave vector k_{con} which depends only on the local pump rate. Additional quantum pressure terms in the GPE can be neglected. Even though these assumptions are not quite right for a staircase potential, it is acceptable to treat effects which go beyond these assumptions as a variation of the pump spot.

For calculation of the momentum-space distribution it is necessary to separate the information of the x- and y-components of the wave vector. The pumping spot is classified into stripes in the y-direction for constant x-positions. Within each stripe the k_x-value is expected to be the same at each position and is given by the difference between the highest pump density of the whole pump spot and the highest pump density inside the stripe. To obtain the momentum-space distribution the staircase pump spot has to be Fourier transformed and, therefore, sigmoidals are used to simulate the plateaus of the staircase. For the imperfect case the edge steepness of these sigmoidals is varied.

The upper panels of Fig. 5-6 show the real- and momentum-space distributions of an ideal staircase potential. Just as expected, a full quantization in momentum-space is recognizable. The case of a potential taking geometrical broadening into account is demonstrated in the lower panels of Fig. 5-6. In real-space a clear deviation from the ideal staircase is noticeable causing a discrete-line-shaped momentum-space pattern. These results are already in good accordance with the experimental results. However, there are still some deviations such as broader maxima in the k_x-direction of the experimental data. One explanation for this broadening could be the disregard of the disorder in the calculations. Disorder in the sample adds some random value to the local wave vectors. Another explanation might be connected to the spectral width of the tunable liquid crystal filter of roughly 1.2 meV. Under pulsed excitation, just as it is in these experiments, the energy of the condensate will decrease with increasing time due to the decrease of the background carriers with time. As a consequence, the line distances

decrease as well. Thus, the experimental momentum-space distribution is rather an average of all momentum-space distributions corresponding to the condensate energies within the transmission window of the filter. This averaging is leading to the observable broadening of the maxima in k_x-direction.

Further it has to be checked if next to geometrical broadening also broadening caused by uncertainty plays a role. With a rectangular, sigmoidal or Gaussian spot shape the standard deviation of the underlying real-space polariton distribution in y-direction is about $\sigma_y \approx 0.85$ µm for the 2 µm full-width-at-half-maximum step width. With this deviation it is possible to estimate the lower bound of the polariton wave vector uncertainty in y-direction to $\sigma_k > 0.59$ µm^{-1}. Comparing this with the standard deviation of the wave vector in the simulated data, which has a value of 0.7 µm^{-1} or even larger, it is clear that the broadening is larger than the value imposed by uncertainty. Therefore, only geometrical broadening plays a significant role. For really high excitation densities, the effective spot shape in y-direction is more Gaussian- than steplike, which leads to the effect that the polaritons get accelerated ballistically to regions outside of the pump spot potential. This is the explanation for the spotted redistribution into the k_y-direction seen in the results of Fig. 5-4. Furthermore, it is obvious that the broadening in momentum-space is close to the limit of uncertainty which means that the quality of the imprinted potential is sufficient. But the determination of the lower bound of the polariton wave vector takes place in the limit of very short polariton lifetime. Hence, as the polaritons move away from the pump spot at high excitation densities, the real spatial polariton distribution will be broader than the imprinted step width. Moreover, which step width is needed to reach the uncertainty limit in the case of a perfectly imprinted potential as shown in Fig. 5-6? With a typically geometrical broadening of 0.1 µm^{-1} for the ideal case, a spatial width of about 10 µm (full-width-at-half-maximum) would already be required to reduce the uncertainty-limited broadening to the magnitude of the geometrical broadening.

In the beginning of this chapter one presumption for the staircase pump spot was that the polariton condensate forms at a single energy state and not several condensates at different energies. By performing spatially, spectrally, and time-resolved measurements it is checked whether a single condensate build-up is observable using a staircase shaped pump spot or not. The results of these measurements are shown in Fig. 5-7. The upper panels give the emission patterns early in the pulse and the lower panels show the emission patterns at later times. On the right side the excitation power is so intense that the system is in the weak coupling regime at early times, which is noticeable in terms of the large blueshift compared to the LP energy of 1.6060 eV. If the excitation power is reduced, as in the case on the left side, a build-up of a single condensate mode blueshifted compared to the LP mode is recognizable. With increasing time the blueshift decreases since the background carrier density is decreasing too. This decrease is visible in both cases, for the high excitation power in the weak coupling regime and for the excitation power reaching condensation staying in the strong coupling

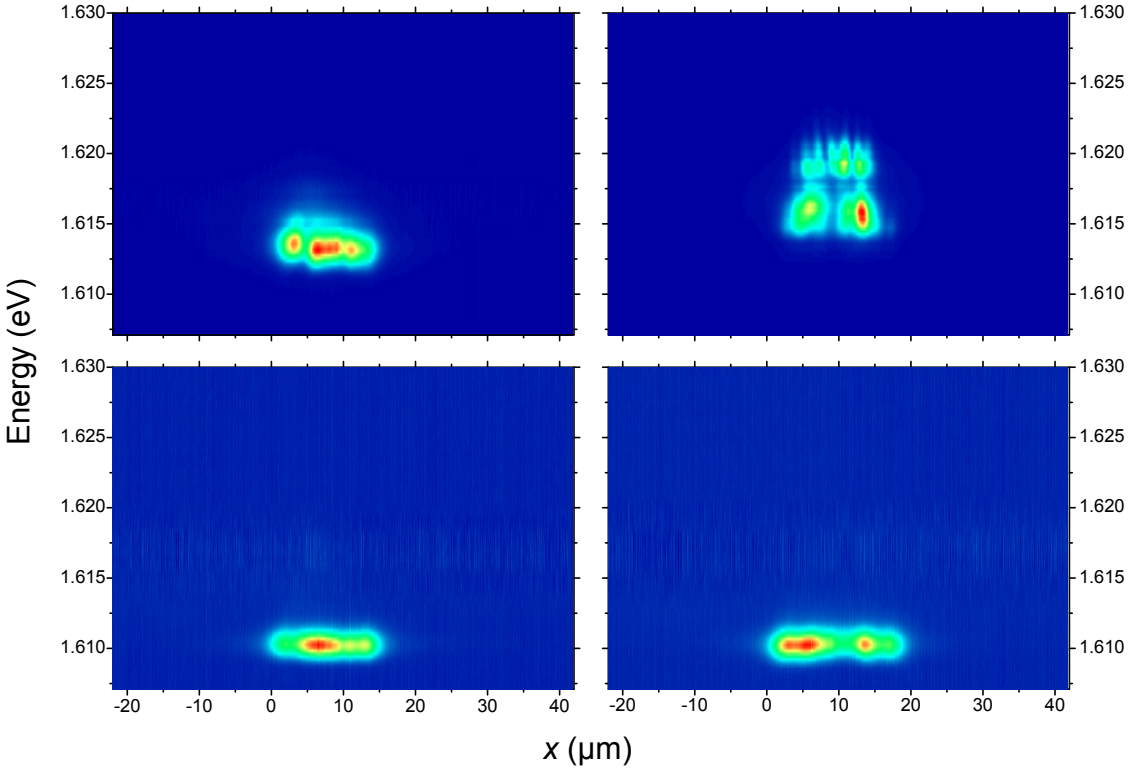

Figure 5-7: Spectrally resolved emission patterns in real-space for excitation densities below (left side) and above (right side) the threshold into the weak coupling regime. The panels in the upper row show emission patterns early within the pulse, while in the lower row the emission patterns after 90 ps (left) and 120 ps (right) are shown.

regime. However, in the case of the higher excitation power even the LP mode at later times stays fragmented. This behavior is most probably due to direct coupling of the background carriers to the light field in the lasing regime. They do not need to relax spontaneously towards the LP branch as it is the case in the strong coupling regime. While the background carrier population decays with a rate which is constant everywhere, spatial hole burning in the carrier population caused by stimulated emission takes place. This ends up with a strong reshaping of the potential.

5.2 Spatial and Temporal Dynamics

In the previous section it was shown that a system with a blueshift E_0 at the position of the highest excitation density builds up a single condensate energy state and compensates the energy mismatch caused by the external staircase potential by varying the local condensate wave vector. Hence, a local polariton flow is created. In this section the influence of this flow on the spatial emission is of interest.

In Fig. 5-8 the dynamics at excitation below threshold ($P = 1$ mW) are presented in spatially, spectrally, and time-resolved emission patterns with an inte-

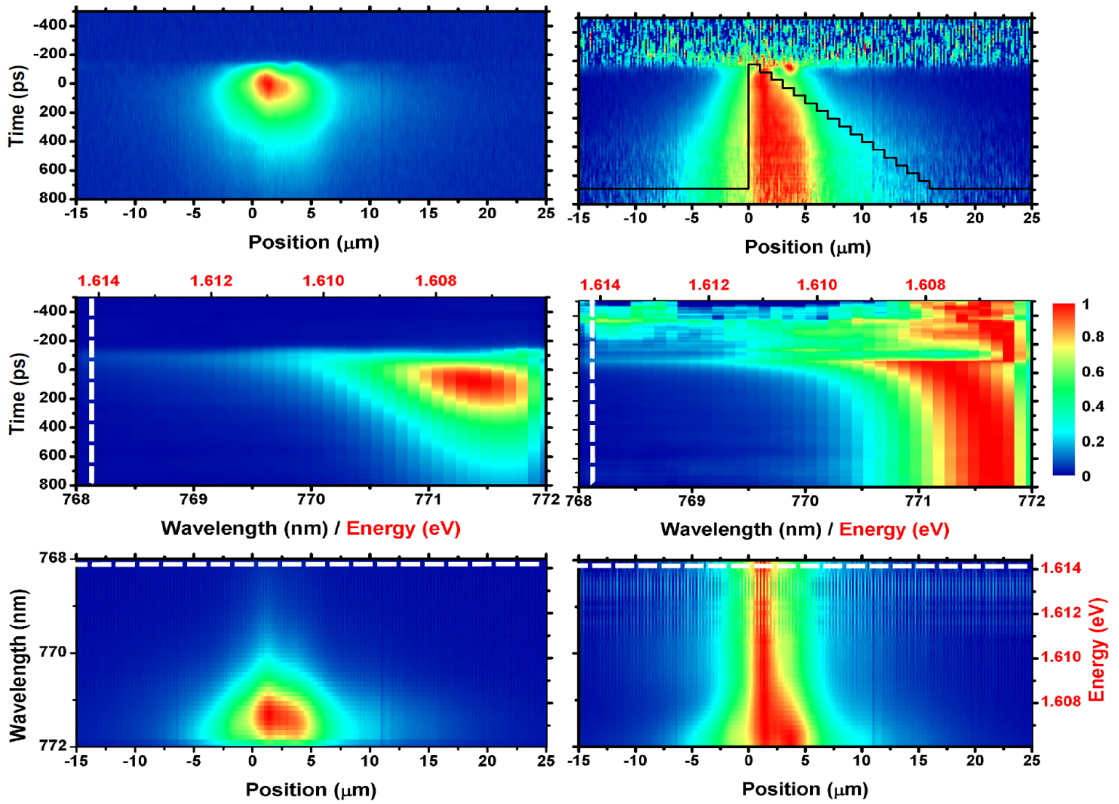

Figure 5-8: Nonnormalized (left) and normalized (right) polariton emission patterns showing the spatially, spectrally, and time-resolved dynamics under nonresonant excitation with a pumping power of 1 mW. The emission pattern is integrated over all energies (upper panels), all positions (middle panels) or all times (bottom panels). The dashed white line indicates the bare-cavity mode energy. The solid black line in the upper panel on the right side represents the target pump-spot shape.

gration over all times, all positions and all energies, respectively. The origin of the time axis is set to the time of occurrence of the peak intensity in the nonnormalized plots. Due to nonresonant excitation of the sample, the arising emission intensity peak is not synchronized to the impact of the excitation pulse. The pattern demonstrates an emission mainly coming from the highest staircase step, which is equal to position 0 and shows quite slow temporal dynamics. Moreover, the emission stems primarily from the energy of the LP at $k_{||} = 0$ and according to that the system is clearly in the strong coupling regime without condensation yet and far away from the energy of the bare cavity represented by the dashed white line.

To show this behavior even clearer, the emission patterns are also shown in normalized plots in Fig. 5-8. Hence, the highest intensity of each row gets normalized to unity for all three panels. While the plots shown before have a color scheme from 1 to the highest intensity, here in the normalized plots they range from 0 to 1. In the top panel the target pump spot shape is indicated by the solid black line. The normalized emission pattern reveals that a certain time is needed for a build-up of the system until the shape of the emission gets relatively constant

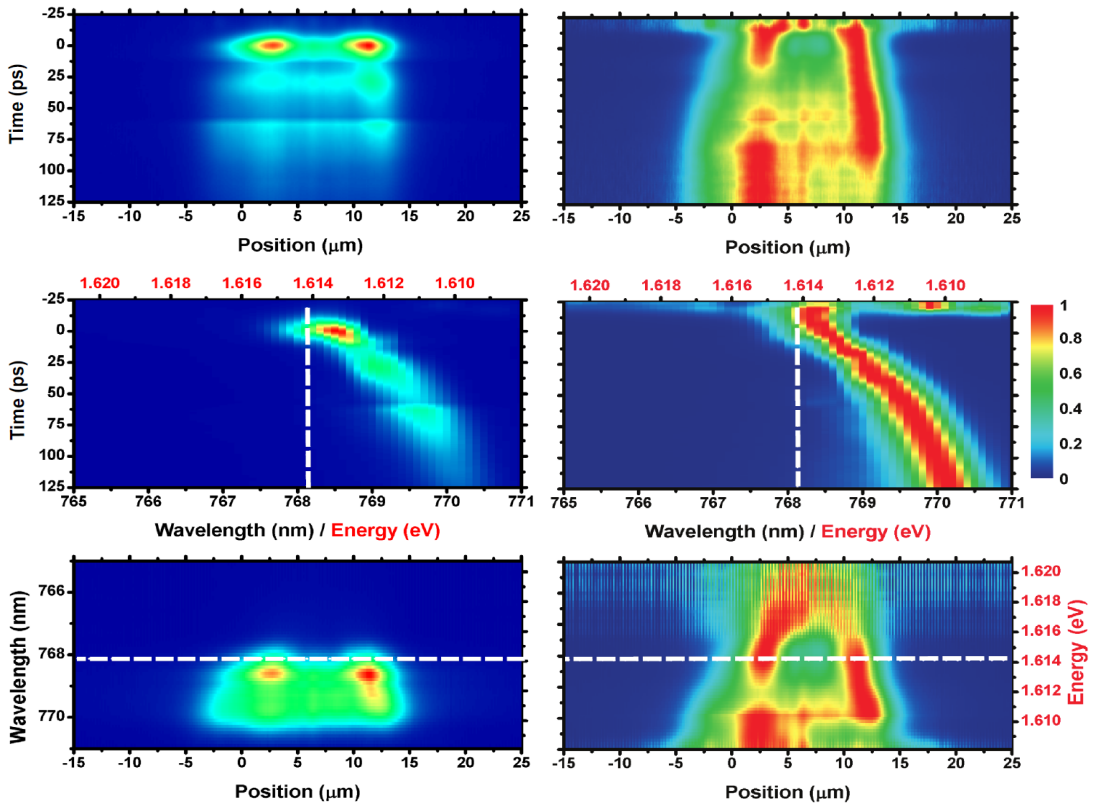

Figure 5-9: Nonnormalized (left) and normalized (right) emission patterns showing the spatially, spectrally, and time-resolved dynamics under nonresonant excitation with a pumping power of 8 mW. The emission pattern is integrated over all energies (upper panels), all positions (middle panels) or all times (bottom panels). The dashed white line indicates the bare-cavity mode energy.

in time. Especially the normalized pattern shows a rather good accordance to the imprinted staircase pattern.

If the excitation power is increased up to about 8 mW, then a drastic change in the emission pattern takes place as can be seen in Fig. 5-9. In real-space the condensate shape does not take the form of the imprinted staircase shape of the excitation beam as expected for nonresonant excitation in the polariton lasing regime. Instead it looks like two separated spots, one at the top and one at the bottom of the staircase potential. Energetically a clear blueshift from the LP mode becomes visible but the emission energy is still below the one of the bare cavity mode, therefore, the system must be in the regime of condensation. With increasing time a smooth decrease of the condensate energy towards the LP energy takes place. The two spot behavior can be explained by a spatially varying exciton population creating a linear potential in addition to the existing imprinted spot potential. First the main emission comes from the top of the staircase potential. As shown in the upper panel, after a few picoseconds the polariton population at the beginning of the staircase dies out completely and all polaritons have fallen down the linear potential and gather at the end of the staircase. For about 70 ps mainly this region is populated until there is again a jump to the beginning of the

staircase. The emission is only slightly blueshifted by now, as can be seen in the lowest panel of the normalized plot.

For a detailed analysis of the dynamics, presented in Fig. 5-9, numerical simulations based on the generalized Gross-Pitaevskii equation were performed. For the used GPE, cf. Eq. (5.8), a few further assumptions are needed. First of all, a nonresonant time-dependent excitation density $P(x,t)$, which creates electrons and holes in the sample, is defined. As the shape of the excitation spot is step-like the pulse is assumed to be sigmoidal in space and has a duration of 3 ps. The free electrons and holes are represented by a free-carrier density $n_{\mathrm{R1}}(x,t)$. The free carriers can relax either nonradiatively with a decay rate γ_{NR} or they form excitons with the rate κ_{12}. This formation rate depends also on the density of the electrons and holes and is proportional to the free-carrier density $n_{\mathrm{R1}}(x,t)$. By choosing $\kappa_{12} = (n_{\mathrm{R1}})/5000\ \mathrm{ps}^{-1}$ the exciton formation rate lies in between 2 ps and 1 ns for typical excitation densities, in agreement with measurements by Szcytko et al. in 2004 [88]. The formed hot excitons can now relax further down to the polariton branch or they decay nonradiatively at a exciton decay rate γ_{R}.

The dynamics of the reservoirs of the free carriers n_{R1} and excitons n_{R2} is then given by

$$\frac{dn_{\mathrm{R1}}(x,t)}{dt} = P(x,t) - \gamma_{\mathrm{NR}} n_{\mathrm{R1}}(x,t) - \kappa_{12} n_{\mathrm{R1}}(x,t), \tag{5.6}$$

and

$$\frac{dn_{\mathrm{R2}}(x,t)}{dt} = \kappa_{12} n_{\mathrm{R1}}(x,t) - \gamma_{\mathrm{R}} n_{\mathrm{R2}}(x,t) - \beta\alpha n_{\mathrm{R2}}(x,t)|\Psi(x,t)|^2. \tag{5.7}$$

Here, $\Psi(x,t)$ is the one-dimensional mean-scalar-polariton field, which describes the gain-trapped polaritons evoked through a small pump spot [89]. α stands for the scattering rate of the excitons into the condensate and β quantifies the backaction of the condensate on the exciton reservoir. This backaction is required to be able to reach a steady state also above the threshold where the in-scattering exceeds the out-scattering rate [90].

The dynamics of the lower polariton branch can be described with the GPE in the following form:

$$\begin{aligned}\frac{d\Psi(x,t)}{dt} = &\left\{\frac{i\hbar}{2m_{\mathrm{LP}}}\frac{\partial^2}{\partial x^2} - \frac{i}{\hbar}g|\Psi(x,t)|^2 - \frac{i}{\hbar}\left[g_{\mathrm{R}} n_{\mathrm{R2}}(x,t) + g_{\mathrm{NR}} n_{\mathrm{R1}}(x,t)\right]\right\}\Psi(x,t) \\ &+ \left\{\frac{1}{2}\left[\alpha n_{\mathrm{R2}}(x,t) - \gamma_{\mathrm{con}}\right]\right\}\Psi(x,t),\end{aligned} \tag{5.8}$$

where m_{LP} is the lower polariton mass and γ_{con} the polariton decay rate from the cavity and corresponds to the inverse polariton lifetime. g, g_{R} and g_{NR} denote

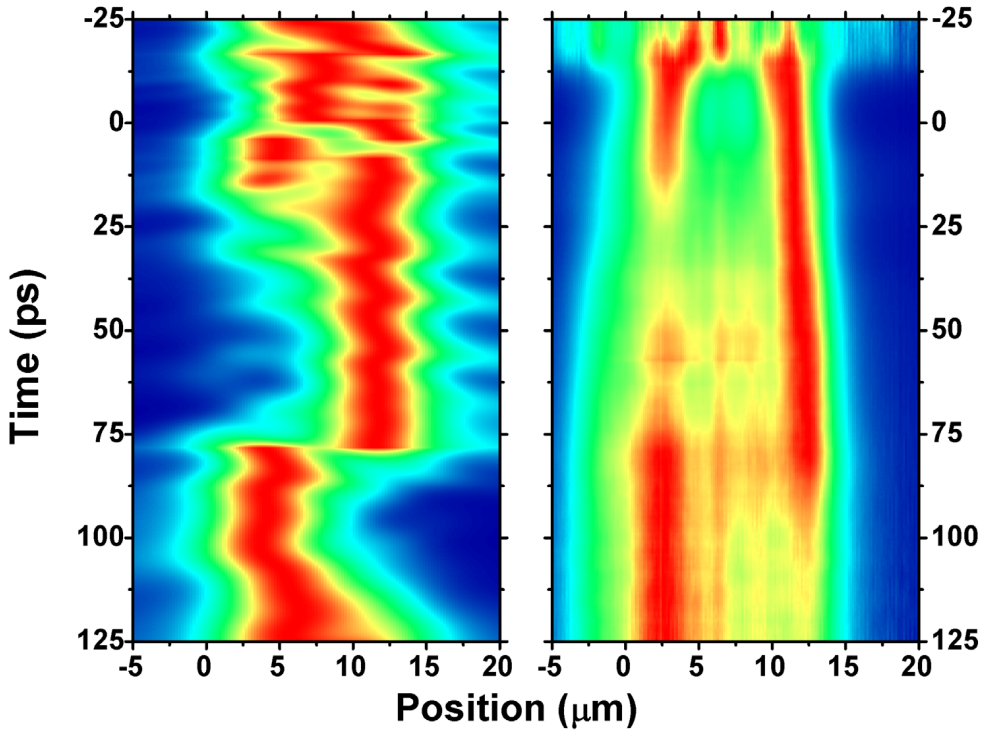

Figure 5-10: Comparison of simulated (left panel) and measured (right panel) normalized spatially- and time-resolved emission for excitation slightly above threshold (8 mW excitation power). The prominent switching process around 75 ps is well reproduced.

the polariton-polariton, the polariton-exciton and the polariton-free carrier interaction strength, respectively. For simulations it is important to choose realistic parameters. First of all the polariton-polariton interaction strength is chosen to be $g = 4\ \mu\text{eV}\mu\text{m}^2$ on the basis of measurements performed by the group of Jacqueline Bloch in 2011 [91]. The exciton-polariton interaction strength is selected to be twice as large as g since the interactions take place via the excitonic part of the polariton wave function and the polaritons of the implemented measurements have a photonic and excitonic Hopfield coefficient of about 0.5. The polariton-free-carrier interaction strength is chosen to be $g_{\text{NR}} = 3.5g$, so that this leads to reasonable total interaction energies. Both, the nonradiative decay rate of free carriers and the nonradiative exciton decay rate, are much slower than the polariton decay rate of $\gamma_{\text{con}} = 0.2\ \text{ps}^{-1}$. Therefore, it is set to $\gamma_{\text{R}} = \gamma_{\text{NR}} = 0.01\gamma_{\text{con}}$. The exciton scattering rate into the condensate is considered to be $\alpha = 0.33\ \text{ps}^{-1}$ and the backaction of the condensate on the reservoir shall be given by $\beta = 0.5$.

In Fig. 5-10 the simulation is compared to the experimental data. It is obvious that there is a qualitative agreement in the long-term behavior and when it comes to the sudden spectral change of the peak position after about 75 ps. Therefore, this switching has a physical meaning and is not only observed due to bad experimental conditions. A local flow velocity towards the lower end of the

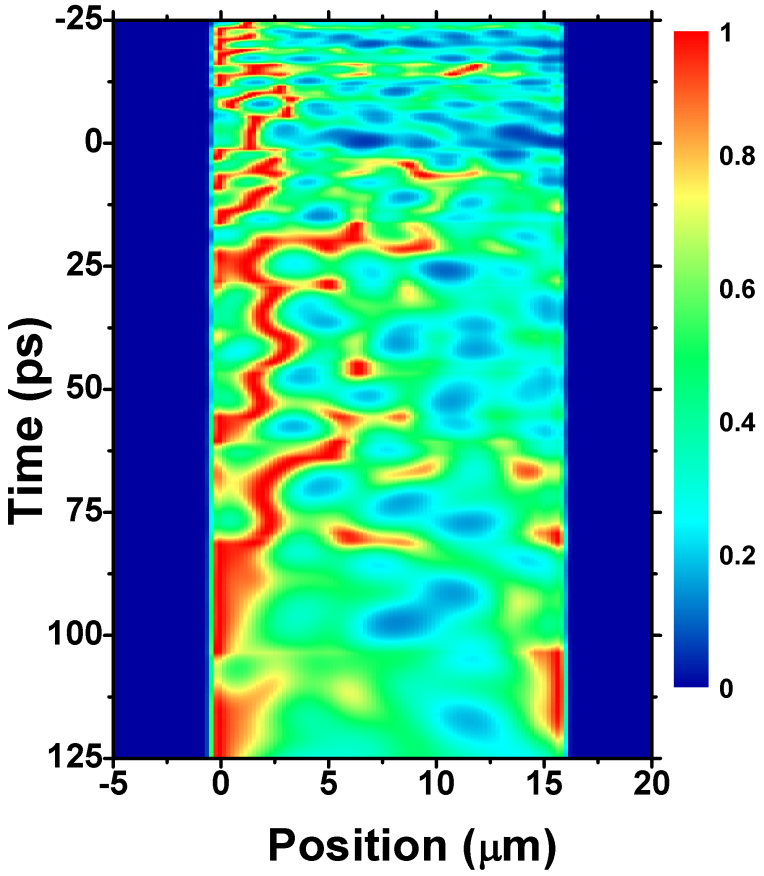

Figure 5-11: Simulated normalized dynamics of the active exciton reservoir for excitation slightly above threshold (8 mW excitation power).

staircase which increases with increasing distance to the upper end of the staircase is observable, so that one synchronized polariton condensate is established. This leads to a strong population of the bottom of the staircase. Spatially there is no evidence of emission beyond the pump spot which is due to the short lifetime of the polaritons in the sample of only a few picoseconds. This fact supports the model of a gain-trapped condensate, since there is no gain beyond the extent of the pump spot and the length scale—over which polaritons can travel—is limited by the polariton lifetime. Hence, the emission coming from the lower end of the staircase is rather due to the fact of spatial separation of the polariton condensate and the pump spot caused by repulsive interactions of polaritons with carriers of the reservoir. Similar results shown for a lithographically confined polariton pattern are presented in the publication of Ferrier et al. [91]. Thus, the asymmetry of the pump spot leads to an asymmetry in the polariton pattern and entails the flow down the staircase potential. Additionally, the potential landscape is influenced by the separation of the pump spot maximum and the one of the condensate.

For a detailed analysis of the condensate-reservoir interaction a simulation of the normalized exciton-reservoir population is shown in Fig. 5-11. The nonlinear

backaction of the condensate on the reservoir is the strongest at the position of the condensate maximum noticeable by stimulated scattering towards the condensate. This means that the reservoir is depleted strongly in the regions of low pump intensity, i.e., at the right side of the staircase. On the contrary, at the upper end of the staircase the depletion is quite slow. This behavior leads to a sharpening of the staircase potential. With elapsing time the population pattern of the reservoir becomes more complicated; peaks occurring at varying positions.

The second jump in the emission pattern towards the upper end of the staircase, observed in the experimental as well as in the simulated data, is based on exactly the opposite effect of what caused the flow towards the lower end of the staircase. With increasing time the density of reservoir carriers decreases and consequently the potential becomes shallower. With the decrease of the repulsive potential the flow towards the lower end of the potential gets reduced as well. At first, this reduction can be compensated by the arising sharpening of the potential, but later on the flow is so weak that again an overlap between the condensate and the population of the reservoir at the upper end of the staircase is occurring. Since the depletion of the reservoir at that position was rather slow at earlier times, stimulated scattering towards the condensate gets efficient now at the top of the staircase. At this point it should be noted that the switching of the maximum of the condensate from one end to the other is not consistent with polaritons moving from the lower to the upper end of the staircase. Instead it is more likely a shortage of new polaritons flowing in from the top of the staircase or scattering in from the reservoir at the bottom of the potential. A lack of polariton scattering becomes apparent in the simulation of the reservoir population (Fig. 5-11). At the time of the second switch, the population of the reservoir is depleted in the region of $2.5-12.5$ µm, which causes a reduction of the polariton flow towards the end of the staircase. After the polaritons in this region have left the microcavity, their total population decreases as well. Hence, the switching dynamics take place on a time scale of a few picoseconds − corresponding to the lifetime of the polaritons. By increasing the lifetime of the polaritons in the simulation, this assumption seems to be confirmed even though it should be noted that an exact reproduction of the dynamic switching process is not possible.

In addition to the effects discussed above, some effects may play a role which are not considered so far. First of all, the polariton flow velocity itself may be relevant, since there is a huge difference in the polariton propagation whether the velocity is subsonic or supersonic [71]. For resonant continuous-wave excitation the influence is already well known [92, 93]: the local sound velocity increases with the square root of the local polariton density. For a subsonic flow velocity an inhibited scattering at defects is expected, and for a supersonic flow a Cherenkov-like scattering arises. Therefore, the resonant excitation determines the flow velocity, while the local sound velocity depends on the polariton density. Thus, it is possible to switch between the regime of subsonic and supersonic velocity by varying the pump intensity. For nonresonant excitation, interactions between polaritons and reservoir carriers play a significant role [94] and dominate over polariton-polariton

interactions. Accordingly, the situation for nonresonant excitation is more complicated since a critical Landau velocity does not exist but a superfluid density can be reached [95, 96]. Other effects which are not considered in the model because of the short time scales are intra-condensate relaxations and spatial diffusion of excitons [97]. Further, inactive excitons which cannot scatter directly to the polariton branch have been neglected, although they are mainly responsible for influencing the relaxation dynamics. In the model used for the simulation the reservoir of free electrons and holes has the same purpose, nevertheless the inactive excitons may have greater impact than just influencing the relaxation dynamics. The number of excitons created in a certain time interval depends on the squared free-carrier density which leads to a change in the potential shape of the free carriers. With time the potential shape will become more homogeneous. And since the total potential created by free carriers and excitons will stay constant, the potential of the free carriers has to roughly preserve its shape, but the exciton reservoir which is coupled to the condensate dynamics will change rapidly. By the creation of inactive excitons, in addition, a slowly varying potential is formed which is only influenced by exciton diffusion and other comparably slow mechanisms. Therefore, the inactive-exciton formation rate can affect how the effective potential experienced by the polaritons changes over time.

As a next step, the excitation power is increased so that the dynamics at the crossover between polariton lasing and photon lasing can be studied. With 30 mW pump power the emission is significantly above the threshold of condensation and it changes considerably as can be seen in the emission pattern of Fig. 5-12. Right after the excitation pulse the emission is observable at the whole width of the imprinted staircase, although the pattern is modulated and not very homogeneous throughout the total width. As can be seen in the middle panels of Fig. 5-12, the emission is spectrally broad at that time. With an emission energy 4 meV above the bare cavity energy, the emission energy rapidly drops until the energy of the cavity is reached. This is followed by a continuous exponential decay while the spatial shape of the emission changes. The main emission is now coming from the center of the pump spot and for about 100 ps also from the top of the staircase. A third maximum arises at the end of the staircase with about half the intensity of the other two maxima. To analyze the dynamics again without experimental impacts a simulation of the system for this excitation density was performed.

Fig. 5-13 shows the results under usage of the same parameters as before. The direct comparison with the experimental data reveals a general analogy, such as the emission maxima at the center of the excitation spot and a dip after roughly 15 ps. But also some features, observed in the experimental data as the emission maxima at the upper end of the staircase, are missing. Most likely this deviation is due to the fact that the system has already reached the weak coupling regime and started to lase which is not considered in the simulations. Another feature which indicates photon lasing is the fast spatial variation of the blueshift next to the emission maxima, since the free carrier population in the weak coupling regime can couple directly to the light field which influences the potential shape

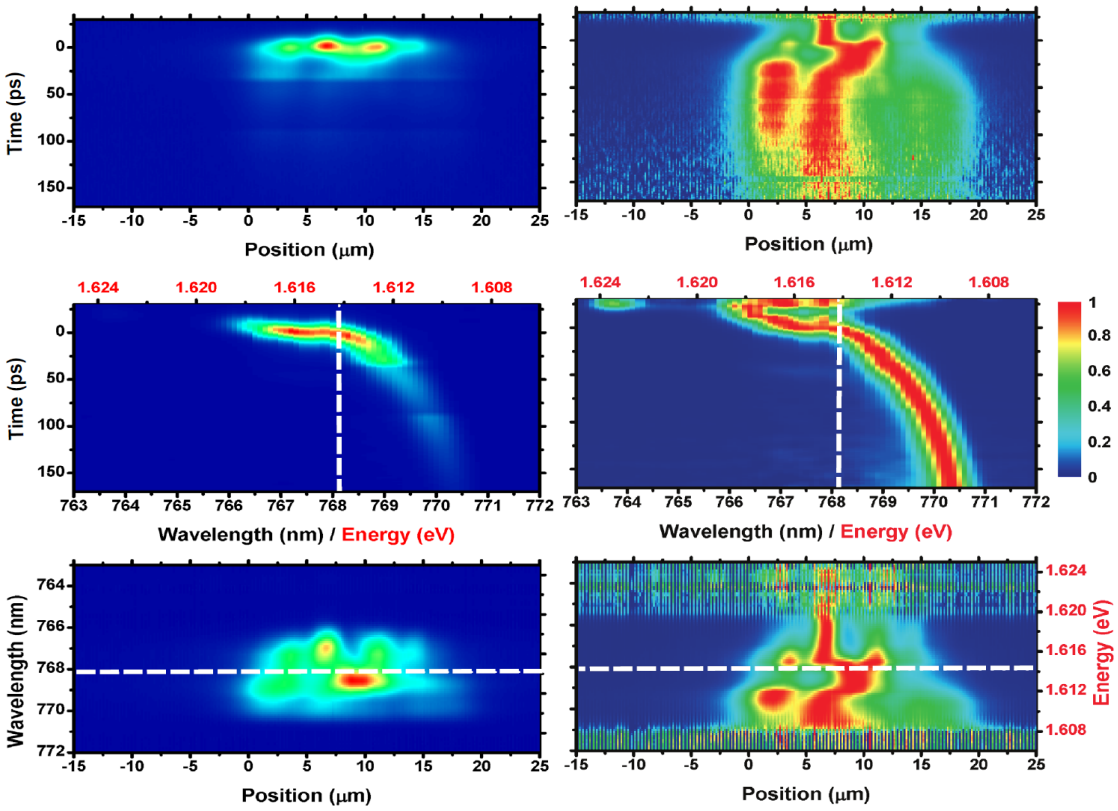

Figure 5-12: Nonnormalized (left) and normalized (right) polariton emission pattern showing the spatially, spectrally, and time-resolved dynamics under nonresonant excitation with a pumping power of 30 mW. The system is here at the crossover between the strong coupling and weak coupling regime. The emission pattern is integrated over all energies (upper panels), all positions (middle panels), or all times (bottom panels). The dashed white line represents the energy of the bare cavity.

drastically. With time the carrier density decreases and the system enters the strong coupling regime again. Now the formed polaritons will experience an altered potential. Spatially the emission occurs at the highest pump intensity which differs from what is expected in the strong coupling regime. In contrast to the results at weaker excitation densities a spatial separation between the region of highest pump power and the largest degree of depletion does not take place. This is a result from the effect that stimulated emission strongly depletes the carrier reservoir at the spatial position of the highest pump intensity. Furthermore, it should be noted that the largest condensate population at later times (where the strong coupling is reached again), is observed at the spatial position where lasing took place before. This seems quite contradictory as the carrier reservoir is strongly depleted at that region, but it is a direct consequence of polariton population and exciton-reservoir separation. While the reservoir has been depleted at these positions during the transition into the weak coupling, local potential minima are formed in these regions. As a result, the polaritons move there and get trapped in these holes.

Finally, the spatial dynamics of a system being clearly in the weak coupling

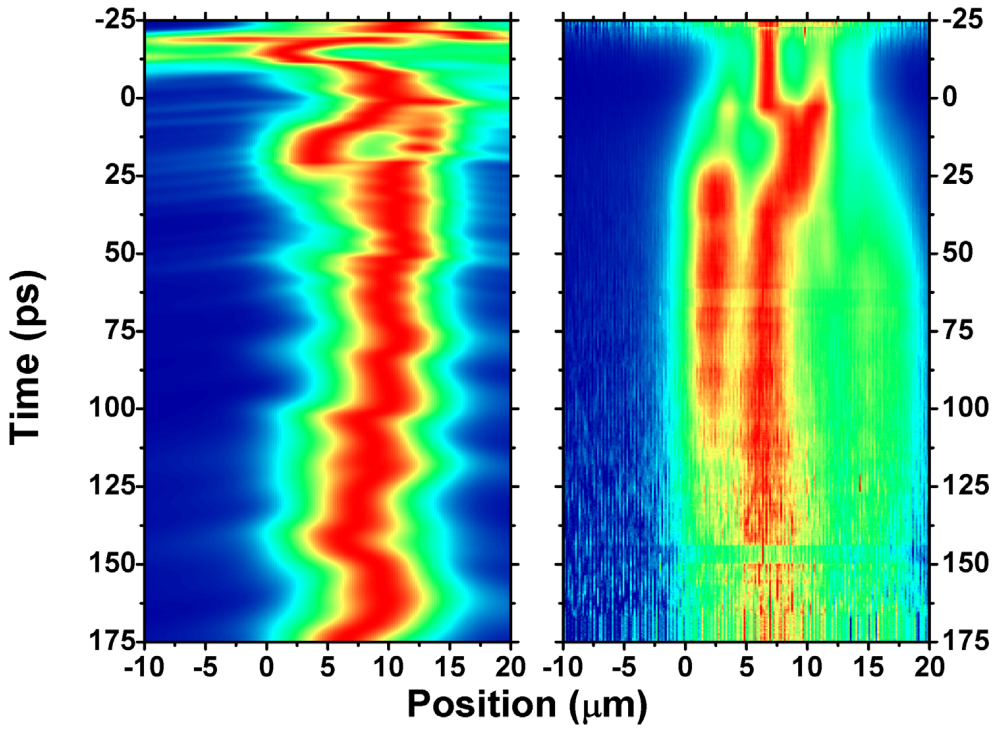

Figure 5-13: Comparison of simulated (left panel) and measured (right panel) normalized spatially and time-resolved emission for excitation significantly above the condensation threshold (30 mW excitation power).

regime shall be investigated. For this purpose, the excitation power is increased to 70 mW and the experimental data are analyzed as before, as can be seen in Fig. 5-14. The normalized data version is shown in the right panels of Fig. 5-14. The emission at early times and therefore still with photon lasing character occurs at different positions from different energies. So a single energy state is not built up. Instead, a collection of several spots is observed when the system is still in the weak coupling regime. After about 50 ps the system changes into the strong coupling regime, since the emission energetically stems from below of the bare cavity mode. In real-space the main emission is observed at both ends of the pump spot and very rarely emission comes from the spot center. Another feature occurring at this excitation density is that there is also emission coming from regions beyond the end of the pump spot best seen in the lowest panels of Fig. 5-14. Since the simulations do not consider the transition into the weak coupling regime and, therefore, also not the consequences on the potential, the experimental data deviate strongly from the simulations, as can be seen in Fig. 5-15. Thus, it is not possible to explain the features seen in the experimental data from that theoretical point of view. Two explanations for the occurrence of emission at both ends and beyond the pump spot are possible. On the one hand, depletion of the carrier reservoir could be strongest at both ends. This would lead to an antitrapping potential at the center

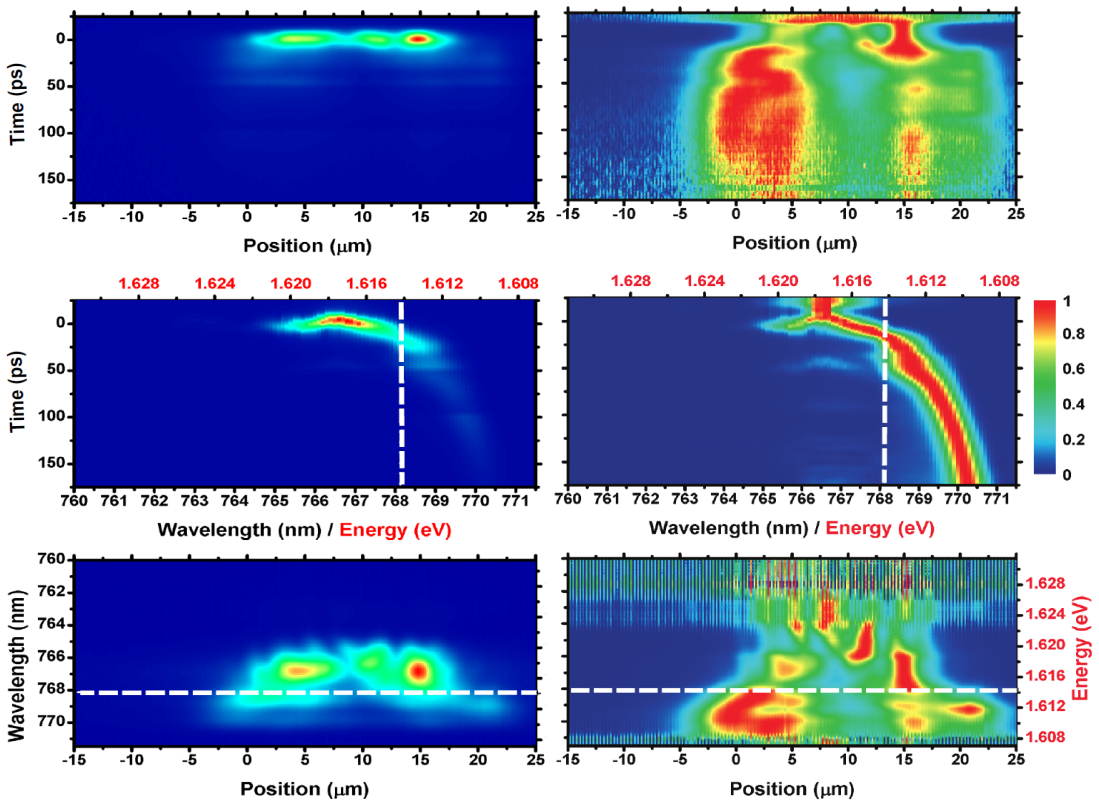

Figure 5-14: Nonnormalized (left) and normalized (right) polariton emission pattern showing the spatially, spectrally, and time-resolved dynamics under nonresonant excitation with a pumping power of 70 mW. Here, the system is in the weak coupling regime above the transition to photon lasing emission. The emission pattern is integrated over all energies (upper panels), all positions (middle panels), or all times (bottom panels). The dotted white line represents the energy of the bare cavity.

of the pump spot. As a consequence, the polaritons accelerate towards the ends of the pump spot as soon as the strong coupling regime is reached again. For a realistic scenario the potential must be quite steep. On the other hand, also the opposite case is thinkable. If at the center of the spot the depletion of the reservoir is the strongest, the build-up of two condensates at both ends would be the result. The required potential landscape has to be rather shallow, so that it is possible to prevent the polaritons from crossing over between the two condensates. This landscape can be reached by a staircase potential or polariton disorder, which is in the order of 100 μeV in this sample.

To reassure that the emission coming from energies above the bare cavity mode has photon lasing character and the one coming from lower energies can be attributed to strong coupling, the maximum blueshift relative to the LP mode is plotted against time. As can be seen in Fig. 5-16, at the two higher excitation powers a biexponential decrease takes place, being visible in the blueshifts in time. However, at low excitation power the evolution has a single exponential nature. The decay constant in the lasing regime has a value of $\tau_l \approx 40$ ps, whereas the decay in the polariton regime is much slower with $\tau_p \approx 145$ ps. This observation

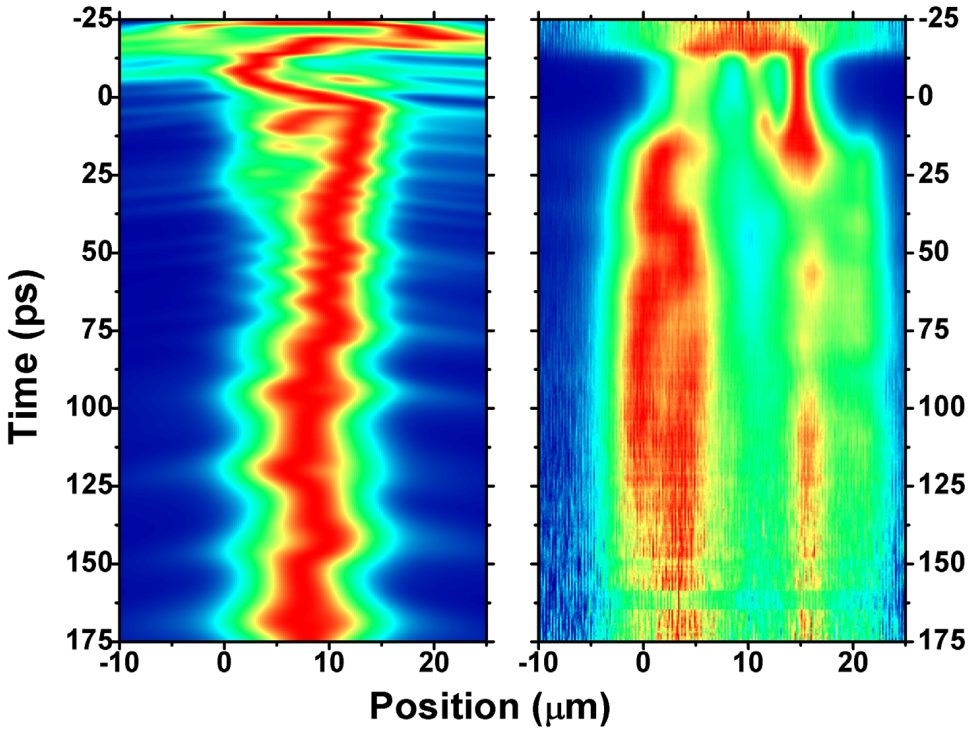

Figure 5-15: Comparison of simulated (left panel) and measured (right panel) normalized spatially and time-resolved emission for excitation far above threshold to photon lasing (70 mW excitation power). The influence of lasing is so strong that the numerical model is not adequate to describe the results.

is quite reasonable, since free carriers can couple directly to the light field in the photon lasing regime in contrast to the carriers in the polariton lasing regime, where they have to form polaritons and relax towards the bottom of the polariton branch first. The marked crossover between photon and polariton lasing does not appear at the exact bare cavity energy, but roughly 1 meV below. This is reasonable since the transition between the two regimes is a gradual one and, therefore, photon and polariton lasing may also coexist. Thus, it is possible to refer the biexponential shape of the blueshift decrease to a crossover between the weak and strong coupling regime.

5.3 Conclusion

In this chapter the emission of a polariton system under nonresonant, pulsed excitation with a staircase-shaped pump spot was investigated.

In the first section it was shown that in the polariton lasing regime discrete steps occur in momentum space. The position of these steps can be influenced by changing the local excitation density. Thus, it is possible to control the polariton

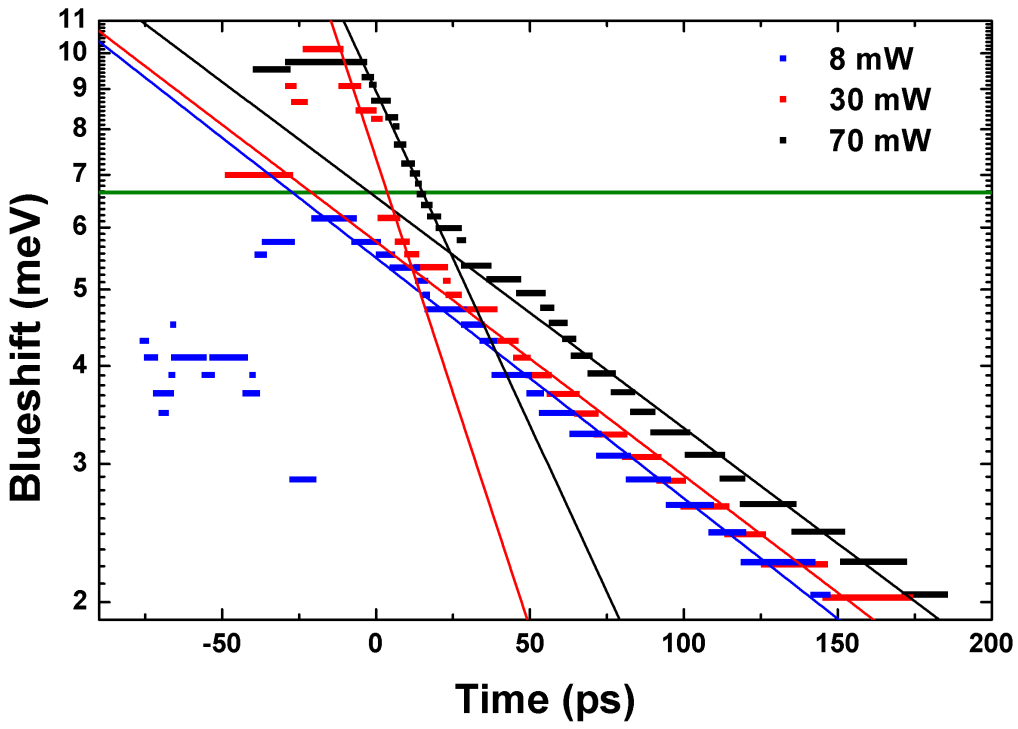

Figure 5-16: Blueshift of main emission peak versus time. The curves at the higher excitation power show a biexponential behavior with a fast component indicating photon lasing and a slower component representing polariton lasing. The crossover takes place close to the bare cavity energy (shown as a green solid line). At the lowest excitation power only the slow component is present.

flow all-optically, once the system undergoes condensation.

In the second section the spatial and temporal dynamics of a polariton condensate were demonstrated. The occurring redistribution of polaritons in the polariton lasing regime along with a fast relocation as the polariton density increases is supported by numerical simulations based on the GPE. As soon as photon lasing effects are observed spatial hole burning arises, which leads to polariton trapping. Furthermore, it was shown that the transition from the strong into the weak coupling is revealed by the biexponential behavior of the blueshift.

Chapter 6

Steady-State Condensate Perturbed by Short Laser Pulses

In the last years special attention has been paid to the phenomenon of superfluidity in semiconductor microcavities, which is a result of the partially excitonic character of the polaritons. When reaching the conditions for polaritons to undergo condensation, a macroscopic state with common phase and collective fluid behavior is established. Polaritons are then able to flow without friction. This behavior is a key feature of superfluidity. Due to the nonequilibrium character of a polariton condensate, the occurring features differ from that observed for superfluidity of liquid helium [98, 99] and cold-atom systems [100].

Various experimental configurations are possible to explore the field of superfluidity for exciton-polaritons in semiconductor microcavities. One of the earliest studies on the collective dynamics in a polariton gas has been performed in the so-called OPO (optical parametric oscillation) configuration [71]. In this case, the microcavity is resonantly excited at the LP branch and the excitation angle is chosen in such a way that the wave vector $\boldsymbol{k}_\mathrm{p}$ (pump) lies in the region of the inflection point of the LP branch. Due to polariton-polariton interactions, scattering to modes with wave vectors $\boldsymbol{k}_\mathrm{s}$ (signal) and $\boldsymbol{k}_\mathrm{i}$ (idler) takes place under conservation of momentum ($2\boldsymbol{k}_\mathrm{p} = \boldsymbol{k}_\mathrm{s} + \boldsymbol{k}_\mathrm{i}$) and energy ($2\hbar\omega_\mathrm{p} = \hbar\omega_\mathrm{s} + \hbar\omega_\mathrm{i}$). While at low pumping intensities the photoluminescence of these modes is still incoherent, stimulated-coherent scattering processes set in as soon as the pump intensity exceeds a threshold value. Then the system is in the OPO regime. Several experimental studies have exploited the OPO regime for polaritons in recent years [101, 102, 103]. Hereby, superfluidity features of the polariton condensate have been shown, e.g. the nondissipative flow around a defect in this regime [72] or the generation and manipulation of quantized vortices [104].

Adding a further weak pulsed beam (probe) to the OPO configuration, either close to the signal or idler state, this probe gets amplified. The regime of optical parametric amplification is reached [105]. Using the pulsed laser as a trigger the observation of a propagating polariton fluid at ultra high speed is achievable [71].

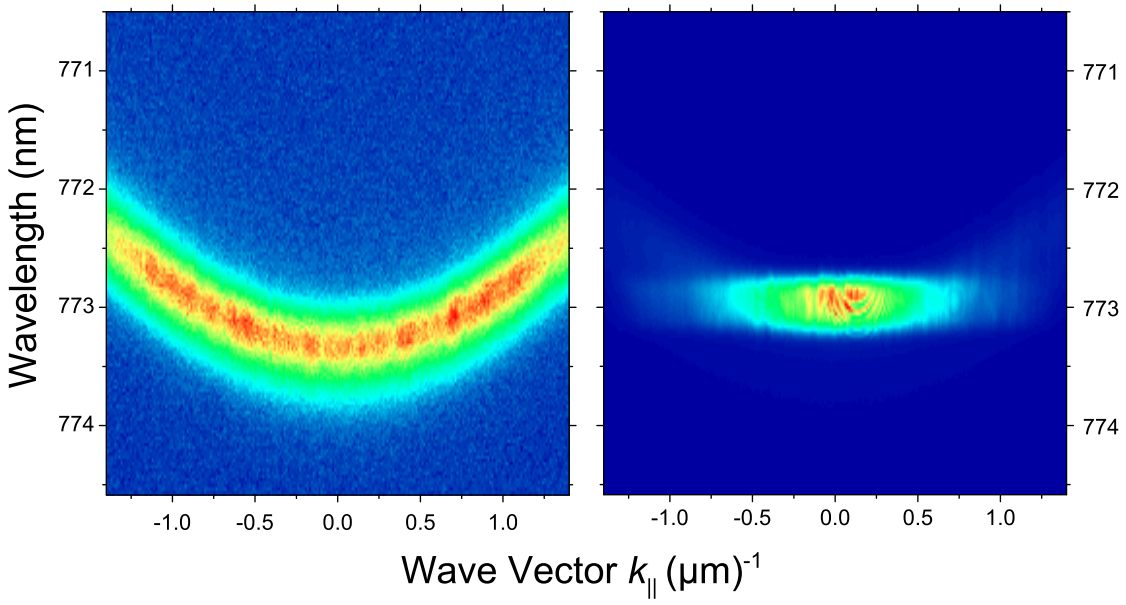

Figure 6-1: Dispersion relations for two different excitation powers of the CW laser ((a)$P_{\mathrm{exc}} = 120$ mW and (b) $P_{\mathrm{exc}} = 475$ mW). Panel (a) gives the dispersion of the lower polariton below and panel (b) the LP dispersion above the threshold of polariton condensation.

While the response to an external perturbation has been experimentally studied in detail under resonant excitation, this is still missing for polariton systems under nonresonant conditions.

In this chapter results of time-resolved far-field measurements are presented, where a continuously and resonantly pumped polariton condensate is disturbed by short nonresonant laser pulses.

6.1 Time-Resolved Two-Beam Measurements

In this section experimental results of a perturbed polariton condensate are presented. The continuous-wave (CW) laser light is focused onto the sample under an angle of 45° from normal incidence. With an excitation wavelength of 770.2 nm the lower polariton branch is excited resonantly and the regime of polariton lasing can be achieved. By use of a second nonresonant laser pulse the polariton BEC is perturbed. The resonant CW laser has a spot diameter of approximately 20 µm whereas the nonresonant pulsed laser has a smaller one with roughly 10 µm. By changing the power of the pulsed laser the strength of this perturbation can be varied. This dependence will be treated in the following. The general setup for these measurements is described in Sec. 3.3 and 3.5. For the purpose of performing time-resolved measurements, the Fourier plane of the cavity emission is imaged onto the entrance slit of the streak camera. The slit of the streak camera effectively cuts out a line along k_x at $k_y = 0$. In order to resolve the emission spectrally, a

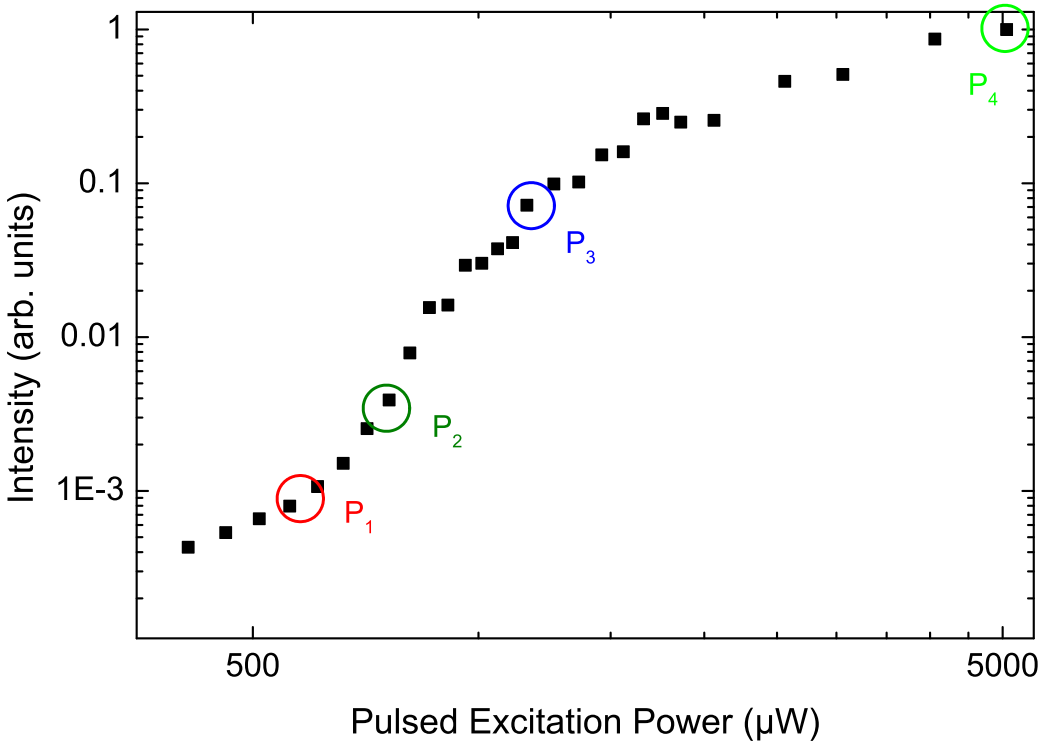

Figure 6-2: Input-output-curve of the pulsed excitation with four marked pump powers ($P_1 = 600$ μW, $P_2 = 800$ μW, $P_3 = 1300$ μW and $P_4 = 5000$ μW), which are used for the time-resolved measurements in Fig. 6-3 and 6-4.

liquid-crystal tunable filter with a resolution of about 0.75 nm is used. The microcavity, kept at cryogenic temperature, is excited at slightly negative detuning. Moreover, dispersion measurements are done to assure that the system is in the polariton lasing regime. In reference to Fig. 6-1, it means that the system is in the polariton lasing regime for excitation powers of $P_{\mathrm{CW}} = 475$ mW.

Fig. 6-2 presents the input-output-curve (i/o-curve) of the pulsed nonresonant excitation resulting from spectrally resolved measurements. The four circles indicate the excitation powers used for the time-resolved two-beam measurements. It visualizes which regime is reached with the pulsed laser. Performing several measurements with varying excitation power it is possible to examine whether the perturbation strength has any impact on the condensate or if the response of the condensate just depends on the presence of the perturbation.

For the time-resolved measurements the excitation power of the resonant CW laser is kept at 480 mW, so that the system creates a stable polariton condensate. In a second step, the nonresonant probe laser is added and measurements are carried out at the four different perturbation strengths indicated in Fig. 6-2. The top panel in Fig. 6-3 shows the results for the lowest excitation power of the pulsed laser (600 μW). In (a) the time-resolved emission pattern for the CW excitation is presented, while panel (b) demonstrates the emission pattern for the pulsed excitation. The origin of the time axis corresponds to the time of

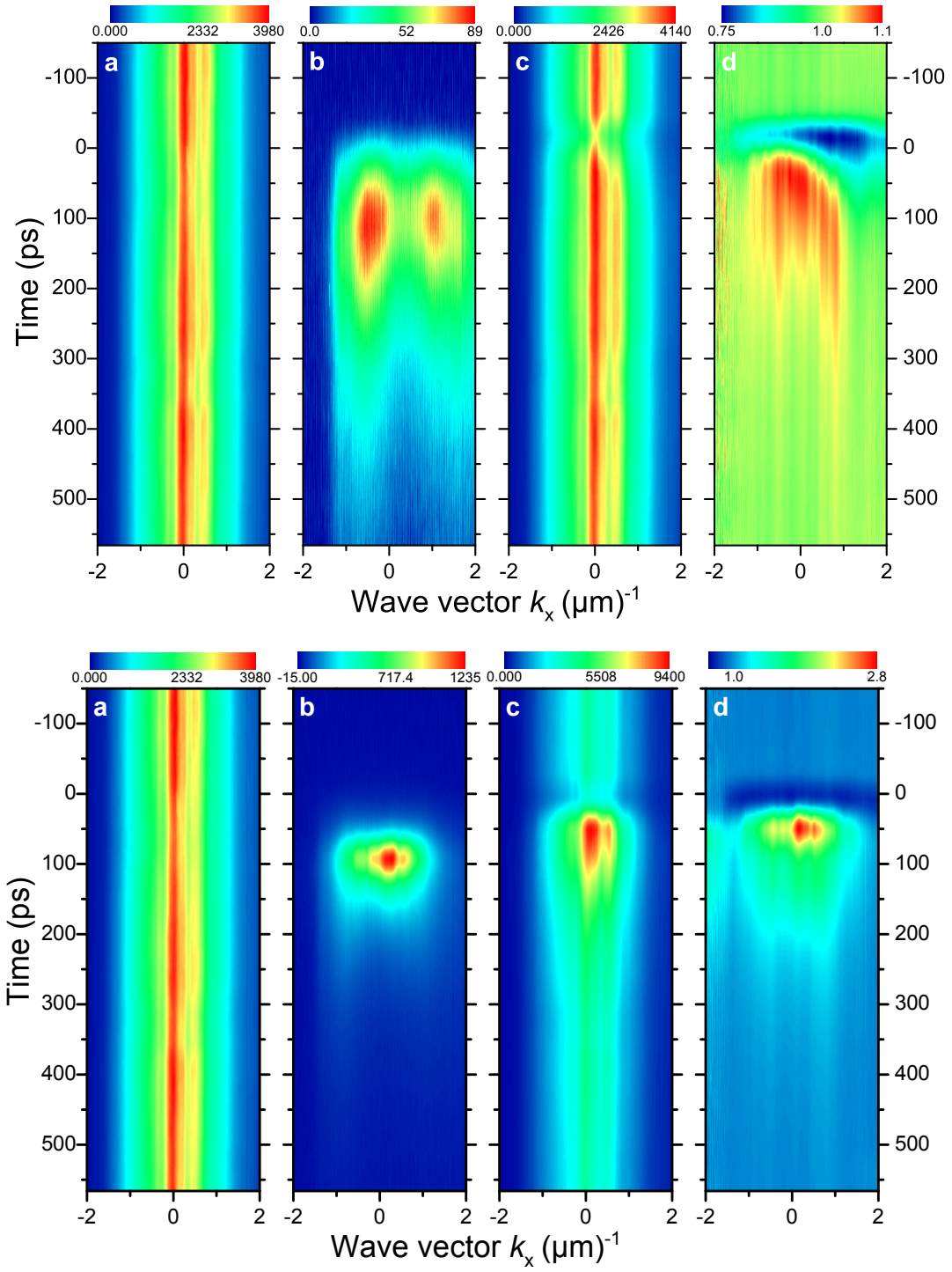

Figure 6-3: Time-resolved PL in dependence on the in-plane wave vector k_x for different excitation conditions. Top (bottom) panels show results for an excitation power of 600 μW (800 μW) of the nonresonant pulsed laser. Panel (a) shows the time-resolved PL of a polariton condensate under resonant CW excitation only. Panel (b) demonstrates polariton emission under nonresonant pulsed excitation. Panel (c) shows the results of applying both laser beams simultaneously. Here, the steady-state condensate created by CW excitation is disturbed by the short additional nonresonant laser pulse of about 2 ps. Panel (d) gives the relative total condensate population change by dividing the emission pattern of panel (c) by the sum of panel (a) and panel (b). The condensate population decreases right after the impact of the pulse. Note the different color scales in the emission pattern.

incidence of the excitation pulse with 2 ps width. Note, the emission patterns have different intensity scales, the colors are not adapted between each other. Panel (c) shows the results of applying both laser beams simultaneously. Under this excitation condition, the emission is clearly dominated by the CW excitation. Nevertheless, at the impact of the laser pulse a small decrease in the intensity can be observed. This intensity reduction is more obvious in the change of the total condensate population. In order to illustrate this parameter the intensity distribution in time and momentum-space of the emission pattern from (c) is divided by the sum of the intensity distribution of the pattern from (a) and (b) ($I_{\mathrm{CW+Pulsed}}/(I_{\mathrm{CW}} + I_{\mathrm{Pulsed}})$). An intensity value of 1 corresponds to an unchanged polariton condensate population, whereas a value below (above) 1 represents a reduction (increase) in the population induced by the nonresonant laser pulse. As shown in Fig. 6-3(d), the impact of the pulse leads to a reduction of the condensate population, and an increase tens of picoseconds after the impact.

As already discussed in Sec. 2.2.5, under nonresonant excitation the spatial shape of the pump spot defines a repulsive potential which acts on the polaritons. Here, the additional nonresonant pulsed laser leads to the formation of a Gaussian-shaped potential, which forces the polaritons of the condensate to flow away from $\mathbf{k}_x = 0$. As demonstrated in Fig. 6-3(b), the polaritons are redistributed towards higher wave vectors, which is observable in the reduction of the condensate population around $\mathbf{k}_x = 0$. After a few picoseconds, the condensate population increases again by 35% and therefore the additional pulsed excitation leads to a 35% gain of the population when compared to the sum of pulsed and continuous pumping. Thus, the polaritons created by nonresonant excitation relax and contribute to the already existing condensate resulting in an enhancement of the occupation of the lower momentum polariton states.

As a next step, let us consider the influence of the pulsed laser on the polariton condensate population when the excitation power of the pulsed laser is increased to 800 μW, bottom panels in Fig. 6-3. At this power, the regime of polariton lasing is reached, as can be seen in Fig. 6-2. A further evidence for this regime is the temporal shortening of the detected polariton emission presented in panel (b). The emission pattern in (c), showing the results of measurements with both pump sources, indicates that the temporal evolution of the intensity is dominated by the pulsed contribution. This is in strong contrast to the behavior resulting from lower power excitation. Nevertheless, in the emission pattern of the relative total condensate population change, shown in (d), the same phenomenon can be observed as before. At the time of the pulse impact the intensity decreases, followed by a population increase tens of picoseconds later. Compared to the increase seen for 600 μW pulsed excitation, the intensity rise is significantly larger. The effect of polaritons flowing away to higher momenta is still present, but since the nonresonant pulsed laser is right at the point of the highest nonlinearity (visible in the i/o-curve in Fig. 6-2), the enhancement due to the pulsed beam is even higher than for the excitation power presented before. The disappearance of the polariton population is quite uniform throughout the momentum space whereas the gain of

intensity is centered around zero. The observed gain has a similar distribution compared to the intensity of the pulsed excitation only. This behavior changes when the pump power is further raised to 1300 µW (top panels in Fig. 6-4). Even though the effect of population extinction is similar as well as its following increase, the intensity distribution in momentum space is now unsettled with an intensity gain peak around $\boldsymbol{k}_x = 0$ for early times and two side peaks occurring later with less intensity.

Finally, the pump power of the pulsed laser is increased so far (Fig. 6-4, bottom panels) that the strong coupling is lost and the system is in the weak coupling regime where photon lasing is expected. As seen in Fig. 6-2, it is not definitely clear whether a second threshold, indicating the transition from polariton towards photon lasing, does occur. The expected two-threshold behavior as an evidence for a transfer from thermal polariton emission to polariton lasing and ending with photon lasing is presented in the publication of Tempel et al. [73]. The i/o-curves of these measurements show a saturation behavior after the first threshold with a build-up of an intensity plateau right before the second threshold. This plateau is also observable in Fig. 6-2, so that the second threshold might be at relatively high excitation powers in the case at hand. A further hint for photon lasing instead of polariton lasing for the excitation power at hand is the immediate intensity increase after the impact of the pulse. Since no relaxation of the carriers to the ground state of the LP branch is needed to observe emission in the weak coupling regime, there is no time lag between excitation and emission. Having a look at the relative total population change presented in Fig. 6-4 (d), a clearly different behavior in comparison to the former results is observed. Instead of an intensity decrease with the impact of the pulse an increase with a double peak feature is observable. Only after about 50 ps a weak intensity dip is recognizable centered around $\boldsymbol{k}_x = 0$. It is followed by a second increase, which is also centered around zero momentum, and a maximum after about 300 ps. Due to the additional high excitation power of the pulsed laser the gain of the streak camera had to be lowered to prevent damage to the phosphor screen. This leads to a high artificial background, which is especially visible for times when the pulse has not excited the sample yet. Hence, the observed increase of the intensity shortly before the impact represents an artifact caused by the background. The reason for the double-peak-shaped emission at the time of the pulse impact is not clear since the nonresonant excitation beam leads to photon lasing, which cannot cause an enhancement of the polariton condensate population. But it might be possible that the regime of weak-coupling is not reached at the more weakly illuminated spot edges and, therefore, a creation of polaritons still takes place. The nonresonant excitation with a small spot diameter leads to a repulsive potential, which forces the condensed polaritons to gather higher momentum. But in contrast to the results at lower excitation powers, the repulsive potential is not as steep since the exciton reservoir density is quite small. This is due to the fact that in the main part of the spot the weak coupling regime is already reached. Hence, the condensed polaritons do not flow to as high momentum states as before and the redistribution is visible in the double-

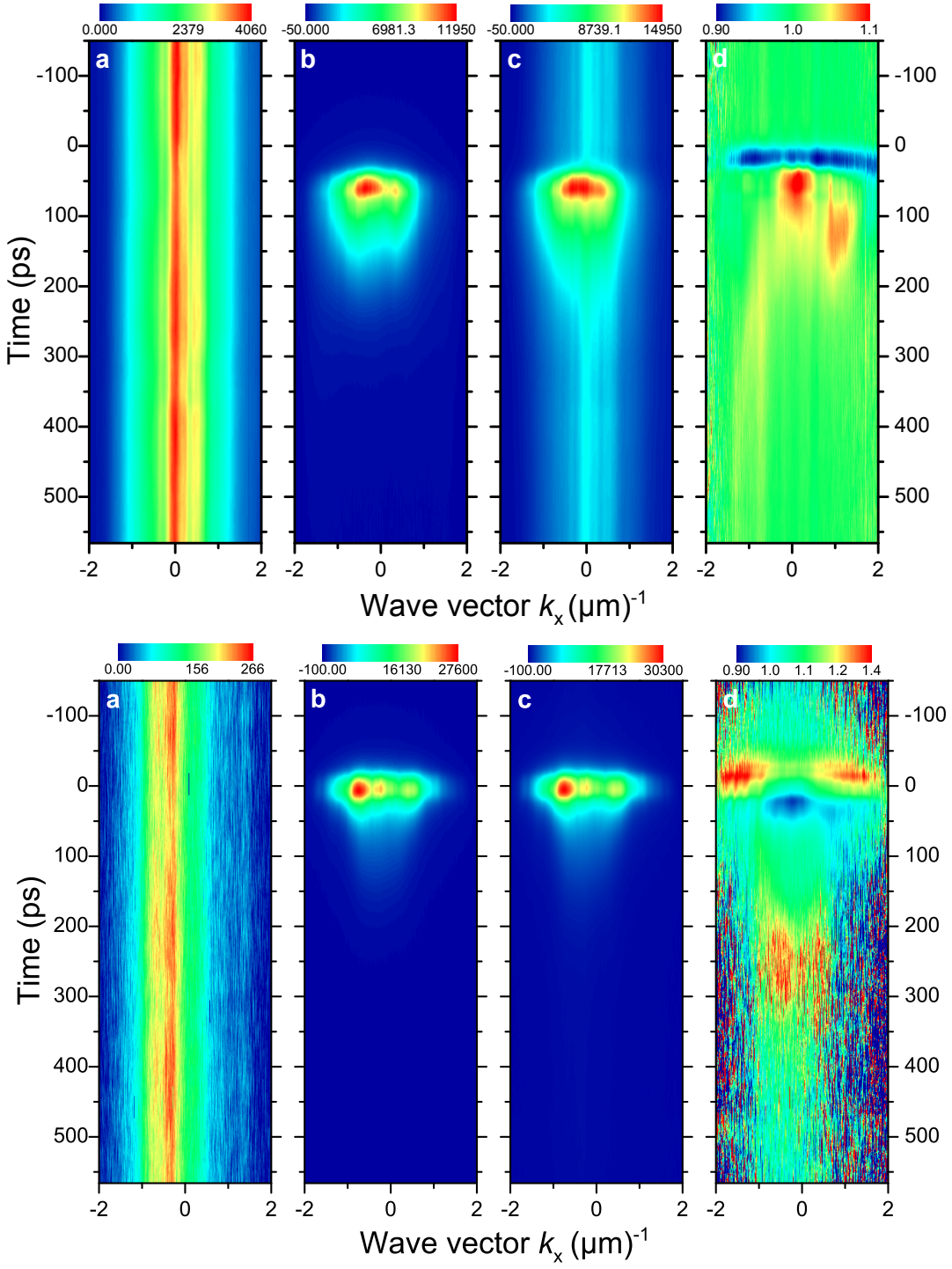

Figure 6-4: Time-resolved PL in dependence on the in-plane wave vector k_x for different excitation conditions. Top (bottom) panels show results for an excitation power of 1300 µW (5000 µW) of the nonresonant pulsed laser. Panel (a) shows the time-resolved PL of a polariton condensate under resonant CW excitation only. Panel (b) demonstrates polariton emission under nonresonant pulsed excitation. Panel (c) shows the results of applying both laser beams simultaneously. Here, the steady-state condensate due to CW excitation is disturbed by the short additional nonresonant laser pulse of about 2 ps. Panel (d) gives the relative total condensate population change by dividing the emission pattern of panel (c) with the sum of panel (a) and panel (b). The condensate population decreases right after the impact of the pulse. Note the different color scales in the emission pattern.

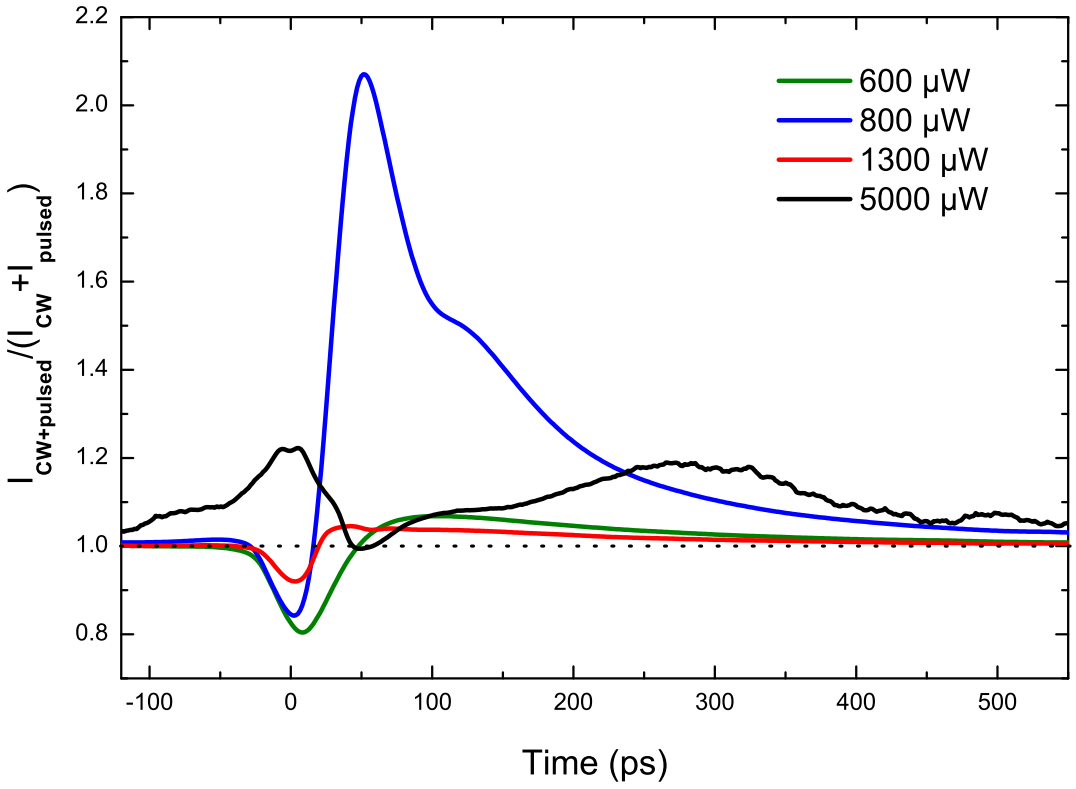

Figure 6-5: Relative total emission change for four different perturbation strengths. Weak perturbations of the condensate lead to a decrease of the population immediately after the impact of the pulse with an increase afterwards. In the case of very strong perturbation, the intensity increases directly with the impact. The dotted line represents the region of no condensate population change.

peak-shapes emission. The increase at later times can be explained by reaching the strong coupling regime again as soon as the exciton density in the QWs is low enough that the excitons and photons can couple strongly. The additional polaritons can contribute to the condensate again and enhance the emission.

To analyze the results in more detail the integrated intensity of the time-resolved measurements ($I_{\mathrm{CW+Pulsed}}/(I_{\mathrm{CW}} + I_{\mathrm{Pulsed}})$) is plotted against time for different powers of the pulsed laser in Fig. 6-5. Striking in this illustration is the simultaneously occurring dip with the impact of the pulse for the three lowest pumping powers, while the curve shows the opposite behavior for the highest pumping powers; an intensity increase instead of a decrease. And exactly at the time where the intensity raises again for the other excitation powers, the expected decrease appears. Since the intensity value at the dip does not fall significantly below one, the condensate population is not reduced due to the additional pulsed excitation as it is the case for lower pump powers. Likewise noticeable is the strong intensity gain for pulsed excitation at 800 µW. Comparison to the curves for the other perturbation strengths shows, that the occurring enhancement is largest at

this excitation power, reaching a maximum value of about two. This fact underlines the theory that the most powerful enhancement takes place at the position of the strongest nonlinearity of the pulsed i/o-curve as depicted in Fig. 6-2.

6.2 Conclusion

In the last section, results of time-resolved momentum measurements in a two-beam experiment were presented. A polariton condensate is created via resonant continuous-wave excitation and perturbed by a nonresonant short laser pulse. The results show a strong dependence on the perturbation strength: for nonresonant excitation powers in the strong coupling regime a polariton flow away from small momenta towards higher wave numbers is noticeable. After relaxation the polaritons from nonresonant excitation enhance the emission. For nonresonant excitation powers in the weak coupling regime a weaker polariton redistribution at the impact of the pulse is observable.

Moreover, for further investigations it would be interesting to perform real-space time-resolved measurements to be able to follow the polariton flow. Secondly it would be possible to vary also the excitation power of the resonant continuous-wave laser. What happens for excitation powers below the threshold of polariton condensation and for excitation powers slightly below the threshold to photon lasing?

Chapter 7

Summary and Outlook

In this thesis, the formation of an exciton-polariton condensate in a semiconductor microcavity was studied with an emphasis on all-optical methods to influence and control the properties of the polariton condensate. The experimental methods range from excitation spot shaping using a spatial-light-modulator to the perturbation of a polariton condensate with a nonresonant, pulsed laser beam.

At first, the relaxation dynamics in an optically created polariton wire were examined. With a wire-shaped excitation spot, created with a spatial-light-modulator, the polaritons are gain-trapped to a length of 15 µm and a width of 2 µm. The results of spatially and time-resolved measurements show an emission dynamics originating from the wire center at earlier times and developing towards both ends of the wire later on. While the emission has a relatively short lifetime at the center it turns into a longer living emission at both ends. Due to spectrally resolved results it is possible to characterize the different emission regimes in terms of photon and polariton lasing.

Hence, an analysis of the decay dynamics in a polariton wire was presented showing a spatial boundary between photon lasing and polariton lasing emission. However, further studies have to be performed to fully understand the crossover from the weak to the strong coupling regime. In analogy to results presented by Kammann et al. [106], it is still an open question, whether the observed characteristics are due to population inversion or condensation in the weak coupling regime. Performing measurements also in momentum-space and with differently shaped excitation spots may help to understand the origin of the emission mechanism and its spatial pattern formation.

The second part of this thesis contained results of a stepwise homogeneously pumped polariton condensate. With a nonresonant staircase shaped excitation spot a polariton condensate with well defined momentum states was created. By adjusting the local excitation density the position of these momentum states can be tuned. In addition, an analysis of the spatial dynamics under such pumping conditions was presented. Results of spatially, spectrally and temporally resolved emission show a redistribution of the polaritons in the regime of polariton lasing

followed by a relocation of the intensity maximum as the polariton density decreases. Numerical simulations support the observed redistribution dynamics in the polariton lasing regime. At higher excitation power the system reaches the weak coupling regime and spatial hole burning leads to trapped polaritons. The temporal dependence of the blueshift demonstrates in its biexponential behavior the crossover between the weak and the strong coupling regime.

The results demonstrate an all-optical method to prepare a polariton condensate in an adjustable momentum state. However, the realization of polaritonic circuits with this approach requires further scientific research. Due to the strong dependence of the polariton properties on the cavity-exciton detuning, it might be desirable to examine the optical momentum state control and the spatial dynamics of a stepwise pumped polariton condensate also at other detunings. Further geometrical changes of the excitation spot might give a more detailed insight into the control of the polariton flow. From an application point of view, a transfer to other materials, which show polariton propagation at room temperature [107], could be very helpful for the realization of optical circuits.

The third part of this thesis demonstrated the impact of a nonresonant laser pulse on a steady state polariton condensate. Results, obtained from time-resolved measurements, show a strong dependence on the strength of the perturbation. With excitation powers, where the system is in the strong coupling regime, a polariton flow towards higher momenta is observed simultaneously with the impact of the pulse. Afterwards an enhancement of the emission occurs with its highest value at the point of the strongest nonlinearity of the pulsed excitation. This behavior changes when the excitation power of the pulsed laser is such that the weak coupling regime is reached. Here, a weaker polariton redistribution with the impact of the pulse is visible.

For a deeper understanding of the relation between polariton flow and perturbation strength further experimental research is needed. For example, real-space measurements could give further information about the polariton flow such as its spatial dynamics. Moreover, it would be worthwhile to study the influence of an external pulsed perturbation on a polariton condensate created by differently shaped excitation geometries.

Bibliography

[1] H. H. Hopkins and N. S. Kapany, "A flexible fibrescope, using static scanning," *Nature*, vol. 173, pp. 39–41, 1954.

[2] E. Snitzer, "Cylindrical dielectric waveguide modes," *J. Opt. Soc. Am.*, vol. 51, no. 51, pp. 491–498, 1961.

[3] K. Kao and G. Hockham, "Dielectric-fibre surface waveguides for optical frequencies," *Proc. IEE*, vol. 113, no. 7, pp. 1151–1158, 1966.

[4] N. Zheludev, "The life and times of the led – a 100-year history," *Nat. Photonics*, vol. 1, pp. 189–192, 2007.

[5] K. D. Choquette and H. Q. Hou, "Vertical-cavity surface emitting lasers: Moving from research to manufacturing," *Proc. IEEE*, vol. 85, no. 11, pp. 1730–739, 1997.

[6] D. Qian, M.-F. Huang, E. Ip, Y.-K. Huang, Y. Shao, J. Hu, and T. Wang, "101.7-tb/s (370x294-gb/s) PDM-128QAM-OFDM transmission over 3x55-km SSMF using pilot-based phase noise mitigation," in *Optical Fiber Communication Conference/National Fiber Optic Engineers Conference 2011*, p. PDPB5, Optical Society of America, 2011.

[7] F. Poletti, N. V. Wheeler, M. N. Petrovich, N. Baddela, E. N. Fokoua, J. R. Hayes, D. R. Gray, R. S. Z. Li, and D. J. Richardson, "Towards high-capacity fibre-optic communications at the speed of light in vacuum," *Nat. Photonics*, vol. 7, pp. 279–284, 2013.

[8] H. J. Caulfield and S. Dolev, "Why future supercomputing requires optics," *Nature Photonics*, vol. 4, p. 261, 2010.

[9] T. Volz, A. Reinhard, M. Winger, A. Badolato, K. J. Hennessy, E. L. Hu, and A. Imamoglu, "Ultrafast all-optical switching by single photons," *Nat. Photonics*, vol. 6, pp. 605–609, 2012.

[10] J. I. Saari, M. M. Krause, B. R. Walsh, and P. Kambhampati, "Terahertz bandwidth all-optical modulation and logic using multiexcitons in semiconductor nanocrystals," *Nano Letters*, vol. 13, no. 2, pp. 722–727, 2013.

[11] V. R. Almeida, C. A. Barrios, R. R. Panepucci, and M. Lipson, "All-optical control of light on a silicon chip," *Nature*, vol. 431, pp. 1081–1084, 2004.

[12] D. A. B. Miller, "Are optical transistors the logical next step?," *Nature Photonics*, vol. 4, 2010.

[13] C. Weisbuch, M. Nishioka, A. Ishikawa, and Y. Arakawa, "Observation of the coupled exciton-photon mode splitting in a semiconductor quantum microcavity," *Phys. Rev. Lett.*, vol. 69, no. 23, p. 3314, 1992.

[14] V. Savona, L. C. Andreani, P. Schwendimann, and A. Quattropani, "Quantum well excitons in semiconductor microcavities: Unified treatment of weak and strong coupling regimes," *Solid State Commun.*, vol. 93, no. 9, pp. 733–739, 1995.

[15] M. H. Anderson, J. R. Ensher, M. R. Matthews, C. E. Wieman, and E. A. Cornell, "Observation of bose-einstein condensation in a dilute atomic vapor," *Science*, vol. 269, no. 5221, pp. 198–201, 1995.

[16] K. B. Davis, M.-O. Mewes, M. R. Andrews, N. J. van Druten, D. S. Durfee, D. M. Kurn, and W. Ketterle, "Bose-Einstein condensation in a gas of sodium atoms," *Phys. Rev. Lett.*, vol. 75, no. 22, p. 3969, 1995.

[17] J. Kasprzak, M. Richard, S. Kundermann, A. Baas, P. Jeambrun, J. M. Keeling, F. Marchetti, M. Szymańska, R. André, J. Staehli, V. Savona, P. B. Littlewood, B. Deveaud, and L. S. Dang, "Bose-einstein condensation of exciton polaritons," *Nature*, vol. 443, p. 409, 2006.

[18] S. Christopoulos, G. Baldassarri Höger von Högersthal, A. J. D. Grundy, P. G. Lagoudakis, A. V. Kavokin, J. J. Baumberg, G. Christmann, R. Butté, E. Feltin, J.-F. Carlin, and N. Grandjean, "Room-temperature polariton lasing in semiconductor microcavities," *Phys. Rev. Lett.*, vol. 98, no. 12, p. 126405, 2007.

[19] G. Christmann, R. Butté, E. Feltin, J.-F. Carlin, and N. Grandjean, "Room temperature polariton lasing in a gan/algan multiple quantum well microcavity," *Appl. Phys. Lett.*, vol. 93, no. 051102, 2008.

[20] G. Tosi, G. Christmann, N. G. Berloff, P. Tsotsis, T. Gao, Z. Hatzopoulos, P. G. Savvidis, and J. J. Baumberg, "Sculpting oscillators with light within a nonlinear quantumfluid," *Nat. Phys.*, vol. 8, 2012.

[21] T. K. Paraïso, D. Sarchi, G. Nardin, R. Cerna, Y. Leger, B. Pietka, M. Richard, O. El Daïf, F. Morier-Genoud, V. Savona, and B. Deveaud-Plédran, "Enhancement of microcavity polariton relaxation under confinement," *Phys. Rev. B*, vol. 79, p. 045319, 2009.

[22] E. Wertz, L. Ferrier, D. D. Solnyshkov, R. Johne, D. Sanvitto, A. Lemaître, I. Sagnes, R. Grousson, A. V. Kavokin, P. Senellart, G. Malpuech, and J. Bloch, "Spontaneous formation and optical manipulation of extended polariton condensates," *Nat. Phys.*, vol. 6, no. 11, pp. 860–864, 2010.

[23] C. W. Lai, N. Y. Kim, S. Utsunomiya, G. Roumpos, H. Deng, M. D. Fraser, T. Byrnes, P. Recher, N. Kumada, T. Fujisawa, and Y. Yamamoto, "Coherent zero-state and π-state in an exciton-polariton condensate array," *Nature*, vol. 450, no. 7169, pp. 529–532, 2007.

[24] A. Amo, T. C. H. Liew, C. Adrados, R. Houdré, E. Giacobino, A. V. Kavokin, and A. Bramati, "Exciton-polariton spin switches," *Nat. Photonics*, vol. 4, no. 6, pp. 361–366, 2010.

[25] T. Gao, P. S. Eldridge, T. C. H. Liew, S. I. Tsintzos, G. Stavrinidis, G. Deligeorgis, Z. Hatzopoulos, and P. G. Savvidis, "Polariton condensate transistor switch," *Phys. Rev. B*, vol. 85, p. 235102, 2012.

[26] D. Ballarini, "All-optical polariton transistor." 2012.

[27] H. S. Nguyen, D. Vishnevsky, C. Sturm, D. Tanese, D. Solnyshkov, E. Galopin, A. Lemaître, I. Sagnes, A. Amo, G. Malpuech, and J. Bloch, "Realization of a double-barrier resonant tunneling diode for cavity polaritons," *Phys. Rev. Lett.*, vol. 110, p. 236601, 2013.

[28] V. M. Agranovich, "On the influence of reabsorption on the decay of fluorescence in molecular crystals.," *Optika i Spektroskopiya*, vol. 3, p. 84, 1957.

[29] J. J. Hopfield, "Theory of the contribution of excitons to the complex dielectric constant of crystals," *Phys. Rev.*, vol. 112, no. 5, pp. 1555–1567, 1958.

[30] C. Weisbuch and R. G. Ulbrich, "Resonant polariton fluorescence in gallium arsenide," *Phys. Rev. Lett.*, vol. 39, pp. 654–656, 1977.

[31] Klingshirn, *Semiconductor Optics*. Spinger Verlag, 1997.

[32] A. V. Kavokin, J. J. Baumberg, G. Malpuech, and F. P. Laussy, *Microcavities*. Oxford University Press, t ed., 2007.

[33] H. Deng, H. Haug, and Y. Yamamoto, "Exciton-polariton bose-einstein condensation," *Rev. Mod. Phys.*, vol. 82, no. 2, pp. 1489–1537, 2010.

[34] M. Fox, *Optical Properties of Solids*. Oxford University Press, 2001.

[35] E. Hanamura and H. Haug, "Condensation effects of excitons," *Phys. Lett. C*, vol. 33, no. 4, 1977.

[36] Gaponenko, *Introduction to Nanophotonics*. Cambridge University Press, 2010.

[37] R. L. Greene, K. K. Bajaj, and D. E. Phelps, "Energy levels of wannier excitons in GaAs/GaAlAs quantum-well structures," *Phys. Rev. B*, vol. 29, pp. 1807–1812, 1984.

[38] D. M. Whittaker, P. Kinsler, T. A. Fisher, M. S. Skolnick, A. Armitage, A. M. Afshar, M. D. Sturge, and J. S. Roberts, "Motional narrowing in semiconductor microcavities," *Phys. Rev. Lett.*, vol. 77, no. 23, pp. 4792–4795, 1996.

[39] V. M. Ustinov, A. E. Zhukov, A. Y. Egorov, and N. A. Maleev, *Quantum Dot Lasers*. Oxford University Press, 2003.

[40] K. J. Vahala, "Optical microcavities," *Nature*, vol. 424, p. 839, 2003.

[41] M. Born and E. Wolf, *Principles of Optics*. Cambridge University Press, 1959.

[42] H. Deng, *Dynamic Condensation of Semiconductor Microcavity Polaritons*. PhD thesis, Stanford University, 2006.

[43] R. Houdré, J. L. Gibernon, P. Pellandini, R. P. Stanley, U. Oesterle, C. Weisbuch, J. O'Gorman, B. Roycroft, and M. Ilegems, "Saturation of the strong-coupling regime in a semiconductor microcavity: Free-carrier bleaching of cavity polaritons," *Phys. Rev. B*, vol. 52, no. 11, p. 7810, 1995.

[44] M. Skolnick, R. Stevenson, A. Tartakovskii, R. Butté, M. Emam-Ismail, D. Whittaker, P. Savvidis, J. Baumberg, A. Lemaître, V. Astratov, and J. Roberts, "Polariton–polariton interactions and stimulated scattering in semiconductor microcavities," *Materials Science and Engineering C*, vol. 19, pp. 407–416, 2002.

[45] A. V. Kavokin and G. Malpuech, *Thin Films and nanostructures - Cavity Polaritons*, vol. 32. Elsevier, 1 ed., 2003.

[46] F. Tassone, C. Piermarocchi, V. Savona, A. Quattropani, and P. Schwendimann, "Bottleneck effects in the relaxation and photoluminescence of microcavity polaritons," *Phys. Rev. B*, vol. 56, no. 12, pp. 7554–7563, 1997.

[47] A. I. Tartakovskii, M. Emam-Ismail, R. M. Stevenson, M. S. Skolnick, V. N. Astratov, D. M. Whittaker, J. J. Baumberg, and J. S. Roberts, "Relaxation bottleneck and its suppression in semiconductor microcavities," *Phys. Rev. B*, vol. 62, no. 4, pp. R2283–R2286, 2000.

[48] M. Müller, J. Bleuse, and R. André, "Dynamics of the cavity polariton in CdTe-based semiconductor microcavities: Evidence for a relaxation edge," *Phys. Rev. B*, vol. 62, p. 16886, 2000.

[49] G. Malpuech, A. Kavokin, A. Di Carlo, and J. J. Baumberg, "Polariton lasing by exciton-electron scattering in semiconductor microcavities," *Phys. Rev. B*, vol. 65, p. 153310, 2002.

[50] F. Tassone, C. Piermarocchi, V. Savona, A. Quattropani, and P. Schwendimann, "Photoluminescence decay times in strong-coupling semiconductor microcavities," *Phys. Rev. B*, vol. 53, pp. R7642–R7645, 1996.

[51] S. Haug, H.; Schmitt-Rink, "Electron theory of the optical properties of laser-excited semiconductors," *Prog. Quant. Electr.*, vol. 9, pp. 3–100, 1984.

[52] D. Ballarini, A. Amo, L. Viña, D. Sanvitto, M. Skolnick, and J. S. Roberts, "Transition from the strong- to the weak-coupling regime in semiconductor microcavities: Polarization dependence," *Appl. Phys. Lett.*, vol. 90, no. 201905, 2007.

[53] E. M. Purcell, "Spontaneous emission probabilities at radiofrequencies," *Phys. Rev.*, vol. 69, p. 681, 1946.

[54] J. M. Gérard, B. Sermage, B. Gayral, B. Legrand, E. Costard, and V. Thierry-Mieg, "Enhanced spontaneous emission by quantum boxes in a monolithic optical microcavity," *Phys. Rev. Lett.*, vol. 81, no. 5, pp. 1110–1113, 1998.

[55] S. Reitzenstein, A. Bazhenov, A. Gorbunov, C. Hofmann, S. Münch, A. Löffler, M. Kamp, J. P. Reithmaier, V. D. Kulakovskii, and A. Forchel, "Lasing in high-Q quantum-dot micropillar cavities," *Appl. Phys. Lett.*, vol. 89, no. 5, p. 051107, 2006.

[56] M. G. A. Bernard and G. Duraffourg, "Laser conditions in semiconductors," *Phys. Status Solidi B*, vol. 1, pp. 699–703, 1961.

[57] M. Wouters, I. Carusotto, and C. Ciuti, "Spatial and spectral shape of inhomogeneous nonequilibrium exciton-polariton condensates," *Phys. Rev. B*, vol. 77, no. 11, p. 115340, 2008.

[58] W. Ketterle, "Nobel lecture: When atoms behave as waves: Bose-Einstein condensation and the atom laser," *Rev. Mod. Phys.*, vol. 74, no. 4, pp. 1131–1151, 2002.

[59] J. Annett, *Supraleitung, Suprafluidität und Kondensate*. Oldenburg Verlag, 2011.

[60] V. A. Zagrebnov and J.-B. Bru, "The bogoliubov model of weakly imperfect bose gas," *Physics Reports*, vol. 350, pp. 291–434, 2001.

[61] R. J. Glauber, "Photon correlations," *Phys. Rev. Lett.*, vol. 10, no. 3, pp. 84–86, 1963.

[62] L. P. Pitaevskii and S. Stringari, *Bose Einstein Condensation*. Oxford University Press, 2003.

[63] J. M. Kosterlitz and D. J. Thouless, "Ordering, metastability and phase transitions in two-dimensional systems," *J. Phys. C: Solid State Phys.*, vol. 6, no. 7, p. 1181, 1973.

[64] D. R. Nelson and J. M. Kosterlitz, "Universal jump in the superfluid density of two-dimensional superfluids," *Phys. Rev. Lett.*, vol. 39, pp. 1201–1205, 1977.

[65] V. Bagnato and D. Kleppner, "Bose-einstein condensation in low-dimensional traps," *Phys. Rev. A*, vol. 44, pp. 7439–7441, 1991.

[66] H. Deng, G. S. Solomon, R. Hey, K. H. Ploog, and Y. Yamamoto, "Spatial coherence of a polariton condensate," *Phys. Rev. Lett.*, vol. 99, no. 12, p. 126403, 2007.

[67] S. Utsunomiya, L. Tian, G. Roumpos, C. W. Lai, N. Kumada, T. Fujisawa, M. Kuwata-Gonokami, A. Löffler, S. Höfling, A. Forchel, and Y. Yamamoto, "Observation of bogoliubov excitations in exciton-polariton condensates," *Nat. Phys.*, vol. 4, p. 700, 2008.

[68] K. G. Lagoudakis, M. Wouters, M. Richard, A. Baas, I. Carusotto, R. Andre, L. Dang, and B. Deveaud-Pledran, "Quantized vortices in an exciton-polariton condensate," *Nat. Phys.*, vol. 4, p. 706, 2008.

[69] K. G. Lagoudakis, T. Ostatnicky, A. V. Kavokin, Y. G. Rubo, R. Andre, and B. Deveaud-Pledran, "Observation of half-quantum vortices in an exciton-polariton condensate," *Science*, vol. 326, pp. 974–976, 2009.

[70] J. J. Baumberg, A. V. Kavokin, S. Christopoulos, A. J. D. Grundy, R. Butté, G. Christmann, D. D. Solnyshkov, G. Malpuech, G. Baldassarri Höger von Högersthal, E. Feltin, J.-F. Carlin, and N. Grandjean, "Spontaneous polarization buildup in a room-temperature polariton laser," *Phys. Rev. Lett.*, vol. 101, no. 13, p. 136409, 2008.

[71] A. Amo, D. Sanvitto, F. P. Laussy, D. Ballarini, E. D. Valle, M. D. Martin, A. Lemaître, J. Bloch, D. N. Krizhanovskii, M. S. Skolnick, C. Tejedor, and L. Viña, "Collective fluid dynamics of a polariton condensate in a semiconductor microcavity," *Nature*, vol. 457, pp. 291–295, 2009.

[72] A. Amo, J. Lefrère, S. Pigeon, C. Adrados, C. Ciuti, I. Carusotto, R. Houdré, E. Giacobino, and A. Bramati, "Superfluidity of polaritons in semiconductor microcavities," *Nat. Phys.*, vol. 5, pp. 805–810, 2009.

[73] J.-S. Tempel, F. Veit, M. Aßmann, L. E. Kreilkamp, A. Rahimi-Iman, A. Löffler, S. Höfling, S. Reitzenstein, L. Worschech, A. Forchel, and M. Bayer, "Characterization of two-threshold behavior of the emission from a GaAs microcavity," *Phys. Rev. B*, vol. 85, p. 075318, 2012.

[74] P. Lugan, D. Sarchi, and V. Savona, "Theory of trapped polaritons in patterned microcavities," *phys. stat. sol. c*, vol. 7, pp. 2428–2431, 2006.

[75] M. Richard, J. Kasprzak, R. Romestain, R. André, and L. S. Dang, "Spontaneous coherent phase transition of polaritons in CdTe microcavities," *Phys. Rev. Lett.*, vol. 94, p. 187401, 2005.

[76] R. Houdré, C. Weisbuch, R. P. Stanley, U. Oesterle, P. Pellandini, and M. Ilegems, "Measurement of cavity-polariton dispersion curve from angle-resolved photoluminescence experiments," *Phys. Rev. Lett.*, vol. 73, no. 15, p. 2043, 1994.

[77] C. Kohler, T. Haist, X. Schwab, and W. Osten, "Hologram optimization for slm-based reconstruction with regard to polarization effects," *Optic Express*, vol. 16, no. 19, 2008.

[78] A. Amo, S. Pigeon, D. Sanvitto, V. G. Sala, R. Hivet, I. Carusotto, F. Pisanello, G. Lemènager, R. Houdré, E. Giacobino, C. Ciuti, and A. Bramati, "Polariton superfluids reveal quantum hydrodynamic solitons," *Science*, vol. 332, no. 6034, pp. 1167–1170, 2011.

[79] K. Paraiso, M. Wouters, Y. Léger, F. Morier-Genoud, and B. Deveaud-Plédran, "Multistability of a coherent spin ensemble in a semiconductor microcavity," *Nat. Mater.*, vol. 9, pp. 655–660, 2010.

[80] E. B. Magnusson, I. G. Savenko, and I. A. Shelykh, "Bistability phenomena in one-dimensional polariton wires," *Phys. Rev. B*, vol. 84, p. 195308, 2011.

[81] T. C. H. Liew, A. V. Kavokin, and I. A. Shelykh, "Optical circuits based on polariton neurons in semiconductor microcavities," *Phys. Rev. Lett.*, vol. 101, p. 016402, 2008.

[82] T. C. H. Liew, A. V. Kavokin, T. Ostatnický, M. Kaliteevski, I. A. Shelykh, and R. A. Abram, "Exciton-polariton integrated circuits," *Phys. Rev. B*, vol. 82, p. 033302, 2010.

[83] A. Kuther, M. Bayer, T. Gutbrod, A. Forchel, P. A. Knipp, T. L. Reinecke, and R. Werner, "Confined optical modes in photonic wires," *Phys. Rev. B*, vol. 58, pp. 15744–15748, 1998.

[84] G. Roumpos, W. H. Nitsche, S. Höfling, A. Forchel, and Y. Yamamoto, "Gain-induced trapping of microcavity exciton polariton condensates," *Phys. Rev. Lett.*, vol. 104, no. 12, p. 126403, 2010.

[85] J. Hegarty, L. Goldner, and M. D. Sturge, "Localized and delocalized two-dimensional excitons in GaAs-AlGaAs multiple-quantum-well structures," *Phys. Rev. B*, vol. 30, pp. 7346–7348, 1984.

[86] F. Manni, K. G. Lagoudakis, T. C. H. Liew, R. André, and B. Deveaud-Plédran, "Spontaneous pattern formation in a polariton condensate," *Phys. Rev. Lett.*, vol. 107, p. 106401, 2011.

[87] M. Galbiati, L. Ferrier, D. D. Solnyshkov, D. Tanese, E. Wertz, A. Amo, M. Abbarchi, P. Senellart, I. Sagnes, A. Lemaître, E. Galopin, G. Malpuech, and J. Bloch, "Polariton condensation in photonic molecules," *Phys. Rev. Lett.*, vol. 108, p. 126403, 2012.

[88] J. Szczytko, L. Kappei, J. Berney, F. Morier-Genoud, M. T. Portella-Oberli, and B. Deveaud, "Determination of the exciton formation in quantum wells from time-resolved interband luminescence," *Phys. Rev. Lett.*, vol. 93, p. 137401, Sep 2004.

[89] G. Roumpos, M. D. Fraser, A. Löffler, S. Höfling, A. Forchel, and Y. Yamamoto, "Single vortex-antivortex pair in an exciton-polariton condensate," *Nat. Phys.*, vol. 7, pp. 129–133, 2010.

[90] M. Wouters and V. Savona, "Stochastic classical field model for polariton condensates," *Phys. Rev. B*, vol. 79, no. 16, p. 165302, 2009.

[91] L. Ferrier, E. Wertz, R. Johne, D. D. Solnyshkov, P. Senellart, I. Sagnes, A. Lemaître, G. Malpuech, and J. Bloch, "Interactions in confined polariton condensates," *Phys. Rev. Lett.*, vol. 106, p. 126401, 2011.

[92] C. Ciuti and I. Carusotto, "Quantum fluid effects and parametric instabilities in microcavities.," *Phys. Status Solidi B*, vol. 242, pp. 2224–2245, 2005.

[93] M. H. Szymańska, F. M. Marchetti, and D. Sanvitto, "Propagating wave packets and quantized currents in coherently driven polariton superfluids," *Phys. Rev. Lett.*, vol. 105, no. 23, p. 236402, 2010.

[94] G. Christmann, G. Tosi, N. G. Berloff, P. Tsotsis, P. S. Eldridge, Z. Hatzopoulos, P. G. Savvidis, and J. J. Baumberg, "Polariton ring condensates and sunflower ripples in an expanding quantum liquid," *Phys. Rev. B*, vol. 85, p. 235303, 2012. Suppl. Information.

[95] J. Keeling, "Superfluid density of an open dissipative condensate," *Phys. Rev. Lett.*, vol. 107, p. 080402, 2011.

[96] M. Wouters and I. Carusotto, "Superfluidity and critical velocities in nonequilibrium bose-einstein condensates," *Phys. Rev. Lett.*, vol. 105, p. 020602, 2010.

[97] M. Wouters, T. C. H. Liew, and V. Savona, "Energy relaxation in one-dimensional polariton condensates," *Phys. Rev. B*, vol. 82, p. 245315, 2010.

[98] J. Allen and A. Misener, "Flow of liquid helium ii," *Nature*, vol. 141, p. 75, 1938.

[99] P. Kapitza, "Viscosity of liquid helium below the lambda-point," *Nature*, vol. 141, p. 74, 1938.

[100] S. Giorgini, L. P. Pitaevskii, and S. Stringari, "Theory of ultracold atomic fermi gases," *Rev. Mod. Phys.*, vol. 80, pp. 1215–1274, 2008.

[101] R. M. Stevenson, V. N. Astratov, M. S. Skolnick, D. M. Whittaker, M. Emam-Ismail, A. I. Tartakovskii, P. G. Savvidis, J. J. Baumberg, and J. S. Roberts, "Continuous wave observation of massive polariton redistribution by stimulated scattering in semiconductor microcavities," *Phys. Rev. Lett.*, vol. 85, pp. 3680–3683, 2000.

[102] J. J. Baumberg, P. G. Savvidis, R. M. Stevenson, A. I. Tartakovskii, M. S. Skolnick, D. M. Whittaker, and J. S. Roberts, "Parametric oscillation in a vertical microcavity: A polariton condensate or micro-optical parametric oscillation," *Phys. Rev. B*, vol. 62, pp. R16247–R16250, 2000.

[103] A. I. Tartakovskii, D. N. Krizhanovskii, D. A. Kurysh, V. D. Kulakovskii, M. S. Skolnick, and J. S. Roberts, "Polariton parametric scattering processes in semiconductor microcavities observed in continuous wave experiments," *Phys. Rev. B*, vol. 65, p. 081308, 2002.

[104] D. Sanvitto, "Controlling quantum flow," *Nature Photonics*, vol. 5, p. 638, 2011.

[105] P. G. Savvidis, J. J. Baumberg, R. M. Stevenson, M. S. Skolnick, D. M. Whittaker, and J. S. Roberts, "Angle-resonant stimulated polariton amplifier," *Phys. Rev. Lett.*, vol. 84, p. 1547, 2000.

[106] E. Kammann, H. Ohadi, M. Maragkou, A. V. Kavokin, and P. G. Lagoudakis, "Crossover from photon to exciton-polariton lasing," *New J. Phys.*, vol. 14, p. 105003, 2010.

[107] H. Franke, C. Sturm, R. Schmidt-Grund, G. Wagner, and M. Grundmann, "Ballistic propagation of exciton-polariton condensates in a ZnO-based microcavity," *New J. Phys.*, vol. 14, no. 013037, 2012.

List of Figures

Symbols and Abbreviations

$\hbar$	$h/2\pi = 1.054571 \cdot 10^{-34}$ Js $= 6.582118 \cdot 10^{-16}$ eVs
E_{g}	Band-gap energy
$E_{\mathrm{Bog}}(\mathbf{k})$	Bogoliubov dispersion
k_{B}	Boltzmann constant ($1.38062 \cdot 10^{-23}$ J/K)
BEC	Bose-Einstein condensate
L_{Cav}, L_{eff}	Cavity length, effective cavity length
CCD	Charged coupled device
μ	Chemical potential
CB,VB	Conduction band, valance band
CW	Continuous wave
g	Coupling factor
T_{TK}	Critical temperature for superfluidity (Kosterlitz, Thouless)
T_c,n_c	Critical temperature, critical density
λ_{dB}	De Broglie wavelength
γ,Γ	Decay rate
$\Delta_{\mathbf{k}}$	Detuning between cavity and exciton mode
DOE	Diffractive optical element
DBR	Distributed Bragg reflector
m^*	Effective mass of a particle in the solid state
e	Electron, unit charge ($1.602176 \cdot 10^{-19}$ C)
$D(E)$	Electronic density of states

Θ	Emission angle
E	Energy
E_b	Exciton binding energy
FWHM	Full-width half-maximum
GPE	Gross-Pitaevskii equation
ξ	Healing length
$\mathcal{C}_\mathbf{k}$,$\mathcal{X}_\mathbf{k}$	Hopfield coefficients
i/o	Input-output
I	Intensity
LDA	Local density approximation
LP, UP	Lower polariton, upper polariton
MO	Microscope objective
MBE	Molecular beam epitaxy
NMS	Normal mode splitting
NA	Numerical aperture
ODLRO	Off-diagonal long-range order
OPO	Optical parametric oscillation
f_osc	Oscillator strength
PL	Photoluminescence
P	Power
F_p	Purcell factor
Q	Quality factor
QW, QWR, QD	Quantum well, quantum wire, quantum dot
Ω_R	Rabi frequency
SLM	Spatial light modulator
c	Speed of light (299792458 m/s)
T	Temperature
t	Time
λ	Wavelength

Publications

Parts of this work are or will be published as follows:

(i) *"Higher-Order Photon Bunching in a Semiconductor Microcavity"*

M. Aßmann, **F. Veit**, M. Bayer, M. van der Poel and J. M. Hvam,

Science **325**, 297–300 (2009)

(ii) *"Ultrafast tracking of second-order photon correlations in the emission of quantum-dot microresonator lasers"*

M. Aßmann, **F. Veit**, M. Bayer, C. Gies, F. Jahnke, S. Reitzenstein, S. Höfling, L. Worschech and A. Forchel

Phys. Rev. B **81**, 165314 (2010)

(iii) *"Measuring the dynamics of second-order photon correlation functions inside a pulse with picosecond time resolution"*

M. Aßmann, **F. Veit**, J.-S. Tempel, T. Berstermann, M. van der Poel, J. M. Hvam and M. Bayer,

Opt. Express **18**, 20229–20241 (2010)

(iv) *"From polariton condensates to highly photonic quantum degenerate states of bosonic matter"*

M. Aßmann, J.-S. Tempel, **F. Veit**, M. Bayer, A. Rahimi-Iman, A. Löffler, S. Höfling, S. Reitzenstein, L. Worschech and A. Forchel

Proc. Natl. Acad. Sci. USA **108**, 1804–1809 (2011)

(v) *"Relaxation dynamics of optically imprinted polariton wires"*

F. Veit, M. Aßmann, M. Bayer, A. Löffler, S. Höfling, and A. Forchel

Proceedings of SPIE **8260**, 82600O (2012)

(vi) *"Characterization of two-threshold behavior of the emission from a GaAs microcavity"*

J.-S. Tempel, **F. Veit**, M. Aßmann, L. E. Kreilkamp, A. Rahimi-Iman, A. Löffler, S. Höfling, S. Reitzenstein, L. Worschech, A. Forchel and M. Bayer

Phys. Rev. B **85**, 075318 (2012)

(vii) *"All-optical control of quantized momenta on a polariton staircase"*

M. Aßmann, **F. Veit**, M. Bayer, A. Löffler, S. Höfling, M. Kamp and A. Forchel

Phys. Rev. B **85**, 155320 (2012)

(viii) *"Temperature dependence of pulsed polariton lasing in a GaAs microcavity"*

J.-S. Tempel, **F. Veit**, M. Aßmann, L. E. Kreilkamp, S. Höfling, M. Kamp, A. Forchel and M. Bayer

New J. Phys. **14**, 083014 (2012)

(ix) *"Spatial dynamics of stepwise homogeneously pumped polariton condensates"*

F. Veit, M. Aßmann, M. Bayer, A. Löffler, S. Höfling, M. Kamp and A. Forchel

Phys. Rev. B **86**, 195313 (2012)

(x) *"Determination of operating parameters for a GaAs-based polariton laser"*

J. Schmutzler, **F. Veit**, M. Aßmann, J.-S. Tempel, S. Höfling, M. Kamp, A. Forchel and M. Bayer

Appl. Phys. Lett. **102**, 081115 (2013)

Danksagungen

Ich möchte mich an dieser Stelle bei all denjenigen bedanken, die mich während meiner Promotionszeit unterstützt und zum Gelingen dieser Arbeit beigetragen haben. Insebesondere danke ich

- **Herrn Prof. Dr. Manfred Bayer** für die Möglichkeit der Promotion an diesem Lehrstuhl mit hervorragend ausgestatteten Laboren sowie für die wissenschaftliche Unterstüzung und Betreuung der Arbeit.
- **Dr. Marc Aßmann** für die exzellente Betreuung all die Jahre im Korrelationslabor als auch für das abschließende Korrekturlesen der Arbeit.
- **Dr. Jean-Sebastian Tempel** für die gemeinsame Zeit im Labor, die stetige Hilfe und das aufmerksame Korrekturlesen der Arbeit.
- **Dr. Jörg Debus** für die Sorgfalt beim Korrekturlesen der Arbeit und den Zuspruch in der Endphase der Promotion.
- **Lars Kreilkamp** für die gemeinsamen Mess- und Auswertungszeiten im Korrelationslabor sowie für die schöne Zeit als Tischnachbarn im Büro.
- **Johannes Schmutzler** für die gemeinsamen Messphasen im Korrelationslabor und die Stippvisite im OPO-Labor.
- **Alexander Schwan** für die gemeinsame Zeit seit Studienbeginn.
- **Michaela Wäscher, Klaus Wiegers** und **Lars Wieschollek** für all die Hilfe bei addministrativen und technischen Problemen.
- allen **E2-Mitgliedern** für die herzliche Atmosphäre am Lehrstuhl, die bereitwille Unterstützung bei Fragen sowie für die unterhaltsamen Abenden außerhalb der Labore.
- meinen Eltern **Manfred** und **Mechthild Veit** und meinem Bruder **Johannes Veit** für die nie nachlassende moralische Unterstützung in allen Lebenslagen.
- meinem Ehemann **Julian Wishahi** für den großen Rückhalt generell und die Hilfe bei Teilchenphysik-Fragen im Speziellen.